EXCITON DIFFUSION, TRANSPORT, AND LOCALIZATION IN CONJUGATED POLYMERS

A Dissertation
Submitted to the Graduate Faculty
of the
North Dakota State University
of Agricultural and Applied Science

By

Josiah August Bjorgaard

In Partial Fulfillment
for the Degree of
DOCTOR OF PHILOSOPHY

Major Department:
Chemistry and Biochemistry

October 2013

Fargo, North Dakota

North Dakota State University
Graduate School

Title

Exciton Diffusion, Transport and Localization in Conjugated Polymers

By

Josiah August Bjorgaard

The Supervisory Committee certifies that this ***disquisition*** complies with North Dakota State University's regulations and meets the accepted standards for the degree of

DOCTOR OF PHILOSOPHY

SUPERVISORY COMMITTEE:

Prof. Dr. M. Erkan Köse
Chair

Dr. Seth C. Rasmussen

Dr. Svetlana V. Kilina

Dr. Alexander J. Wagner

Approved:

11/13/2013
Date

Dr. Gregory R. Cook
Department Chair

ABSTRACT

Conjugated polymers are wide bandgap semiconductors which have a series of conjugated π-orbitals that extend along the polymer 'backbone'. The π-orbital conjugation can be disrupted by twisting of the polymer, affecting their optical properties. These materials are very useful for devices, where they are frequently found in semicrystalline thin films. In thin films, Frenkel excitons diffuse on a nanometer scale. However, measurement of the diffusion length of excitons in conjugated polymer films is currently very difficult. Disordered packing and twisting of polymers plays a significant role, but has not been examined in detail. This dissertation presents methods of measuring exciton diffusion length in polymer films and nanoparticles and explains the effect of nuclear disorder on the optical spectra and exciton diffusion in semicrystalline polymer films.

ACKNOWLEDGEMENTS

Thanks to my committee members, listed above, for their mentorship and continued support in this scientific pursuit. Special thanks to my family for their love and support in helping me obtain my goals and in general. Additional thanks to other graduate students and post-doctoral researchers who have helped me along the way; specifically Dr. Zhenghuan Lin, Dr. Kirill Velizhanin, Dr. Ayse Gul Yavuz, Akila Iyer, Baris Yilmaz, Cole Larsen and Trent Anderson.

TABLE OF CONTENTS

LIST OF TABLES

.

LIST OF FIGURES

LIST OF ABBREVIATIONS

LED ..... light emitting diode

PV ..... photovoltaic

P3HT ..... poly(3-hexylthiophene)

MEH-PPV ..... poly[2-methoxy-5-(2-ethylhexyloxy)-1,4-phenylenevinylene]

BHSC ..... bulk heterojunction solar cell

NP ..... nanoparticle

PCBM ..... phenyl-C_{61}-butyric acid methyl ester

MO ..... molecular orbital

HOMO ..... highest occupied molecular orbital

LUMO ..... lowest unoccupied molecular orbital

DFT ..... density functional theory

TD-DFT ..... dime-dependent density functional theory

HF ..... Hartree-Fock

TD-HF ..... time dependent Hartree Fock

LCF ..... long range corrected functional

PL ..... photoluminescence

HOPG ..... highly ordered pyrolytic graphite

DCB ..... ortho-dichlorobenzene

UV-Vis ..... ultraviolet-visible

FRET ..... forster resonant energy transfer

THF ..... tetrahydrofuran

AFM ..... atomic force microscopy

SV ..... Stern-Volmer

DOF..... degree of freedom

PES..... potential energy surface

P3MT ..... poly(3-methylthiophene)

O3MT..... oligo(3-methylthiophene)

T3MT ..... tetra(3-methylthiophene)

PES..... potential energy surface

PCM ..... polarizable continuum model

NTO ..... natural transition orbital

FWHM ..... full width at half maximum

INTRODUCTION AND BASIC CONCEPTS

Excited States in Twisted Polymer Chains and Condensed Phase Morphologies

Introduction

The most common conjugated polymers are wide bandgap semiconductors which exhibit a strong exciton binding energy. These qualities arise because of a system of conjugated π orbitals along the polymer backbone. They can be tailored in an organic chemistry lab to produce optically tuned materials.[1] In the past several decades, conjugated polymers have been used in optoelectronic applications due to their ability to form highly efficient light emitting diodes (LEDs) and photovoltaics (PVs) from flexible thin films.[2–5]

An early account which is commonly misinterpreted as a discovery of conjugated polymers involves an observation of changing color in aniline upon oxidation. Although there is clearly a change in the absorbance wavelength, this was not recognized as polymerization at the time.[6] Today, this observation suggests the possible synthesis of polyaniline. Before the discovery of conductivity in anthracene in the early 20th century, however, such applications were not likely to have been realized.[7] More recently, the Nobel Prize was awarded to A. J. Heeger, H. Shirakawa, and A. MacDiarmid for the discovery of conductivity in doped polyacetylene.[8,9] During this time, conjugated polymers have become a popular field with a strong research basis and many applications.

Conjugated polymers are now available commercially and have been well studied. Some notable examples of these polymers, shown in Fig. 1.1, include polyacetylene, poly(3-hexylthiophene) (P3HT), and poly[2-methoxy-5-(2-ethylhexyloxy)-1,4-phenylenevinylene] (MEH-PPV). P3HT has found wide application in organic PVs and is the main focus of this dissertation. Despite the history and current widespread use of conjugated polymers, some

aspects of their optical properties are not well understood. To understand the current state of the art, it is necessary to first give a general description of their photoexcitation.

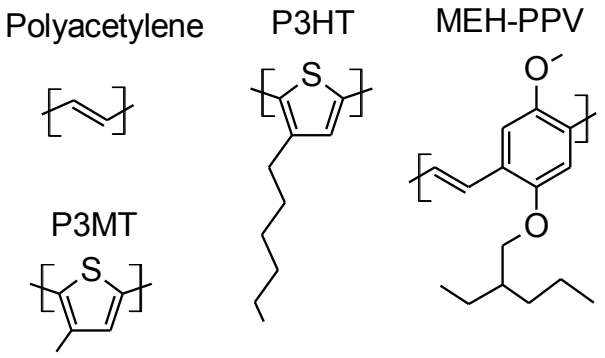

Figure 1.1. Chemical structures of some representative conjugated polymers.

It was observed early on that the optical properties of conjugated polymers converged upon lengthening of the polymer chain.[10] This result was taken to be a result of localization of the excited state along a polymer backbone (Fig. 1.2). Indeed, as the length of a conjugated chain is extended, a lowering of the excitation energy evolves according to a well-defined trend.[11,12] This relationship between oligomer length and optoelectronic properties has been investigated experimentally[13–15] and extrapolated to predict polymer properties.[12,16,17]

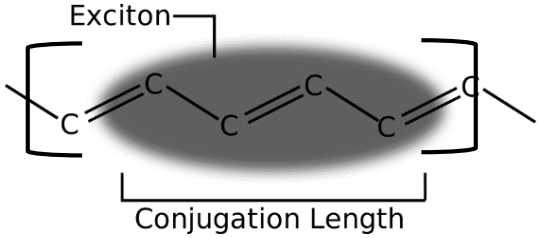

Figure 1.2. Cartoon of an exciton in polyacetylene showing the size of the exciton as the conjugation length.

This phenomena is frequently attributed to quantum confinement effects, i.e. the elementary particle in a box quantum mechanics problem, where the conjugated backbone is analogous to a box with boundary conditions given by the oligomer size. But the problem is more complex, since disorder in the geometry of the polymer backbone can occur. The extent of

localization can be dominated by this disorder when the length of a conjugated chain reaches some limit where the 'boundary condition' is essentially infinite.

One origin of localization is the twist angles of conjugated polymer chains.[18] The twist angle is a torsion between repeat units (Fig .1.3). It is known in other conjugated molecules for its intense effect on optical properties.[19] For P3HT and other polythiophenes, the twist angle of 2,2'-bithiophene has been used as a model compound to examine the potential of the twist angle.[20] The reason that the twist angle effects optical properties can be illustrated by a picture of reduced orbital overlap upon twisting of the backbone (Fig 1.3, left). Several studies have attempted to use computational methods to explore localization effects caused by the twist angle by introducing a single torsion in a polymer chain, but not seen the expected localization effets of the twist angle.[21,22] On the contrary, computational studies using numerous torsional defects produced by, i.e. molecular dynamics, has resulted in a picture of separate light absorbing subunits along a disordered polymer backbone.[23–25] However, localization due to twist angle disorder has not been studied using computational methods which accurately reproduce the absorption spectrum of polythiophenes and consequently, the extent of localization may be incorrectly predicted. This task is successfully performed in chapter 3 of this dissertation.

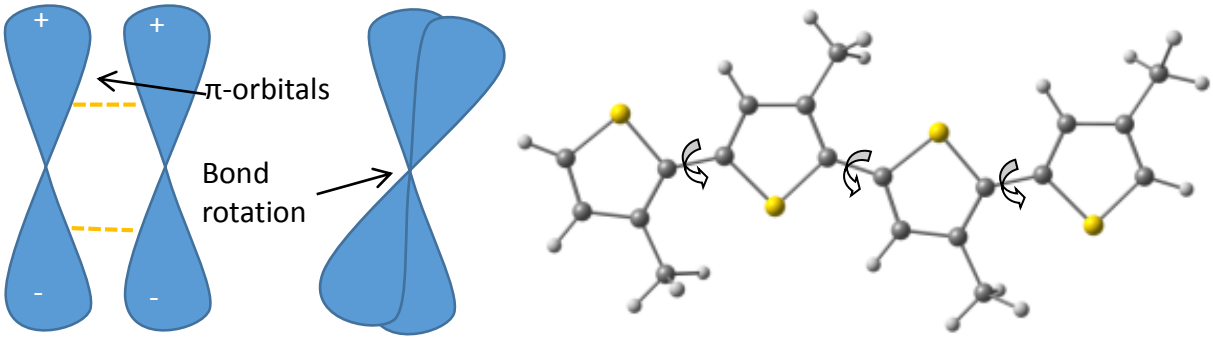

Figure 1.3. (Left) Cartoon of π-bonding and the resulting reduction in π overlap due to twisting of π-bonds. (Right) Twist angles in tetra(3-methylthiophene). Rotation about the twist angles can occur continuously around the full rotation of the bonds between 3-methylthiophene polymer building blocks. This rotation is torsion around the bond connecting 3-methylthiophene units.

The utility of twist angles has recently been recognized in conjugated polymers,[26,27]. Polymer structures have been engineered which can use intramolecular interactions to stabilize conformations that present appealing delocalization, band-gap, and transport properties for solar cell applications.[28] The use of attractive interactions which cause specific conformations to become the most probable has been termed "conformational locking".[26,29] This illustrates an example of how chemical structure can affect the emergent properties of conjugated polymers in the condensed phase.[3,30–32] Induced backbone planarity from "conformational locking" improves properties such as charge mobility,[33,34] exciton diffusion length,[35] localization and bandgap.[36] Details of some of these effects (localization, bandgap, and exciton diffusion length) in P3HT are given later in this dissertation.

Important processes in conjugated polymers can be described in the same way for a variety of different materials.[32] This makes computational prediction of, e.g., exciton diffusion length or charge mobility possible and allows information that is gathered from simulations on model systems to be applicable across the range of conjugated molecules. Experimental advances, such as single molecule spectroscopy and ultrafast techniques have allowed direct observation of the excited states in conjugated polymer chains and their ability to traverse length scales on the order of nanometers.[37,38] These techniques have further shown rapid molecular reorganization on the time scale of the optical lifetimes and coherent, wavelike exciton transport in controlled situations.[39,40] Still, diffusive exciton transport is most frequently encountered in conjugated polymer applications.[41–44]

The diffusion length of excitons (L_D) is given by

$$L_D = \sqrt{2d\tau D} \qquad \text{(Eq. 1.1)}$$

where d is the dimensionality of diffusion, τ is the natural lifetime of the excitons, and D is the diffusion coefficient of the excitons. Controlling L_D could allow for tuning of condensed phase morphologies for specific applications. In LEDs, decreasing the L_D can lead to increased device efficiency by reducing loss pathways that occur when excitons combine.[30,45] In bulk-heterojunction solar cells (BHSCs), described later in this chapter, increasing L_D can increase device efficiency by increasing the possibility that an exciton reaches a domain boundary where charge separation (exciton splitting) can occur.[46–49]

These examples of device optimization require measurement of L_D in thin films. Most measuring techniques require varying film thickness on substrates which quench local excitons. A number of variations upon this method are available in the literature. Another morphology which has found some recent application is conjugated polymer nanoparticles (NPs). For NPs of conjugated polymers, described later in this chapter, there was previously no L_D measurement technique available. A novel method for measuring L_D in NPs is presented in chapter 2. This technique is applied to the amorphous polymer MEH-PPV, but some conjugated polymers, e.g. P3HT, are semicrystalline.

In semicrystalline polymers, it is difficult to perform an absolute measurement of L_D for a given material. L_D depends on intermolecular interactions which can vary greatly depending on processing conditions.[50] Further, since polymer crystallites may have an anistropic diffusion coefficient, L_D depends on semicrystalline morphologies.[35,51] This is shown to vary with film thickness for P3HT in chapter 2. Recently, a method has been proposed by Lunt et al. which measures L_D without changing film thickness, but this does not consider the orientation or shape of crystallites, i.e. it assumes homogeneous diffusion.[35] Unfortunately, in the previous two decades, numerous studies which presume that excitons diffuse homogenously in semicrystalline

polymers, e.g. P3HT, can be found.[35,43,48,52,53] This is incorrect, since the microscopic interactions governing transport rates are anisotropic (shown in chapter 4). To investigate diffusive exciton transport in P3HT requires a microscopic description of transport in the polymer morphology.

The macroscale description of exciton diffusion used for measurements in chapter 2 does not provide specific information about the microscopic properties that govern exciton transport. To do so, current methods are built upon in chapter 4 to simulate semicrystalline morphologies. These methods originate from charge transport simulations performed for disordered molecular materials using Monte-Carlo methods in the mid 20th century.[54] In fact, an early mention of exciton diffusion simulation in molecular materials is a work by Bässler from 1984.[55] There, kinetic equations are used to simulate transport on an energetically disordered lattice with a residence-time algorithm. Recently, studies have used a multiscale method to simulate exciton diffusion by taking input for rate equations from atomistic simulation of electronic structure.[41,56,57] As a result, more accurate rates of energy transfer can be employed, giving more accurate and material specific diffusion coefficients. However, these methods consider the material morphologies to be homogeneous, whereas semicrystalline conjugated polymer films are heterogeneous, demonstrating both ordered and disordered domains. This problem is addressed in chapter 4, where rate equations are formed based on atomistic simulations of ordered and disordered oligomer dimers and a kinetic Monte-Carlo simulation is performed in a semicrystalline morphology.

Condensed Phase Morphologies

Several morphologies of condensed phase polymers are examined or discussed in this dissertation. These include thin films, nanoparticles and bulk-heterojunctions. In any of these

morphologies, a conjugated polymer can be semicrystalline. Since this dissertation focuses on P3HT as a model compound, the structure of P3HT crystallites is described. The morphology of a single polymer chain may be different in each of these structures and may affect localization and transport properties.

Spincast Thin Films. Thin films of conjugated polymers can be cast in a thin film by spincoating of a solution onto a substrate. In general, this process is performed by placing a small amount (< 1mL) of polymer solutions ranging from 0.001 mg/mL to 20 mg/mL on a substrate which is fixed to a rotor by vacuum. Commonly, the substrate is glass or quartz. The spincoating process is commonly used to prepare BHSCs as described below. The spin coater rotates at high speed (500-1500 rpm) while the solvent evaporates, leaving a thin layer of polymer film on the substrate (5 nm - 10μm). This process is depicted in Fig. 1.4. Thin films are the most commonly employed condensed phase morphology in device applications, where the film may be a mixture of two phase separated components, as in BHSCs described below. However, conjugated polymers can also be prepared as NPs.

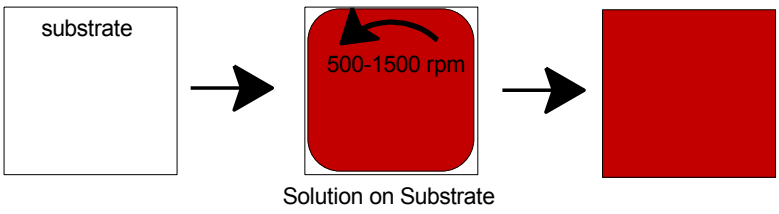

Figure 1.4. Depiction of the spincasting process. Solution is placed on substrate and rotated at high speed while a thin layer of solution evaporates, depositing a thin film on the substrate. To spincast films of varying thickness (5nm-10μm), solution concentration is varied from 0.001 mg/mL to 20 mg/mL

Conjugated Polymer Nanoparticles. Conjugated polymer NPs have recent applications ranging from chemical sensing[58,59] to PVs.[47,60] Various methods allow simple preparation of NP solutions with diameters ranging from several nanometers to hundreds of nanometers in neat

solvents or with the aid of dispersants.[61,62] Generally, a dilute solution of well solvated polymer is injected into a 'bad' solvent during sonication with or without dispersants included in the 'bad' solvent. The 'good' solvent is removed by vacuum. The result is nearly spherical aggregates of conjugated polymers in solutions. These nanoparticles are retained as a dispersion. The optical spectra of these NPs are usually very similar to their counterpart neat thin film spectra, while some variation has been seen in P3HT nanoparticles, where the semicrystalline morphology depends on processing conditions.[47,60,63]

Bulk-Heterojunction Solar Cells. P3HT is frequently used in BHSCs when combined with a fullerene derivative, phenyl-C_{61}-butyric acid methyl ester (PCBM).[16,64,65] A mixture of the polymer and PCBM is spincoated onto a substrate. Phase separation occurs, where polymer and PCBM partially crystallize between mixed domains.[16,64] As a solar cell, the conjugated polymer acts as the light absorbing material while PCBM acts as an electron acceptor, causing separation of excitons into mobile charge carriers to generate current.[65] The highest efficiency P3HT/PCBM BHSCs have polymer domain size close to L_D.[66]

Structure of P3HT Aggregates. Two types of P3HT crystallites have been observed in thin films. Type 1 is frequently encountered in applications, where alkyl sidechains are interdigitated and the P3HT forms a three dimensional crystal structure with stacked lammelae. Type 2 is a 2 dimensional crystal structure involving dispersed crystalline lammelae.[67–69] Crystals of type 1 can extend in either the interdigitated or π stacking direction (Fig. 1.5).[67,70,71] Crystallite structures may be thought of as polymers folded into lammelae of interdigitated segments (Fig. 1.5, right) which are then stacked together to form π-stacks. Alternatively, elongated interdigitated lammelae with only a few π-stacks can be formed.[70] That is, crystallites can be categorized as having many more unit cells in either the $\vec{a}$ or $\vec{b}$ directions.

Generally, spincast films of P3HT contain the π-stacked type 1 crystallites.[71] The induced planarity and aggregation effects in crystallites affect the photophysical properties of this material. These effects are discussed throughout this dissertation. Background information on these properties and methods used to analyze them are described in the following sections of this chapter. Wherever the unit cell parameters are required (e.g. crystalline morphologies), those given in Fig. 1.5 ($\vec{a}$ and $\vec{b}$ from Ref. 72, $\vec{c}$ from simulations in chapter 3) have been used.

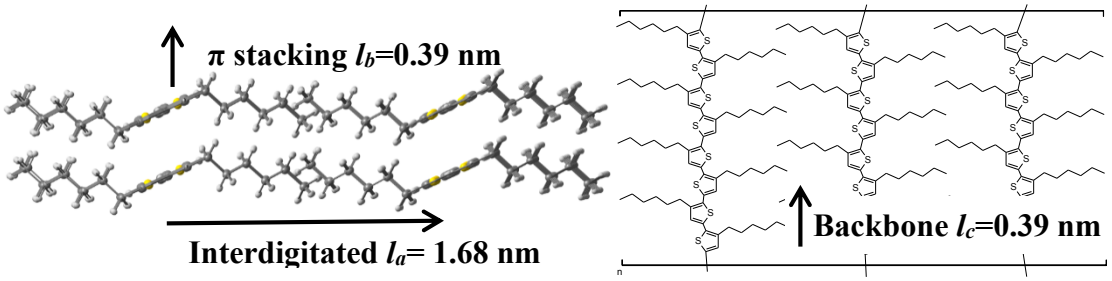

Figure 1.5. (Left) Proposed P3HT crystal structure for type 1 crystallites showing interdigitated ($\vec{a}$) and π-stacking ($\vec{b}$) directions. (Right) Depiction of P3HT crystalline lammelae in $\vec{a}$ and backbone ($\vec{c}$) direction.

Optical Processes in Conjugated Materials

Optical Excitation. Absorption and emission of photons are one of the fundamental processes which give conjugated molecules their useful properties. This process is excitation. In zeroth order approximation, i.e. neglecting electron correlation, photon absorption excites an electron from an occupied molecular orbital (MO) to an unoccupied MO. In most molecules, the lowest energy excitation occurs when an electron in the highest occupied molecular orbital (HOMO) is transferred to the lowest unoccupied molecular orbital (LUMO). In P3HT, this transition occurs from the ground (singlet) electronic state (S_0) to excited (singlet) state n (S_n).[10] The photon energy is commonly denoted by $h\upsilon$, where h is Planck's constant and υ is the photon frequency. For a transition from S_0 to S_n, the photon must have the correct energy, i.e. $h\upsilon_{0\rightarrow n} = E_0 - E_n$ where E_n is the energy of state n from the time independent Schrodinger equation for state n,

$$H\Psi_n = E_n\Psi_n \quad \text{(Eq. 1.2)}$$

This does not describe the interaction with light, but only the allowed electronic state energies between which transitions can occur due to photon absorption. The probability of absorption of an impinging photon is given by the absorption coefficient. This quantity is the fraction of impinging photons of a specific energy which are absorbed.[73]

Franck-Condon Transitions. Within each state, a manifold of vibrational levels exist (Fig. 1.6) which create a vibronic structure in the absorption and emission spectra. For large conjugated molecules this is best observed at cryogenic temperatures due to broadening of the individual vibronic transitions by inhomogeneous broadening. Inhomogeneous broadening is due to static factors such as molecular conformation and intermolecular dipole-dipole interactions.[73] In conjugated polymers, the vibronic transitions are frequently observed in the both absorbtion and emission spectra despite significant inhomogeneous broadening. The probability of a vibronic transition is related to the overlap of vibrational wavefunctions in two vibronic states and varies between materials.

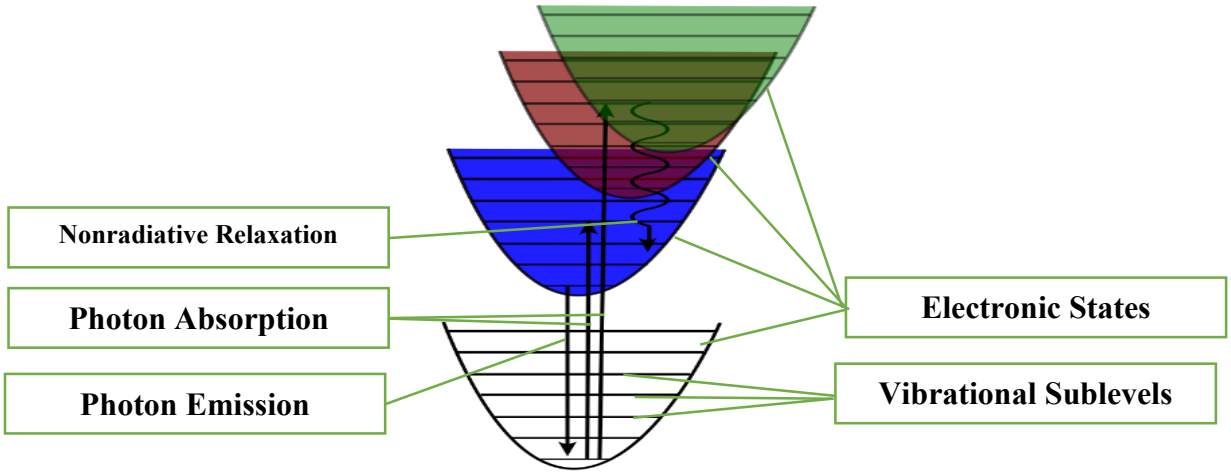

Figure 1.6. Schematic illustrating 4 adiabatic electronic states with vibrational sublevels and possible transitions between vibronic states. Franck-Condon emission according to Kasha's rule is demonstrated using arrows to represent excitation and emission.

Quantum Yield. The emission efficiency, or quantum yield of emission, is the ratio of absorbed to emitted photons. Competing processes cause the absorbed photon to be consumed nonradiatively. The quantum yield of emission Φ_{em} is related to the rate of photon emission (k_{em}) and other excited state quenching processes (k_i).[73] For example, nonradiative relaxation from excited states to ground state, energy transfer to another molecule, or charge transfer can occur and prevent photon emission from occurring.

$$\Phi_{em} = \frac{k_{em}}{\sum_i k_i} \quad \text{(Eq. 1.3)}$$

Kasha's Rule. According to Kasha's rule, excitation and emission occur only *from* the lowest vibrational state of the ground and excited state, respectively. An analogue to this rule states that emission occurs only from the lowest electronic excited state. This rule assumes that nonradiative relaxation, the process by which excess vibrational energy is dissipated to the environment, is much faster than the emission timescale. Excitation to states higher than the first vibronic state results in rapid nonradiative relaxation, so that emission occurs only from the first excited vibronic state.[19]

Frenkel Excitons. Upon photoexcitation, a positively charged hole interacts coulombically with the excited electron. The strength of this interaction, called the exciton binding energy, is substantial in many conjugated materials. The bound electron and hole can collectively be described as a quasiparticle, termed an exciton.[74]

Two limiting cases of excitons exist, the Wannier-Mott and Frenkel exciton.[75] In the latter case, the exciton binding energy is large enough to cause localization of the exciton to a single molecule. In the former case, lower exciton binding energy leads to a delocalized exciton over many molecules or unit cells in the case of periodic systems.[74] The strength of exciton binding energy in conjugated molecules is an important consideration when simulating

photophysical processes. The Frenkel-type excitons can be approximated as single molecule excited states.

Optical Spectra of Aggregates. The optical effects of molecular aggregation can be of the H- or J-type.[76,77] These correspond to limiting cases of the relative orientation of transition dipole moments (Fig. 1.7). For polymers with transition dipole moment parallel with the polymer backbone, a phenomena similar to J-type aggregation occurs between repeat units. Although true J-type aggregation would require that the constituents were not chemically bonded, an analogous effect occurs due to coupling of transition dipole moments between chemically bonded subunits. In aggregated chains, H-type aggregation is generally seen upon π-stacking.[78]

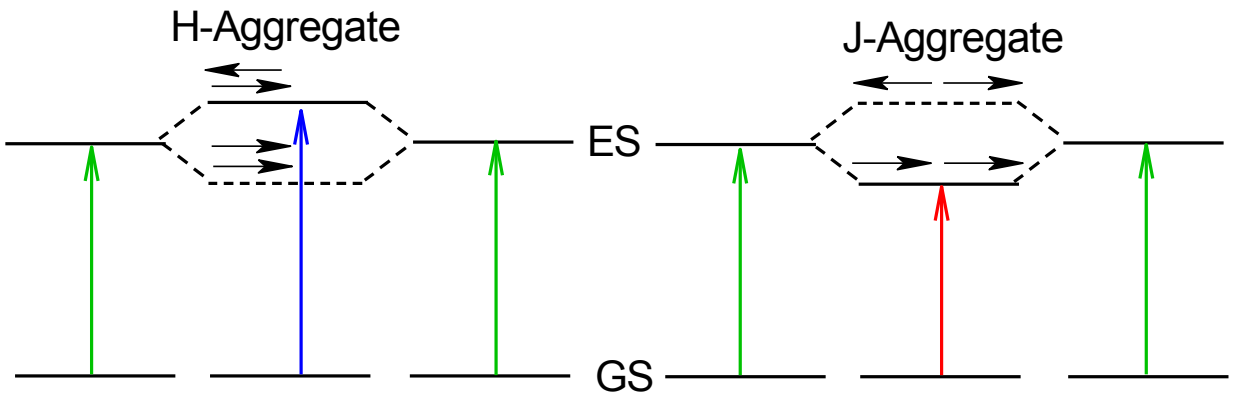

Figure 1.7. Schematic of the effects of H- and J-type aggregation on the excitation energy of a two level chromophore. Transition dipoles are given by black arrows, while red, and blue arrows describe bright excitations which are red or blue shifted from the excitation energy of non-aggregated chromophores (green). Dark transitions may also occur to the levels without illustrated transitions.

In an isolated chain, intramolecular disorder changes J-type aggregation strength between repeat units, while intermolecular coupling changes H-type aggregation strength.[79] Aggregation may occur in solution, thus becoming stronger for higher molecular weight polymers under certain conditions (e.g. 'bad' solvent).[50,80] In neat films, polymers are certainly aggregated. In this case, the optical spectra are strongly affected by the *type* of aggregation which is in turn

affected by the intermolecular ordering.[81,82] The type of aggregation not only affects the excited state energy, but also the 'allowedness' of vibronic transitions in P3HT aggregates.

A comprehensive treatment of these effects has been given by Spano et al. over the course of many publications.[78,82–85] For interpreting the optical spectra here, it is sufficient to summarize these works in two simple statements. Isolated P3HT in an amorphous polymer matrix exhibits a unity ratio of the intensity of 0-0 ($I_{0\text{-}0}$) to 0-1 ($I_{0\text{-}1}$) vibronic peaks, i.e. $\eta_C = \frac{I_{0-0}}{I_{0-1}}$. Increasing the strength of H-aggregate intermolecular coupling increases η_c in the absorption spectrum and decreases η_c in the emission spectrum. Of course, the coupling strength of H-aggregation should change very little in the same crystal structure. Since film crystallinity is directly related to the ratio of H-aggregates to amorphous type aggregates, the ratio of vibronic peaks changes and one can predict variation in the film crystallinity from this readily observed metric.

Simulation Methods and Theoretical Background

Fermi's Golden Rule. Fermi's golden rule gives the rate of transition from an initial state, *m*, to a final state, *n*, given a Hamiltonian, *H*. The transition rate is

$$k_{mn} = \frac{2\pi}{\hbar} |J_{mn}|^2 D_{mn} \qquad \text{(Eq. 1.4)}$$

where J_{mn} is the coupling between states *m* and *n* and D_{mn} is the joint density of states of *m* and *n*.[86] This transition rate is applicable to thermalized transport. That is, when the current state reaches equilibrium on a much faster timescale then the transition rate. In conjugated polymers, this can be applied to intra- and inter- chain exciton transport when the sites are rapidly thermalized chromophores. Fermi's golden rule is applied to various systems like electron or exciton transfer through explicit representations of $|J_{mn}|$ and D_{mn}. One example is the Marcus theory of electron transfer.

Marcus Theory of Electron Transfer. The basic equation of Marcus Theory is

$$k_{et} = \frac{2\pi}{\hbar}|J_{mn}|^2(4\pi\lambda k_b T)^{-\frac{1}{2}} \exp(-\frac{(\lambda+\Delta G^o)^2}{4\lambda k_b T}) \quad \text{(Eq. 1.5)}$$

where λ is the reorganization energy of the transition, T is temperature and ΔG^o is the Gibb's free energy change for the electron transfer reaction. ΔG^o can be determined from the difference in oxidation or reduction potential of donor and acceptor for hole or electron transfer, respectively.[87,88] Later in this dissertation, a similar equation is used to describe exciton transfer where the rate is calculated using output from density functional theory (DFT) calculations.

Density Functional Theory. Throughout this dissertation, DFT has been used to predict the properties of conjugated polymers. Many variations have been developed, i.e. various exchange-correlation potentials.[89] The accuracy and scale of computations allow one to examine large conjugated organic molecules such as conjugated polymers.[89] To introduce DFT, we first define the particle density, $\rho(r)$, of a wavefunction is given by

$$\rho(r) = N\int d^3r_2 \int d^3r_3 \ldots \int d^3r_N \Psi^*(r, r_2, r_3, \ldots, r_N)\Psi(r, r_2, r_3, \ldots, r_N) \quad \text{(Eq. 1.6)}$$

DFT is based on the statement that the ground state wavefunction Ψ_0 is a unique functional of the density, i.e.,

$$\Psi_0 = \Psi(\rho_0) \quad \text{(Eq. 1.7)}$$

In particular, this leads to a self consistent expression when the molecular wavefunction is expanded in the basis of single-particle MOs (ϕ_n),

$$\Psi_0 = \sum_n c_n \phi_n \quad \text{(Eq. 1.8)}$$

The orbitals which reproduce the density are then given by

$$\left[-\frac{\hbar^2}{2m}\nabla^2 + V_s(r)\right]\phi_i(r) = \epsilon_i\phi_i(r) \quad \text{(Eq. 1.9)}$$

where V_s is defined by

$$V_S = -\sum_\alpha \frac{Z_\alpha}{r_{1\alpha}} + \int \frac{\rho_s(r')}{|r-r'|} d^3r' + V_{XC} \quad \text{(Eq. 1.10)}$$

under the constraint $\rho_s(r') = \sum_i^N |\phi_i(r)|^2$. The exact form of the exchange-correlation potential, V_{XC}, is unknown and various strategies for determining appropriate expressions have been formulated and tested against experimental data. To yield the MOs which reproduce the single particle density, Eq. 1.9 is solved iteratively using an appropriate exchange-correlation potential, e.g. one which produces accurate predictions of experimental values.[89] Further discussion of DFT follows descriptions of various DFT based methods used in this dissertation.

Time-dependent DFT. The time dependent formulation of DFT (TD-DFT), where the single particle density is subject to an external oscillatory perturbation, results in the following eigenvalue equation in the basis of position (X+Y) and momentum (X-Y) coordinates.

$$\left[\begin{pmatrix} A & B \\ -B & -A \end{pmatrix} - \Omega \right] |X,Y>= 0 \quad \text{(Eq. 1.11)}$$

Where Ω is the transition energy, |X,Y> is a vector of excitation (X) and de-excitation (Y) coefficients describing the transitions between (Kohn-Sham) MOs. A and B are defined by

$$(A+B)_{nmjk} = (\epsilon_a - \epsilon_i)\delta_{ij}\delta_{ab} + 2(nm|jk) + 2f^{xc}_{iajb} - c_x(mj|nk) \quad \text{(Eq. 1.12)}$$

$$(A-B)_{nmjk} = (\epsilon_a - \epsilon_i)\delta_{ij}\delta_{ab} + c_x(mj|nk) \quad \text{(Eq. 1.13)}$$

where the exchange-correlation kernel in the adiabatic approximation is given by

$$f^{xc}(r,r') = \frac{\delta^2 V_{xc}}{\delta \rho_s(r)^2} \quad \text{(Eq. 1.14)}$$

and the coulomb type integral notation is used. The coefficient c_x allows inclusion of 'exact' exchange, i.e. the exchange of Hartree-Fock (HF) theory. Time-dependent HF theory (TD-HF) is incorporated in this formalism by setting c_x=1 and f^{xc}=0.[90,91]

TD-DFT exchange-correlation potentials have been developed which reproduce optical spectra of organic molecules with high precision and have been used not only to determine the

energy of transitions, but also determine the oscillator strength and localization of the electronic transitions.[92] Many density functional methods involve incorporating a portion of exact exchange in the exchange-correlation functional (where the term involving c_x is incorporated into f^{xc}). For example, the B3LYP functional incorporates 30% exact exchange for empirical reasons.[93–98]

Table 1.1. Parameters for specific long range corrected functionals from Eq. 3.1 describing the distance at which HF exchange becomes prevalent (c), the contribution of HF exchange at short distance (a_{short}) and at long distance (a_{long}).

	B3LYP	CAM-B3LYP	ωB97XD	LC- ωPBE
c	0	0.33	0.2	0.4
a_{short}	0.19	0.19	0.22	0.25
a_{long}	0.19	0.65	1	1

Long Range Corrected Exchange-Correlation Functionals. Excellent agreement for optical excitations can be found for long-range corrected functionals (LCFs) in TD-DFT calculations.[92,99–102] Some LCFs, e.g. CAM-B3LYP, predict excitation energies and oscillator strengths of organic compounds with high accuracy.[100–102,102,103] All LCFs include asymptotically increasing HF exchange at increased electron-electron separation by partitioning of the two electron operator in Eq. 1.12 and 1.13 according to the following scheme,

$$\frac{1}{r} = \frac{1-\mathrm{erf}(cr)}{r} + \frac{\mathrm{erf}(cr)}{r}. \qquad \text{(Eq. 1.15)}$$

where c is a parameter and r is the electron-electron distance. The contribution from HF exchange can then be varied between long and short range. The coefficient c_x of Eq. 1.12 and 1.13 becomes a_{short} and a_{long} (the contribution from exact exchange at short and long distance given by the coefficient c) with the corresponding distance partitioning scheme of the two-electron operator. Some parameters for various LCFs are given in Table 1.1. Notable examples of these functionals include CAM-B3LYP,[92] LC-ωPBE,[102,103] and ωB97X-D.[100]

Subsystem Density Functional Theory. Subsystem TD-DFT provides a means of calculating the strength of weak couplings between electronic transitions at moderate computational cost.[104,105] The couplings between transitions are directly related to the coupled response of single subsystem transitions. The subsystem might be defined as a single polymer chain in a dimer of two 'intertwined' polymers as performed in chapter 4. It is most instructive to present the two subsystem working equation for subsystem TD-DFT in the Tamm-Dancoff approximation (Y=0 in Eq. 1.11).

$$\begin{bmatrix} \tilde{A}^{I} & \tilde{C}^{I/II} \\ \tilde{C}^{II/I} & \tilde{A}^{II} \end{bmatrix} \begin{bmatrix} \tilde{x}^{I} \\ \tilde{x}^{II} \end{bmatrix} = \omega \begin{bmatrix} \tilde{x}^{I} \\ \tilde{x}^{II} \end{bmatrix}. \qquad \text{(Eq. 1.16)}$$

where $\tilde{A}$ is a diagonal bock containing the excitation energies of isolated subsystems *I* or *II*, the blocks $\tilde{C}$ contain transition densities of subsystems *I* and *II* interacting through a coupling kernel, and $\tilde{x}$ are solution vectors.[106]

Subsystem-DFT is not an exact method and is correct only in the limit of vanishing couplings.[107] However, accurate prediction of measured excitonic couplings in photosynthetic complexes is evidence of its phenomenological accuracy in similar systems. These calculations have comparable value to those found experimentally.[108]

Discussion of DFT Methods for Conjugated Polymers. The widespread use of DFT for the ground and excited state properties of organic molecules has been made possible by a wide range of exchange-correlation functionals which then allow reproduction of the experimental properties. The major strength of DFT in this respect is an ability to produce accurate results in large systems. It is routine to simulate systems of greater than 100 atoms.[109]

For conjugated polymers, the validation of DFT and TD-DFT methods has relied upon extrapolation procedures. For these procedures, either polymer or extrapolation of an oligomer series (which increases in length) are compared with simulations of an oligomer series oligomers

of increasing length.[110–112] Good agreement for predictions of oxidation/ionization potential[110,112] and bandgap[110–112] have been found for a wide variety of polymers. Similarly, for potential energy calculations, e.g. of twist angle potentials, DFT calculations have been determined to give closely matching results to high accuracy wave function based methods using functionals such as B3LYP.[113] Indeed the parameterization of a molecular dynamics force field for oligothiophenes with B3LYP based calculations gives accurate crystallization enthalpies.[114]

The localization of excited states is of importance for later discussions. Transition densities in TD-DFT (introduced in chapter 3) also give qualitatively accurate results for exciton sizes in conjugated polymers. LCFs have been used to predict exciton sizes for planar MEH-PPV polymers The effect of the amount of exact HF exchange incorporated in LCFs affects localization, predicting decreasing exciton size with increasing long-range HF contribution.[25,115] The selection of LCF functional for this purpose is further discussed in chapter 3.

It is still not feasible to determine the dynamics of systems of this scale using ab initio methods.[40,116] This prevents the calculation of, e.g., ensemble averages or relatively long time scale transport properties. To do so, DFT simulations must be coupled to other methods. This is done in chapters 3 and 4, where DFT simulations are used to parameterize the construction of disordered chains by a Monte-Carlo method and determine the strength of couplings between single chain excitons in dimers to simulate exciton diffusion.

Multiscale Model for Exciton Diffusion. A general description of the multiscale method used in chapter 4 to simulate exciton diffusion in semicrystalline morphologies is described here, with more detail given in the respective section. In general, input parameters for a rate equation are taken from DFT calculations and experimental optical spectra. This rate equation is used to perform a kinetic Monte-Carlo simulation of exciton hopping. The nuclear geometry of polymer

chains for DFT calculations of the electronic structure of dimers is taken from molecular dynamics calculations (in molecular dynamics simulations, the forces of a molecule are simulated using Newton's equation of motion). Initial polymer chain geometries are chosen through Monte-Carlo selection of initial conformations. Essentially, this is a sequential multiscale method, with output from one method becoming input for another without instantaneous feedback.

There are three temporal and spatial scales described in this specific multiscale simulation. First, the nuclear geometry is simulated at the longest time scale, where molecular conformation can be acquired during the process of preparing a condensed phase morphology, as described above. Second, kinetic Monte-Carlo simulations occur during the lifetime of an exciton and span the exciton diffusion length. Third, electronic structure calculations give an instantaneous snapshot of the electronic structure of the molecule or molecular dimer in the selected geometry of each exciton hopping site. This general description of simulating L_D will be explained in detail in chapter 4. First, methods of measuring L_D are discussed in chapter 2.

OPTICAL SPECTRA OF P3HT THIN FILMS AND EXCITON DIFFUSION LENGTH MEASUREMENTS

Exciton diffusion length measurements have been performed by analyzing the optical spectra or lifetime of a material with and without an optical quencher.[51,52,117] Here, the quenching of photoluminescence (PL) of P3HT thin films on highly ordered pyrolitic graphite (HOPG) are examined. The optical spectra of P3HT has resolved vibronic peaks and lineshape changes upon changing film thickness. The change in line shape is also discussed in this section. From the intensity of these optical spectra, L_D can be inferred. This measurement technique is explored in detail in this chapter. The change in lineshape of P3HT optical spectra is characteristic of varying crystallinity, which is shown in chapter 4 to have a significant effect on L_D. Films are not the only important aggregate structure for conjugated polymers. Exciton diffusion also occurs in NPs.

There was no available method for measuring L_D in NPs comprised of only conjugated polymers until publication of the method described here.[42] This method uses changes in the NP emission spectrum during titration with an optical quencher. This devised procedure and model provide a straightforward means of measuring the L_D of materials in NP morphologies. This chapter applies and discusses measurement methods for L_D. Difficulties in measuring P3HT film L_D due to changes in crystallinity are described, but a full description of diffusive exciton transport in semicrystalline films of P3HT is deferred until chapter 4, after description of a model for disordered P3HT single chains in chapter 3.

Optical Spectra and Exciton Diffusion in Thin Films of Poly(3-hexylthiophene)

Introduction

Conjugated polymers in thin films display complex optical spectra which may involve resolution of vibrational peaks. In semicrystalline polymers such as P3HT, the absorption spectra displays components of amorphous and crystalline material.[50] Spectra can be drastically different in films of chemically similar polymers with some variation, e.g. different molecular weight or regioregularity.[10] In the emission spectrum of polymer films, diffusion of excitons before emission may cause emission to be from a preferential population of sites, e.g. lower energy sites.[118]

In this chapter, the dependence of the optical spectra on film thickness and the effects of exciton diffusion when the films are placed on a substrate which quenches emission are discussed. This results in the ability to infer L_D. Measurements of L_D in a single thin film is performed with success, but fitting a model across a range of film thicknesses is not possible using this method.

Experimenal Methods

P3HT (Rieke Metals Sepiolid 200, >95% rr, 20-30kD, PDI=2.0) was dissolved in chloroform or ortho-dichlorobenzene (DCB) at a concentration of ~5 mg/mL. Films were spin-cast from the same chloroform or DCB solution onto glass slides with a 1 cm^2 piece of HOPG attached using double sided tape near a corner of the glass slide. Approximately 0.5 mL of solution was placed on a slide. It was then spun until dry at 1400 rpm for chloroform casting or 600 rpm for DCB casting. ultraviolet-visible (UV-Vis) spectra were taken using a Varian Cary 50 spectrophotometer. Fluorescence spectra were taken using a Horiba-Yvon Nanolog Fluorimeter in front facing mode with an angle of 30^o of incline from the impinging beam in

order to reduce reflections from the HOPG surface. Films were aged under inert atmosphere (anhydrous Nitrogen), but removed to perform fluorescence measurements.

Film thicknesses were initially measured using step-profilimetry for three films (~15-70 nm) and compared with absorption spectra to determine the thin film extinction coefficient at 540 nm with good agreement between films. Subsequent film thicknesses were calculated from absorbance at 540nm and a calculated thin film extinction coefficient of 0.019 nm^{-1}. Film casting solutions were diluted to prepare films of varying thickness. Annealing of films was performed under inert atmosphere when described.

Thin Film Optical Spectra

Dependence of Film Crystallinity on Solvent. The solvent used to spincast a film of conjugated polymer can induce different amounts of crystallinity within the film.[50] In this study, chloroform or DCB are used to dissolve the P3HT before spincasting. It has been shown that chloroform produces a significantly more amorphous film than chlorinated benzene solvents, which produce higher crystallinity films in the following series; chlorobenzene, DCB, trichlorobenzene.[119] This aggregation could be due to induced π-stacking by folding of chains in solution.

Absorption Lineshape of Spincast Films. Using chloroform and DCB indeed produces different lineshapes (Figs. 2.1 and 2.2). The lineshape of DCB cast films has more defined vibronic peaks. This infers that reduced inhomogeneous broadening is observed in DCB cast films. Although not necessarily representative of increased crystallinity, this suggests higher intramolecular order in the P3HT films cast from DCB than chloroform. This could be caused by, e.g., π-stacking of DCB and polymer chains in solution, resulting in decreased disorder in

twist angles of polymers in ordered crystal-like structures in films. Importantly, the ratio of 0-0 to 0-1 vibronic peaks increases as film thickness is increased in both Fig. 2.1 and Fig. 2.2.

Annealing of films spin-cast from DCB (110 ºC/10 min.) has very little effect on the absorption spectrum (Fig. 2.2). Due to the conclusions of Spano described in chapter 1, this implies that the crystallinity is not changed. These films are thinner than commonly used in a BHSC. Annealing of binary mixtures of fullerenes and P3HT for BHSCs has been shown to increase device efficiency.[120] If P3HT behaves in such a binary mixture as it does in these thin films, increased crystallinity may be due to phase separation effects rather than increased crystallinity.

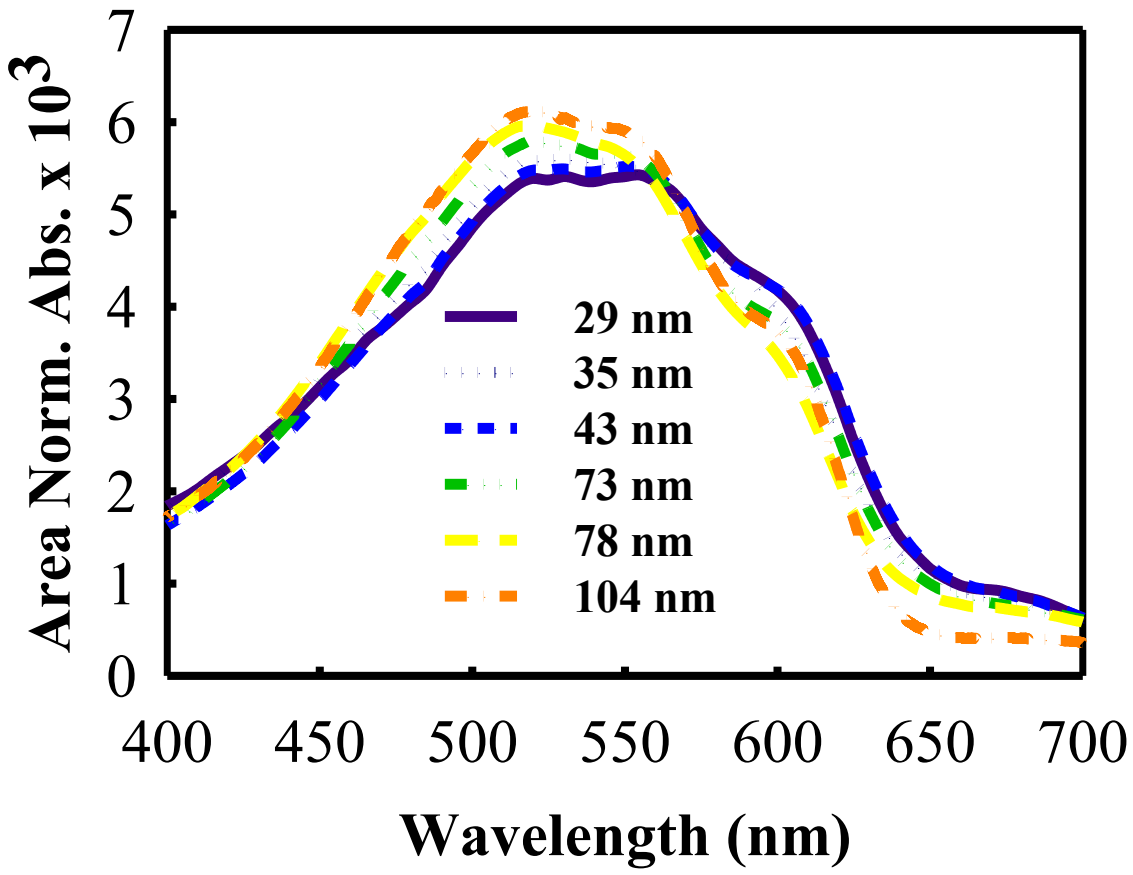

Figure 2.1. Optical absorption spectra of films spincast from chlorform on glass using various concentrations to change film thickness. Film thickness, as measured from the optical absorption spectrum and extinction coefficient, is given in the figure legend in nanometers.

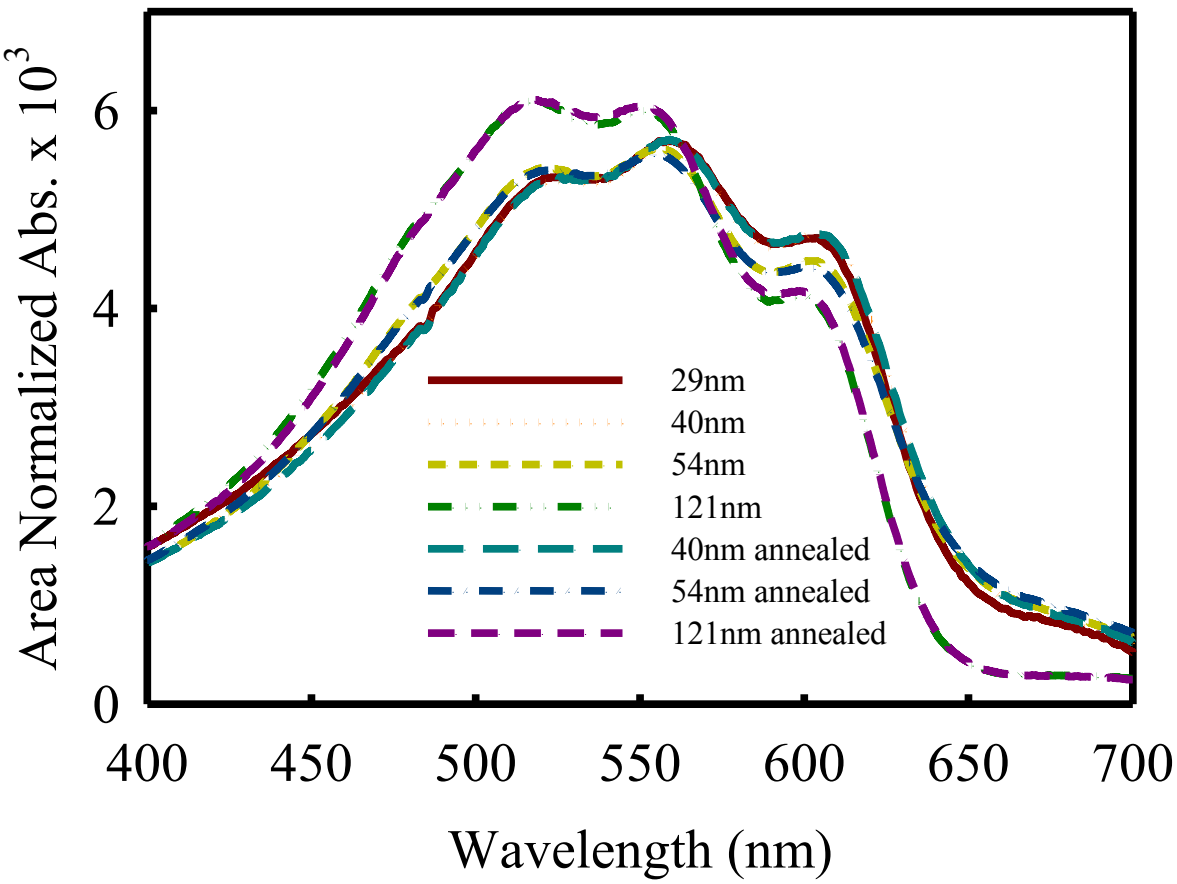

Figure 2.2. Optical absorption spectrum of P3HT films spincast from DCB on glass substrates before and after annealing for 10 min. at 110 ºC. Film thickness, as measured using the calculated extinction coefficient for P3HT films, is given in the figure legend.

Emission Lineshape of Spincast Films. The ratio of 0-0 and 0-1 peaks decreases in the emission lineshape while it increases in the absorption lineshape (Figs. 2.3 and 2.4). In the case of films cast on HOPG, quenching of PL occurs. For this reason, HOPG has been used in L_D measurements later in this chapter.[121] Due to the low PL quantum yield of P3HT in thin films (~0.003)[122] and the quenching of excitons by HOPG, the emission intensity is very low, so experimental spectra were smoothed for comparison (Figs. 2.3 and 2.4). Upon annealing of films spin-cast from DCB, very little change in the emission spectra for all but the thinnest measured film is observed (Fig. 2.3).

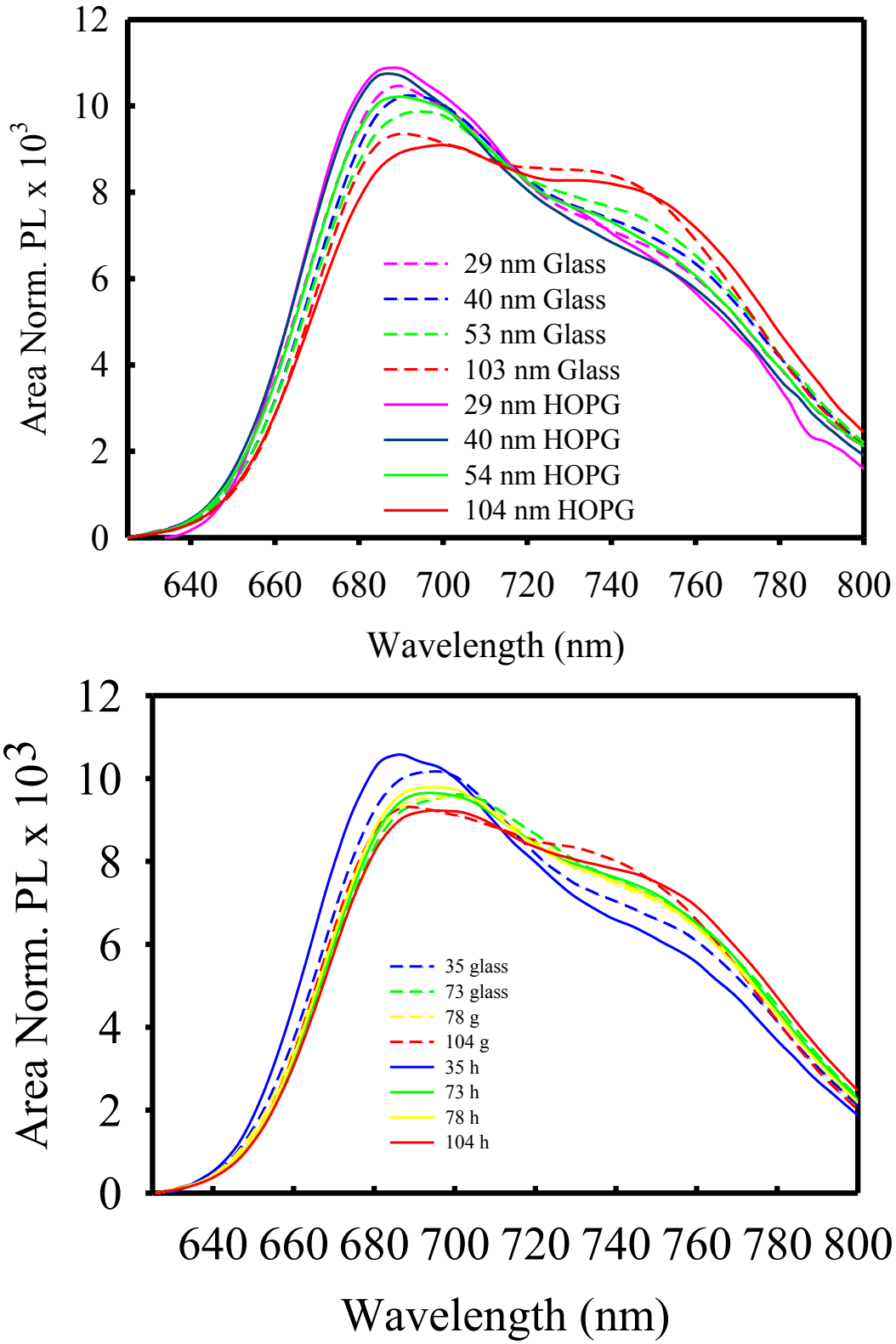

Figure 2.3. Optical emission spectra of P3HT films on glass and HOPG substrates as spincast from DCB (Top) or chloroform (Bottom) solution. Film thickness is given in the figure legend. g: glass, h: HOPG.

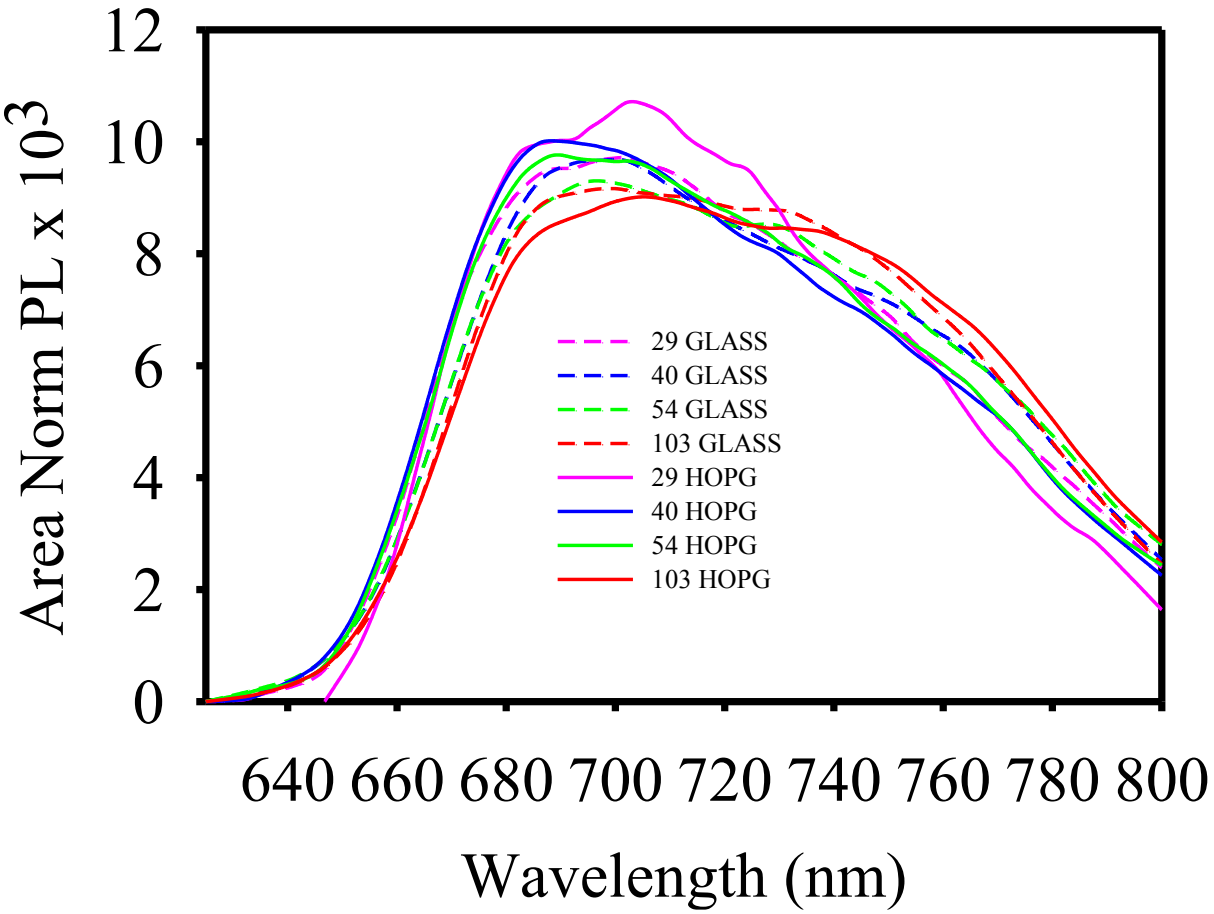

Figure 2.4. Optical emission spectrum of P3HT films on HOPG and glass substrates as spincast from DCB solution after annealing. The film thickness is given in the figure legend in nanometers as calculated from the film absorption spectrum.

It is clear that magnitude of the ratio of intensity of 0-0 to 0-1 peaks increases in the absorption spectrum and decreases in the emission spectrum as film thickness is increased for films spin cast from either chloroform or DCB. Through the conclusions of Spano et al. described in chapter 1, these results imply that the film crystallinity increases as film thickness increases. A possible explanation for the increased crystallinity is the higher concentration of solution used to spin cast thicker films. Higher concentration may induce a higher rate of crystalline formation during solvent evaporation.

Change in Emission Intensity during Film Drying. The maximum emission intensity of films varies with time for more than one hour and depends on the type of substrate on which

the film is cast (Fig. 2.5). Beginning at initial film casting, the emission intensity reduces to 50% of the initial value after 15 min. Upon ageing under inert atmosphere and thermal annealing of the sample some additional reduction in emission intensity is observed.

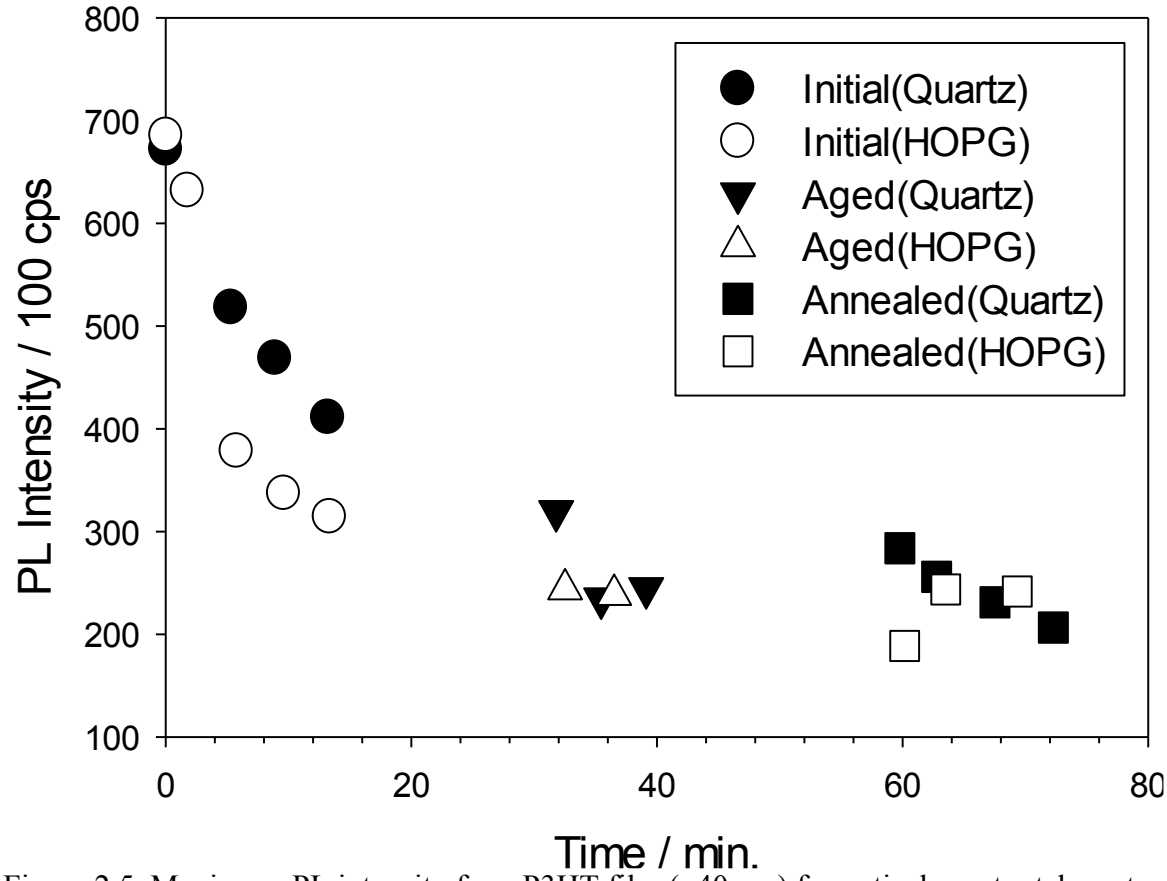

Figure 2.5. Maximum PL intensity for a P3HT film (~40 nm) for optical spectra taken at various times under ambient conditions on quartz and HOPG substrates. Films were aged for 20 minutes under nitrogen and anhydrous conditions in the first gap, then annealed for 20 minutes under anhydrous nitrogen atmosphere at 110 ^{o}C during the second gap.

The emission intensity of films of P3HT spin cast on glass (quartz) and HOPG have varying emission intensity. P3HT cast on HOPG is known to quench excitons at the boundary between the P3HT film and HOPG.[56,123] Hence, for films of comparable thickness, the emission intensity is expected to be reduced on the HOPG surface. As shown later in this chapter, the ratio of emission intensities for films of the same film thickness can be related to L_D.

The reduction in emission intensity over time must be caused by factors on a long (minute) timescale. Two factors are immediately apparent which might cause reduced emission efficiency. First, thin films of P3HT have a much lower emission efficiency than in solution (0.003 in film vs. ~0.1 in solution)[51,121,122], so drying of the film may cause the emission efficiency to be reduced by, e.g., intermolecular ordering of the polymer that might occur during drying. Second, ordering of P3HT chains can occur on longer time scales and may occur also during film drying. This may also cause reduced efficiency by increased exciton diffusion, thereby increasing the possibility that an exciton reaches a site that causes nonradiative decay.

Exciton Diffusion Length Measurements

It is frequently assumed that excitons in amorphous organic semiconductors such as P3HT undergo isotropic diffusive transport. In such a case, a continuity equation can be applied to model the exciton density (η)

$$\frac{d\eta(x,t)}{dt} = D\frac{d^2\eta(x,t)}{dx^2}. \qquad \text{(Eq. 2.1)}$$

The diffusion coefficient *D* is related to the diffusion length through Eq. 1.1. It will now be shown how the ratio of fluorescence intensities can be related for thin films on quenching substrates and non-quenching substrates by solving a diffusion equation with appropriate boundary conditions. Measurements of fluorescence quenching occurring at an interface with HOPG are performed at a steady state, so the time derivative becomes zero. However, three additional terms are necessary in order to accurately describe the diffusion in this system.[51] These are, in the order given on the right hand side of Eq. 2.2, finite exciton lifetime, resonant energy transfer from the conjugated polymer layer to HOPG and exciton generation (excitation) density. This can be written as

$$D\frac{d^2\eta(x)}{dx^2} = \frac{\eta(x)}{\tau} + \frac{\rho_A R_0^6 \pi \eta(x)}{6x^3} - G(x) \qquad \text{(Eq. 2.2)}$$

where τ is the exciton lifetime, ρ_A is the acceptor density of HOPG, R_0 is the characteristic Forster radius of energy transfer[124] and *G(x)* is the excitation density. In the case of Forster resonant energy transfer (FRET) between a donor and a three dimensional array of acceptors, the dipole-dipole coupling term of FRET theory has a cubic dependence on distance.[73] Addition of this FRET term makes analytical solution of this equation difficult and the exciton density is approximated numerically.[16–18]

When calculating $G(x)$, optical interference effects can be important when the film is not optically thick and the refractive indices of the mediums are very different. An example of this is the case of ~50nm thick films of P3HT on HOPG (quenching) or polystyrene (nonquenching) substrates (Fig. 2.6). Using the well known transfer matrix approach, interference effects are accounted for with scattering matrices according to the complex refractive indices of the various layers.[48] In contrast, several studies have used a simple exponential decay of light intensity in the active layer (Beer-Lambert law). If the Beer-Lambert law was used to model the steady state exciton generation rate, an error would be introduced in the calculation of the L_D with magnitude depending on the thicknesses of the films studied. In the case of very thin films, this effect can usually be neglected.[51] The comparison of the calculated exciton density with experimental emission spectra will now be described.

Measurements are performed on layered structures in which the active layer (P3HT) is spin coated in a thin film upon a quenching substrate (HOPG) or nonquenching substrate (glass slide). Therefore, appropriate boundary conditions for Eq. 2.2 correspond to complete quenching at the P3HT/HOPG interface and complete blocking at other interfaces, i.e. $\eta(0) = 0$ and $\left.\frac{d\eta}{dx}\right|_d = 0$, respectively, where *d* is the film thickness. An example exciton density profile calculated using the parameters given in Table 2.1 for a P3HT film on HOPG is shown in Fig. 2.6.

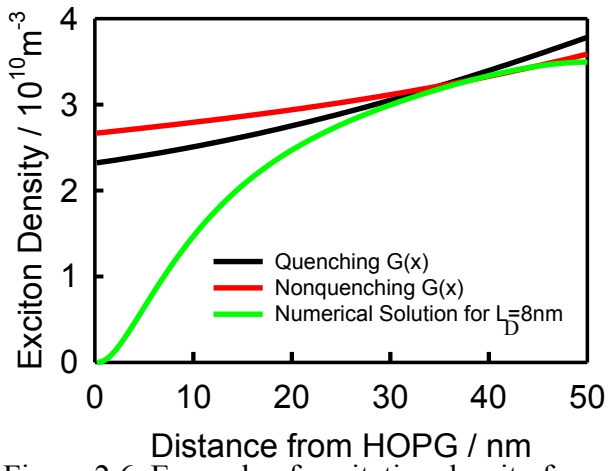

Figure 2.6. Example of excitation density for quenched and nonquenched films and numerical solution of Eq. 2.3 for P3HT films of 50 nm on HOPG or polystyrene substrates.

Table 2.1. Parameters for exciton diffusion model.

Parameter	***Value***	***Reference***
ρ_A	4 nm^{-3}	Calc'd
R_0	2.345 nm	Calc'd
τ	470 ps	125
QE	0.3%	126
$\tilde{\eta}_{HOPG}$	3.011 + 1.725i	127
$\tilde{\eta}_{Polystyrene}$	1.572	128
$\tilde{\eta}_{P3HT}$	1.625+0.3i	129

For a film on an nonquenching substrate, the steady state exciton density is calculated from Eq. 2.2 by neglecting the FRET term and enforcing the boundary conditions $\left.\frac{d\eta}{dx}\right|_d = 0$ and $\left.\frac{d\eta}{dx}\right|_0 = 0$, yielding

$$\int_0^d \eta_{nq}(x)dx = \tau \int_0^d G_{nq}(x)\,dx. \qquad \text{(Eq. 2.3)}$$

In these measurements, the quenching efficiency is measured as a function of film thickness (d) and compared with theoretical values using the following equation

$$1 - \phi_Q \approx \frac{I_q}{I_{nq}} \approx \frac{\int_0^d \eta_q(x)dx}{\tau \int_0^d G_{nq}(x)dx} \qquad \text{(Eq. 2.4)}$$

where ϕ_Q is the quenching efficiency of the HOPG substrate and I_q and I_{nq} are the emission intensities of quenched and nonquenched films, respectively. This has been found to have little effect on the accuracy of the measurements in similar layered structures. The exciton density in the quenching structure $\eta_q(x)$ is calculated from numerical solution of Eq. 2.2

A three dimensional plot of $1 - \phi_Q(L_D,d)$ is displayed in Fig. 2.7. It shows the transition to low quenching at larger film thicknesses. In theory, these curves could be fit to experimental data at different film thicknesses (such as in Fig. 2.7) as has been done in several previous studies.[51,56] However, in practice this is difficult due to the large standard deviation in measured values. From Fig. 2.7, it can be seen that a small variation in the curve of quenching efficiency and film thickness can result in a large deviation in the measured L_D. It would require many measurements to obtain accurate results from this method. .

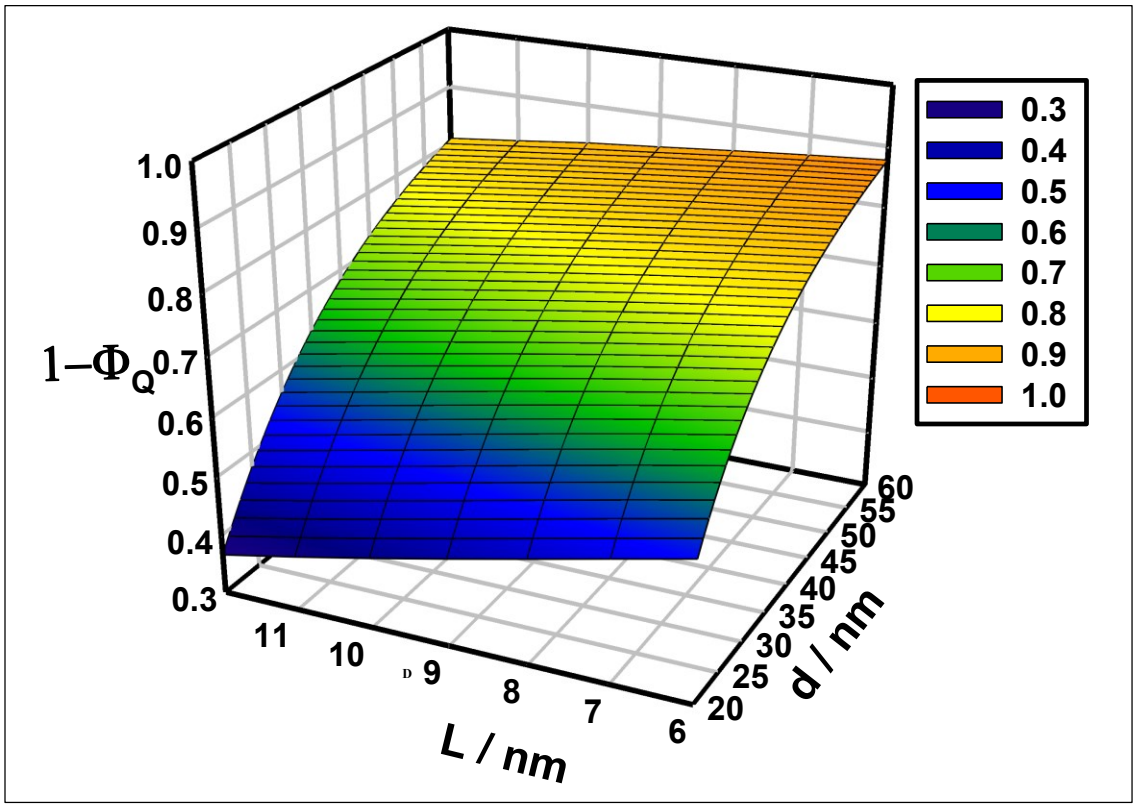

Figure 2.7. Solution to Eq. 2.4 for P3HT films on HOPG and glass substrates. This relates the quenching efficiency to diffusion length and film thickness.

Experiments were performed with varying film thickness. The results of these experiments (maximum emission intensity) are shown in Fig. 2.8 at two different excitation wavelengths. To make a measurement of L_D, numerical solutions of Eq. 2.4 (Fig. 2.7) would be fit to the points in Fig. 2.8. However, it is apparent that these experiments do not produce results which can give accurate fit to the exciton diffusion model.

Another experiment was performed using a single thin film (42 nm) and measuring the emission intensity over time (Fig. 2.9). This resulted in data which could be compared with Eq. 2.4. In this case, films on glass and HOPG were interchanged in a fluorimeter every 2-3 minutes and the emission intensity at 670 nm was recorded three times and averaged. The films were annealed under inert conditions at 110^{o}C for 10 minutes. Then, the measurement process was continued. The resulting plots were fit with lines corresponding to the emission intensity before and after annealing. From the ratio of the fitted lines, L_D was calculated according to Eq. 2.4. The calculated L_D is ~8-9 nm before annealing and ~14-18 nm after annealing. Although calculated L_D decreases with time, this observation may be a coincidence of fitting lines to data with significant deviation from linearity.

A complication of using this method arises when considering the results of examining the optical spectra of thin films at the beginning of this chapter. There, it was concluded that film crystallinity changed with film thickness. The details of how crystallinity and polymer conformation affect optical properties are discussed later in this dissertation. In chapters 3, it is shown how optical spectra vary between crystalline and disordered P3HT and in chapter 4 the effects of crystallinity on L_D is simulated. Since L_D is affected by the film microstructure, these effects should be accounted for or experiments could be modified in order to include them.

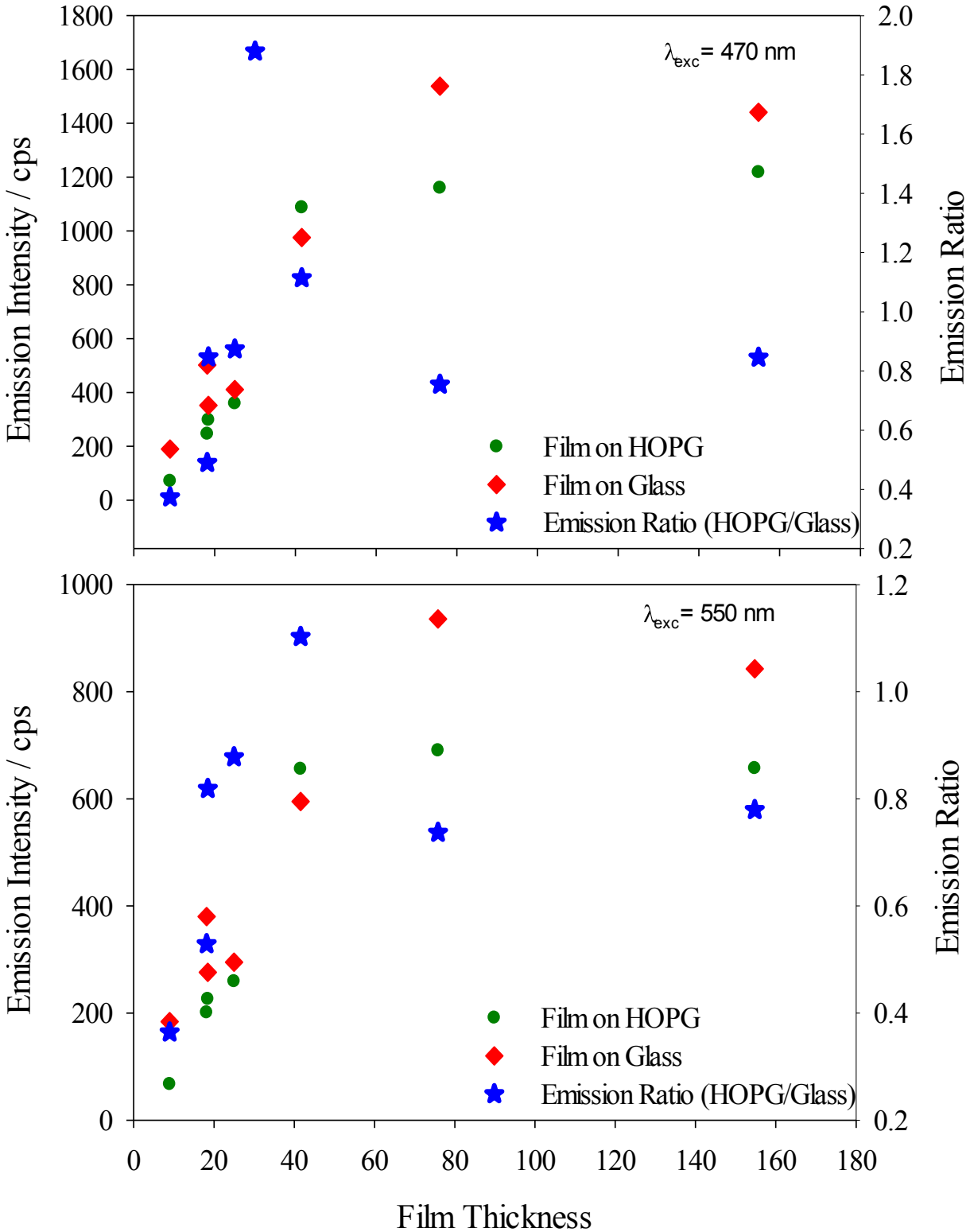

Figure 2.8. Emission intensity of P3HT films spincast from $CHCl_3$ on Glass and HOPG substrates with excitation wavelength at 470 nm (Top) or 550 nm (Bottom). Film Thickness is given in nm. The ratio of emission on HOPG/Glass is also pictured.

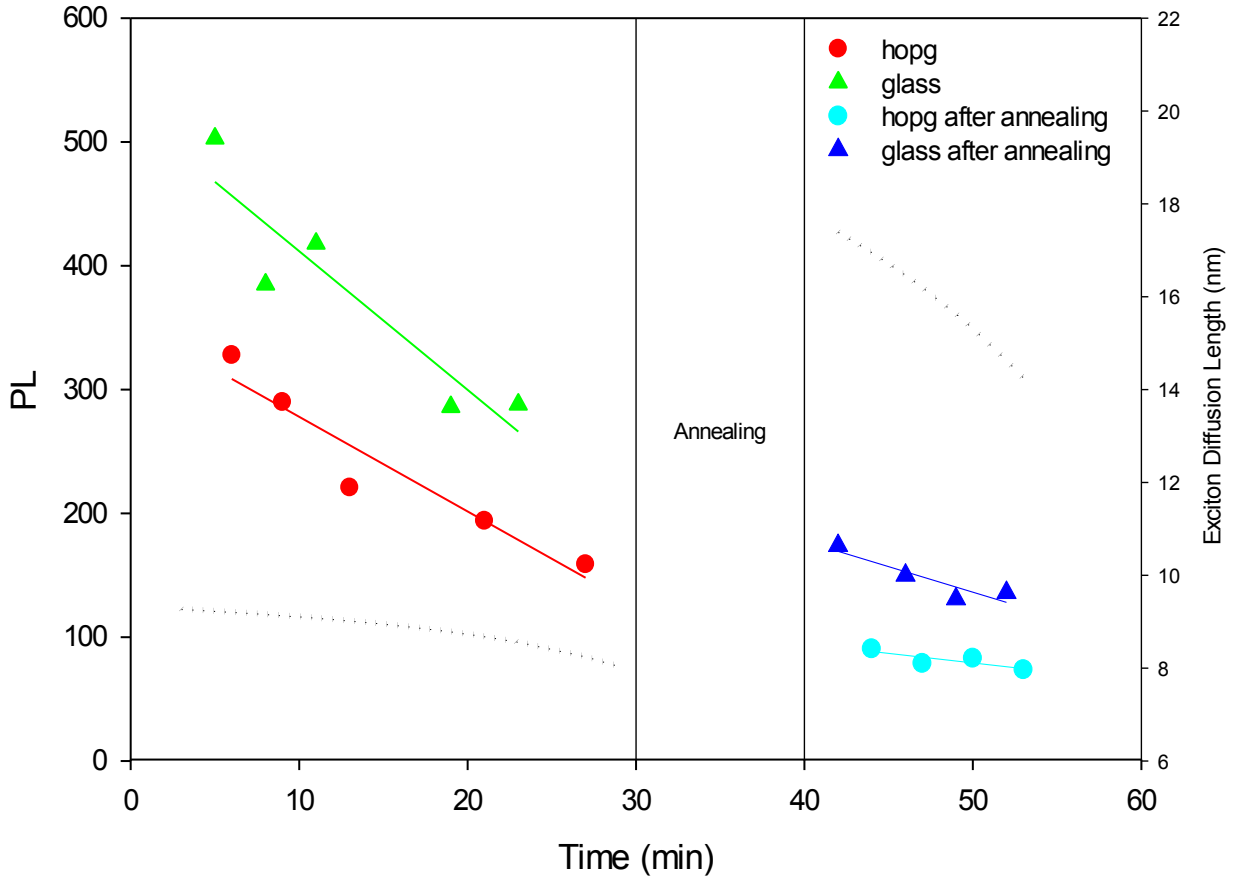

Figure 2.9. Maximum PL intensity for P3HT film excited at 540 nm (~42 nm thick film) on glass (green/blue triangles) and HOPG (red/blue circles) substrates before and after annealing under dry-box conditions for 10 minutes at 110 ºC. Exciton diffusion length (dotted line) is then calculated from the ratio of lines fit to PL intensities according to Eq. 2.4.

Discussion of Methods of Exciton Diffusion Length Measurement. A variety of methods of measuring L_D exist in the literature. In several examples, fullerenes have been used as a quenching layer. However, significant molecular diffusion eliminates the well-defined boundary between layers and may introduce significant error into the measurements. This problem was solved by Denis et al. by using a cross-linking fullerene derivative as a quenching layer to measure L_D for poly(phenylvinylene) derivatives.[130,131] However, the quenching mechanism in this system involves electron transfer and may accumulate significant charge at the boundary. This has been shown to have a significant effect on exciton quenching in isolated

polymer chains.[38] HOPG has a structure which prevents molecular diffusion and is thus favorable for the presented measurements.

A significant problem with most exciton diffusion length measurements is the amount of material required. For example, in Figure 2.9, nearly 10 mg of material were used. However, it is clear several times this amount would be required to reduce measurement error to acceptable levels. This amount of material is too much for newly synthesized polymers, which are of primary interest in L_D measurement.

One scheme to address this issue involves a spectrally resolved method where the variation in the extinction coefficient of the material at various wavelengths is exploited.[132] In this case, the material is excited at a range of wavelengths which are absorbed to varying extent by the polymer film. This creates an effect similar to changing the film thickness by changing the pattern of excitation within polymer films. In this case, a model similar to that presented here can be used with a wavelength dependent exciton generation function, $G(x,\lambda)$, giving a better estimate of L_D in comparison to using a single thin film.

Another method involves time-dependent PL measurement at high intensity, thus inducing a process which quenches PL when two excitons combine.[133] From the magnitude of this effect at various intensities, L_D can be determined. Still another involves creating a donor-acceptor heterojunctions of varying domain size and extracting the domain size of the highest PV efficiency.[134] Each method predicts varied results.

The overall problem with L_D measurements is the lack of consistency when treating the same polymer. Unfortunately, this is likely to be caused by the intrinsic variability of polymer films, especially semicrystalline films where crystallite variation and disorder can strongly affect

L_D. Seen in Table 2.2, it is rare for two measurements to agree. However, it's clear that the L_D in most conjugated polymer films is 5-30 nm. These effects are explained in chapter 4.

Table 2.2. References measuring exciton diffusion length for polymer or polymer/fullerene films, polymer, quencher used for measurement and measured value.

Ref.	*Polymer (Details)/Quencher (Details)*	*L_D(nm)*	*Film Thickness (nm)*
[51]	MDMO-PPV/Titania	6±1	0-15
[135]	NRS-PPV/C_{60}	28	24-170
[130]	NRS-PPV/C_{60} (cross linked)	5±1	3-65
[43]	LPPP/C_{60} derivative (blended)	6	-
[4]	LPPP/C_{60} derivative (monolayer)	14	-
[53]	P3HT (92%RR)/TiO_2	5.3/2.4	0-30
[52]	P3HT (98.5% RR, MW=76kD PD=2.1)/TiO_2	8.5±0.7	-
[133]	P3HT (98.5% RR, MW=76kD PD<2)/None	27±12	-
[56]	P3HT(93% RR)/HOPG	8±2	0-70

Another issue these methodologies is that other conjugated polymer morphologies, e.g. NPs, solvated nanocrystals, or epitaxially grown spherulites, are not applicable to these methodologies. These morphologies cannot be prepared in a uniform thin film, as required by existing L_D measurements. This issue is addressed in the remainder of this chapter, where a method for measuring L_D in conjugated polymer NPs is presented.

Methodology for Measuring Exciton Diffusion Length in Conjugated Polymer Nanoparticles

Introduction

Stable aqueous NP dispersions of conjugated materials can be prepared easily using well known methodologies. No method for measuring L_D exists for conjugated polymer NPs without incorporating acceptor in the conjugated polymer matrix.[136] This causes quenching of excitations to a degree which is dependent on the material's L_D, similar to measurements of films on quenching substrates. However, inclusion of quenching dyes into a matrix of conjugated materials alters the packing of molecules and affects L_D. If the measurement requires various embedded dye concentrations, the measured L_D may be drastically affected.

A method by which to measure L_D in NPs without disturbing the polymer matrix is given in this section. This is performed by measuring NP emission with quenching by colloidal aggregation of dye molecules on NP surfaces and extracting a measure of L_D by comparison with a model describing diffusion and quenching in a NP ensemble.

Methodology and Results

Nanoparticle Preparation. MEH-PPV (Sigma-Aldrich 541435, 70-100kD) was used as received. NPs were prepared by the reprecipitation technique.[137] Well dissolved 2 mg/mL tetrahydrofuran (THF) solution was rapidly injected into millipore water through a very narrow diameter needle during sonication, followed by partial vacuum evaporation of THF. The NP solution was then filtered through 450 nm pore size filters.

Atomic Force Microscopy. To determine NP sizes, atomic force microscopy (AFM) was performed with a Dimension 3100 Nanoscope IIIa using a 10 nm diameter platinum tip with resonant frequency of 47-76 kHz and force constant of 1.2-6.4 N/m. Samples were prepared from 100-fold diluted solutions of NPs in millipore water and vacuum dried overnight onto glass substrates.

Vertical cross sections of non-aggregated NPs were obtained from AFM scans. Using the mean position of the vertical cross section of individual NPs as the NP center, the distance from the NP center which includes 95% (by area) was used as the NP radius. By considering only the central 95% of a NP scan, the curvature and size of the AFM tip are accounted for in the final calculation of NP radii. The resulting radii were then fit with a Gaussian function to calculate a mean radii of 28 nm and standard deviation of 5 nm. The AFM image and nanoparticle radius distribution are shown in Fig. 2.10.

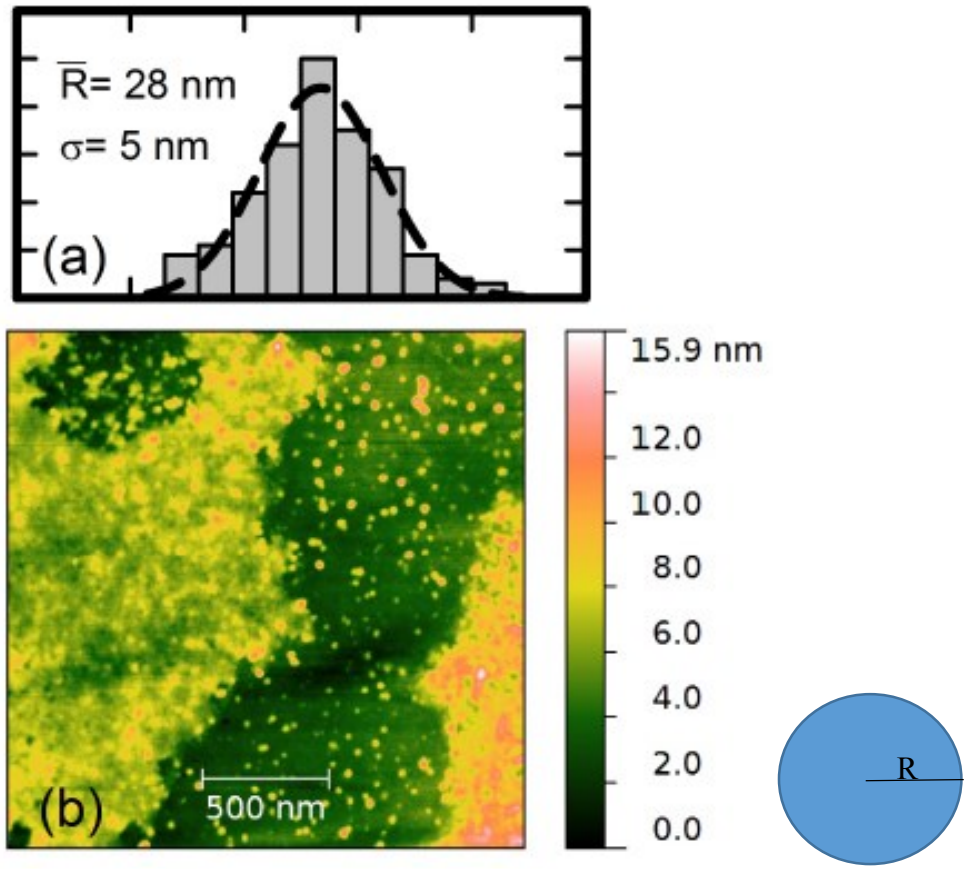

Figure 2.10. (a) Distribution of particle radii determined from AFM counted in 3 nm bins and fit by a Gaussian distribution with mean radius and standard deviation σ. (b) AFM image of vacuum dried NP with mean radius of 28 nm on glass. Regions of nonaggregated NPs were used for determining the size distribution. Definition of *R* is given.

Quenching Experiments. Subsequent additions of small aliquots of 0.3 mM dye stock solution were added directly to a fluorescence cuvette containing NP solutions and carefully mixed. methylene blue (Ricca Chemical Company) and cresyl violet Acetate (MP Biomedicals, LLC) were used as received. Absorbtion and emission spectra were collected with a Cary WinUV Spectrophotometer and Horiba Jobin-Yvon Nanolog Fluorimeter at an excitation wavelength of 500 nm. Inner filter effects were accounted for using a multiplicative correction factor (C.F.) calculated with measured molar extinction coefficients of the acceptors at excitation (ε_A) and emission wavelengths (ε_E);[73]

$$C.F. = 10^{C_A(\varepsilon_A+\varepsilon_E)/2} \quad \text{(Eq. 2.5)}$$

Due to the well known high singlet oxygen yield of photoexcited methylene blue, a series of preliminary quenching experiments were first carried out under deoxygenated conditions and subsequently under ambient conditions. Noting that solutions of MEH-PPV NPs and methylene blue show no change in the amount of NP emisson quenching compared with the results of experiments carried out under ambient conditions, it was inferred that oxidative damage of MEH-PPV NPs does not occur in the presence of acceptor dyes. Further experiments were carried out under ambient conditions.

Factor Analysis. Due to significant overlap of dye and NP emission spectra, deconvolution was performed by factor analysis using non-negative matrix factorization[138] and rotation of the resulting factors onto the experimental spectra of the neat components using Procrustes factor rotation.[139] Cresyl violet dominates the recorded spectra at lower concentrations than methylene blue due to higher fluorescence quantum efficiency (55% vs. 4%).[140] Thus, deconvolutions of higher dye concentrations were possible for experiments with methylene blue than with cresyl violet. After factor analysis and rotation, the reconstructed spectra reproduce the experimental spectra with high accuracy, while rotated factors are nearly identical to the experimental spectra of the neat components.

Lifetime and Quantum Yield. Fluorescence quantum efficiency (Φ_F) was calculated using 25 μM Rhodamine 6G/EtOH as reference[141] according to

$$\Phi_F = \Phi_R \frac{A_R(\lambda) I_F n_F}{A_F(\lambda) I_R n_R} \quad \text{(Eq. 2.6)}$$

where $A(\lambda)$ is the absorbance at excitation wavelength λ, I is the integrated PL, n is the refractive index of the medium and subscripts R and F stand for the reference chromophore and analyte, respectively.[73]

Time-correlated single photon counting experiments were performed to determine the lifetime of the quenched and unquenched NPs with a nanosecond pulse diode in a Horiba Jobin-Yvon Fluorimeter. Excitation was carried out at 340 nm and emission was recorded at 590 nm. Transients are well fit by a biexponential curve. A subnanosecond lifetime accounts for >98% of the decay curves and a 3-5 nanosecond decay accounts for the remainder. The subnanosecond decay is attributed to the singlet lifetime of MEH-PPV. Lifetime measurements were performed using a separately prepared NP sample of unknown size distribution. Upon adding quencher, the lifetime is reduced (Fig. 2.11).

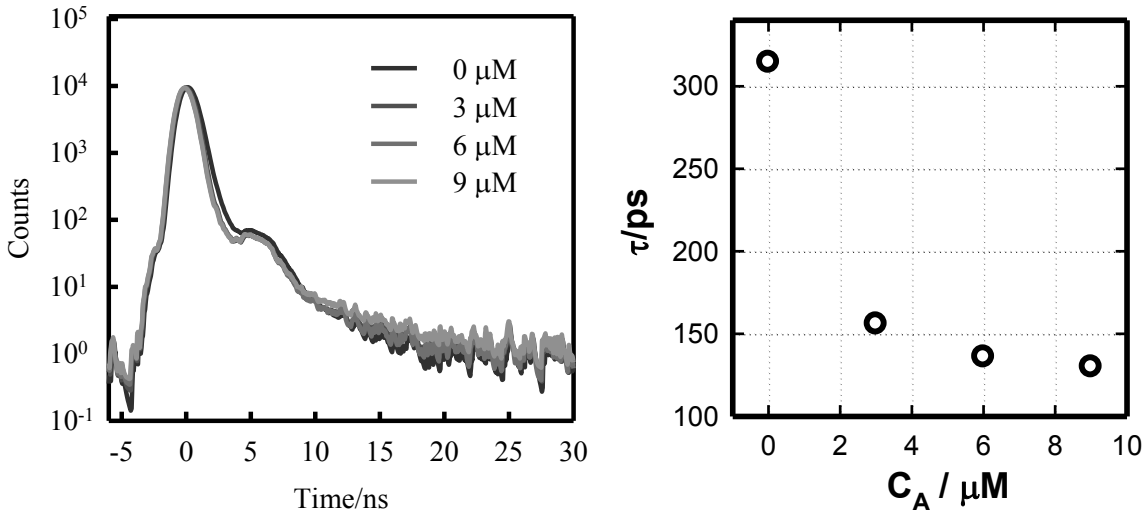

Figure 2.11. Lifetime measurement of MEH-PPV NPs from time-correlated single-photon counting. (Left) Plotted transients with various methylene blue concentrations. (Right) Fitted lifetime measurement. Measurement error is smaller than the displayed markers. MEH-PPV lifetime is reduced by addition of quencher dye on a similar scale as the reduction of integrated emission in steady-state PL measurements.

Experimental Results. The aggregation of cationic dye molecules on MEH-PPV NP surfaces is supported by the observed amplified quenching in titration experiments. Well known

in conjugated polyelectrolytes, two factors contribute to amplified quenching. First, the formation of a static quenching complex occurs between donor and acceptor. Second, intra- and inter-chain energy migration in the conjugated polymer allows one acceptor to quench many donors.[142] In the presented experiments, MEH-PPV NPs function as a collection of many donors in which energy migration occurs, while aggregated dyes function as acceptors. The interaction between NPs and cationic acceptors is presumed to be electrostatic. Indeed, the zeta potential of similar MEH-PPV NPs has been measured at -40 mV at neutral pH,[143] supporting aggregation of cationic acceptors arround MEH-PPV NPs.

Methylene blue and cresyl violet were chosen as quencher dyes due to strong overlap between dye absorption and MEH-PPV NP emission spectra (Fig. 2.12), solubility in water, and ability to electrostatically interact with prepared NPs. To estimate the concentration of NPs (C_{NP}) from optical absorption and NP size distributions, (assuming that NPs exhibit the same extinction coefficient as in spin-coated thin films of ~0.03 nm^{-1} at λ_{max}[144], the following equation was used;

$$C_{NP} = \frac{A(\lambda)}{Nl\varepsilon(\lambda)}[\int_0^\infty V(R)\Omega(R)dR]^{-1} = \frac{A(\lambda)}{Nl\varepsilon(\lambda)}\frac{3}{4\pi}[\overline{R}^3 + 3\overline{R}\sigma^2]^{-1} \qquad \text{(Eq. 2.7)}$$

where the equation on the right is given for a Gaussian distribution of spherical NPs, $\varepsilon(\lambda)$ is the thin film extinction coefficient of the material at wavelength λ, l is the path length of the cuvette, N is Avogadro's number, $V(R)$ is the volume of a NP with radius R and $\Omega(R)$ is the probability density function for the occurrence of a given R. This equation gives approximate C_{NP} of 20 pM. The maximum surface density of acceptors (that is, when all added acceptors are aggregated on the NP surface), ρ_A, at a given acceptor concentration (C_A) is given by,

$$\rho_A = \frac{C_A}{C_{NP}}[\int_0^\infty S(R)\Omega(R)dR]^{-1} = \frac{C_A}{C_{NP}}[4\pi(\overline{R}^2 + \sigma^2)]^{-1} \qquad \text{(Eq. 2.8)}$$

where *S(R)* is NP surface area and the right-hand side is again given for a Gaussian distribution of spherical NPs. Maximum acceptor surface densities for 1 μM quenching dye are calculated to be 5 nm^{-2}. Considering the acceptor size, this calculation clearly supports the notion of NP surface saturation at μM dye concentrations.

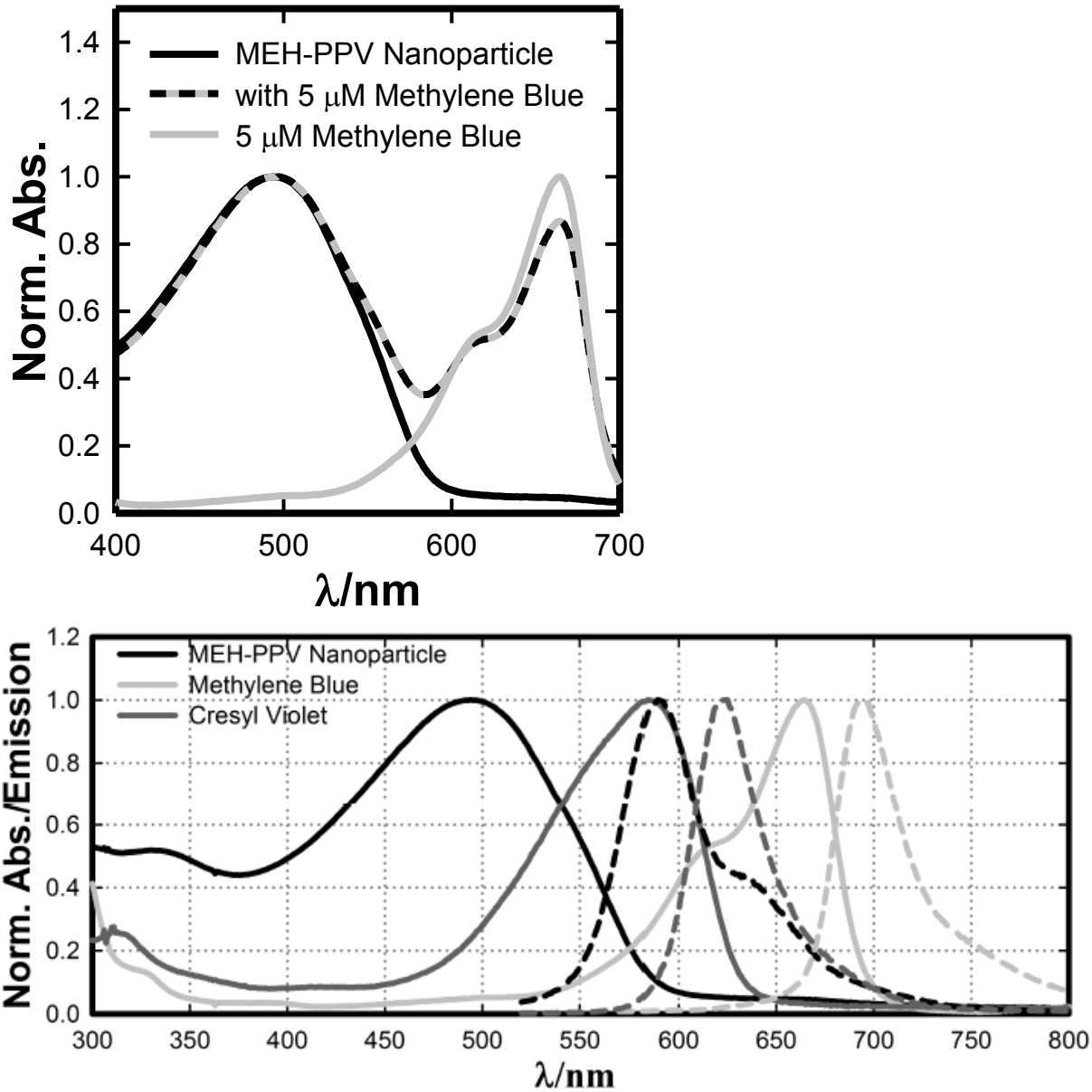

Figure 2.12. (Bottom) Normalized optical absorbance (solid) and emission (dashed) spectra of methylene blue, cresyl violet, and MEH-PPV Nanoparticles. There is significant spectral overlap between MEH-PPV NP emission and the absorption spectra of dyes. (Top) Normalized absorbance spectrum of MEH-PPV NP with $\overline{R} = 28nm$, 5 μM methylene blue, and MEH-PPV NP with 5 μM methylene blue.

The Stern-Volmer (SV) relationship is a linear relationship between the amount of quenching and acceptor concentration. The standard SV relationship is given by,

$$\frac{I_0}{I} = 1 + k_{SV} C_A \qquad \text{(Eq. 2.9)}$$

where $I_0(I)$ is the integrated PL in the absence(presence) of acceptor and k_{SV} is the SV constant describing the dependence of quenching on C_A. The current quenching experiments do not fulfill the linearity of this equation. Rather, SV plots are strikingly nonlinear with negative curvature (Fig. 2.13).

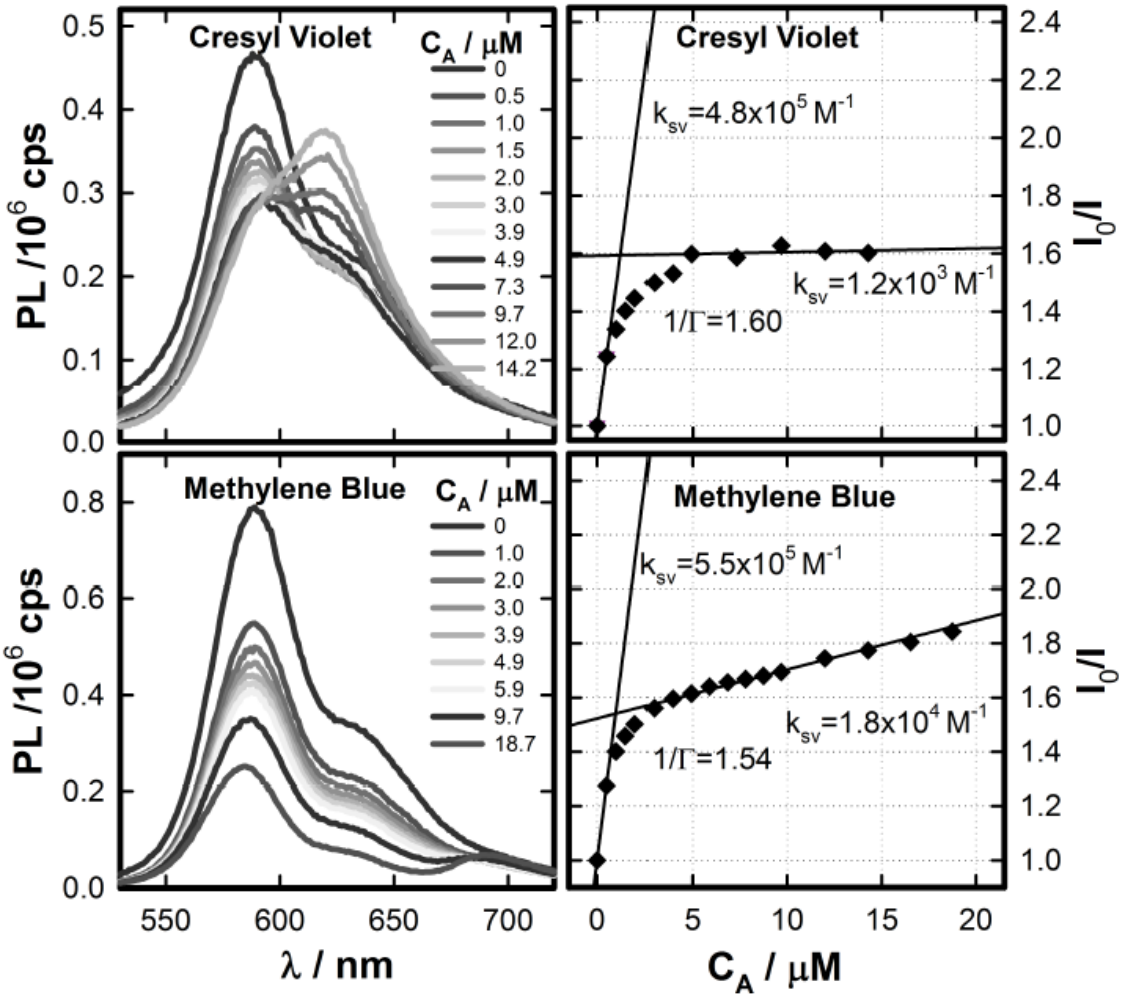

Figure 2.13. Emission spectra (Left) and Stern-Volmer plots (Right) of quenching experiments conducted using MEH-PPV NPs quenched with methylene blue (Bottom) or cresyl violet (Top). Extrapolated lines are used to estimate the quenching at saturation (Γ) when the NP surface is saturated with quencher dyes.

Lines tangent to curves in SV plots are used for estimates of k_{SV} at specific acceptor concentrations. Initial quenching occurs with k_{SV} greater than 10^5 M^{-1}, indicating amplifed quenching by complexation. Between acceptor concentrations of 1-5 μM, an order of magnitude reduction in k_{SV} is observed. This change is interpreted as saturation of the NP surface with acceptor dyes. From the intersection of lines fit in these two regions of Stern-Volmer plots, the efficiency of quenching after saturation of the NP surface with dye molecules (Γ) can be obtained.

In higher concentration regions of SV plots, quenching with cresyl violet has lower k_{SV} than quenching with methylene blue. As dye loading increases, inner filter effects not accounted for in the SV plots may cause the observed reduction in PL after saturation of the NP surface. Since methylene blue has a higher extinction coefficient than cresyl violet, inner filter effects are stronger in experiments with methylene blue, giving higher k_{SV} after saturation of the NP surface with quencher dyes.

The lifetime and emission efficiency of unquenched MEH-PPV NPs (measured at $\tau = 314$ ps and Φ_F=2.3%) are similar to literature values of 200-300 ps[145] and 3%[146] reported for MEH-PPV thin films. This suggests that the environment of chromophores in these two nanomorphologies is similar, supporting comparison between L_D in MEH-PPV NPs and thin films.

Upon addition of quencher dye, the MEH-PPV emission lifetime (τ) is decreased (Fig. 2.11). Static quenching (donor-acceptor association) should not exhibit a reduction in τ upon increased acceptor concentration, since the lifetime of nonquenched chromophores will not be affected. Excitons with longer lifetime are more likely to diffuse farther and therefore have a higher probability of being quenched before radiative decay. In the present case, the dynamic

nature of energy migration within the NP causes lifetime reduction even while association is present.

Exciton Diffusion Model for Nanoparticles

In the previous section, the density of excitons was described by a modified form of the diffusion equation (Eq. 2.2). A similar equation is applied here;

$$\frac{\partial \eta}{\partial t} = D\nabla^2\eta(\vec{r}) - \tau^{-1}\eta(\vec{r}) + k_G \qquad \text{(Eq. 2.10)}$$

where $\eta(\vec{r})$ is the exciton density in spherical coordinates with origin at the NP center. On the right hand side of Eq. 2.10, the first term accounts for exciton diffusion, the second term for nonradiative decay, and the third term accounts for the rate of exciton generation per unit volume (k_g). Here we assume that k_g is spatially homogeneous, which is well suited to describe NPs with diameter much smaller than the penetration depth of incident light. In the steady state $\frac{\partial \eta}{\partial t} = 0$.

Assuming spherically symmetric NPs,

$$\nabla^2 = 2r^{-1}\frac{d}{dr} + \frac{d^2}{dr^2} \qquad \text{(Eq. 2.11)}$$

where r_D indicates the distance from the NP center. Combining Eqs. 1.1, 2.10 and 2.11 with $\frac{\partial \eta}{\partial t} = 0$ and defining $L=L_D/(2d)^{1/2}$ to simplify expressions, the steady state exciton density can be determined by solving

$$L^2(2r^{-1}\frac{d}{dr} + \frac{d^2}{dr^2})\eta(r) - \eta(r) + \tau k_G = 0 \qquad \text{(Eq. 2.12)}$$

Boundary conditions describing quenching at the surface of the NP with efficiency γ can be constructed using Fick's first law at the NP surface, given by;

$$J_R = -D\frac{d\eta}{dr}\bigg|_R \qquad \text{(Eq. 2.13)}$$

where J_R is the magnitude of diffusive exciton flux at the NP surface. This flux can be related to the change in exciton density and one dimensional exciton velocity (v) by

$$J_R = v\Delta\eta(R) = \sqrt{2}\frac{L}{\tau}\Delta\eta(R)\,. \qquad \text{(Eq. 2.14)}$$

The change in exciton density at the boundary due to quenching, $\Delta\eta(R)$, is related to the quenching efficiency by $\Delta\eta(R) = \eta(R-dr) - \eta(R) = \frac{\gamma}{1-\gamma}\eta(R)$ because $\eta(R) = (1-\gamma)\eta(R-dr)$, so J_R can be expressed as

$$J_R = \sqrt{2}\frac{L}{\tau}\frac{\gamma}{1-\gamma}\eta(R) \qquad \text{(Eq. 2.15)}$$

which gives the following boundary condition when combined with Eq. 2.13,

$$L(1-\gamma)\frac{d\eta}{dr_D}\bigg|_R + \sqrt{2}\gamma\eta(R) = 0 \qquad . \qquad \text{(Eq. 2.16)}$$

Also applying a second boundary condition,

$$\frac{d\eta}{dr}\bigg|_0 = 0\,, \qquad \text{(Eq. 2.17)}$$

as a result of spherical symmetry gives the following solution for $\eta(r)$,

$$\eta(r) = k_G\tau[1 - \frac{\sqrt{2}\gamma R^2}{r}\frac{e^{\frac{r}{L}} - e^{-\frac{r}{L}}}{\gamma_+ e^{\frac{R}{L}} - \gamma_- e^{-\frac{R}{L}}}] \qquad \text{(Eq. 2.18)}$$

where $\gamma_\pm$ is given by $\gamma_\pm = [(\sqrt{2}\mp 1)\gamma \pm 1]R + (\gamma - 1)L$. The effect of quenching efficiency on the exciton density is shown in Fig. 2.14, while a comparison of exciton density for 100% and 50% quenching efficiency at various L is shown in Fig. 2.15.

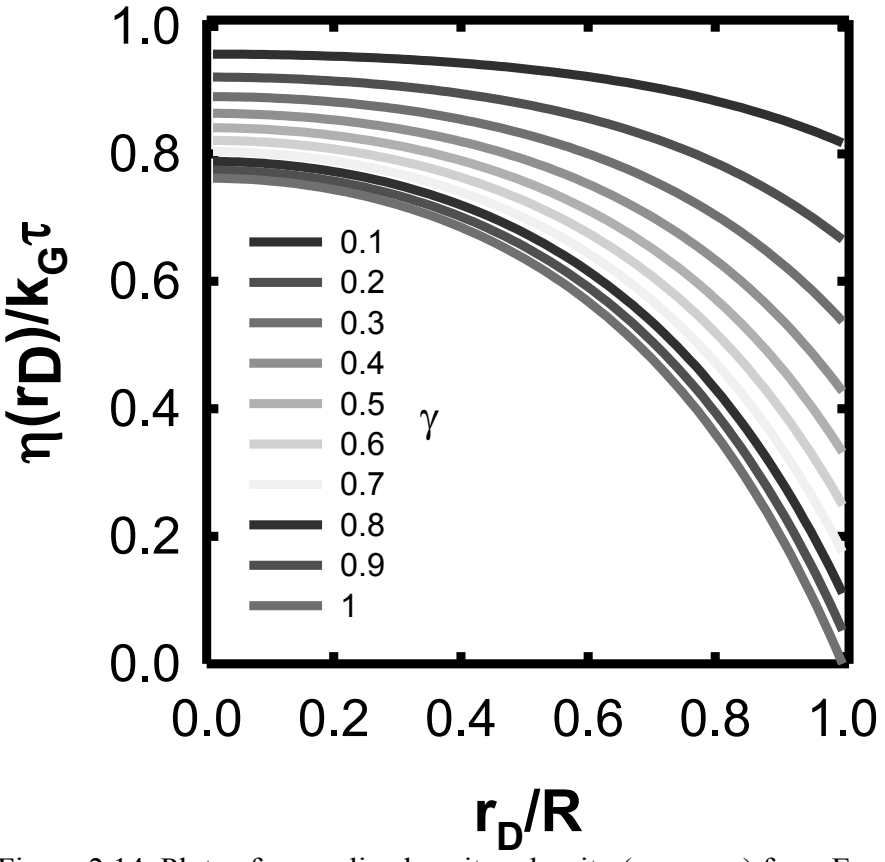

Figure 2.14. Plots of normalized exciton density ($\eta(r_D)/k_G\tau$) from Eq. 2.18 with L, R, and r scaled by $1/R$ at constant L =0.3R for various quenching efficiencies.

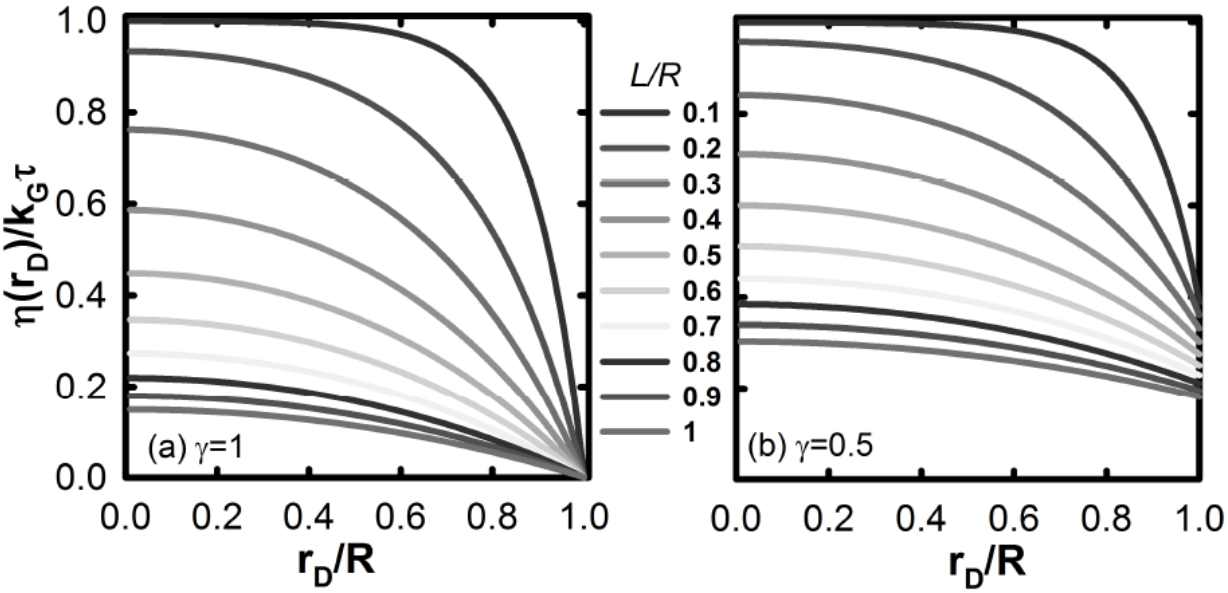

Figure 2.15. Plots of normalized exciton density ($\eta(r_D)/k_G\tau$) from Eq. 2.18 with L, R, and r scaled by $1/R$ for various L at 100% quenching efficiency (a) and 50% quenching efficiency (b).

The integrated emission intensity is related to the radial exciton density for a given NP radius, $\eta(r,R)$, by

$$I \propto \int_0^R \int_0^\infty \eta(r,R)\Omega(R)4\pi r^2 dRdr \quad . \qquad \text{(Eq. 2.19)}$$

In the absence of a quencher, this becomes

$$I_0 \propto 4/3\pi k_G \tau(\overline{R}^3 + 3\overline{R}\sigma^2) \qquad \text{(Eq. 2.20)}$$

for a Gaussian distribution of NP sizes. The ratio of Eqs. 2.19 and 2.20 eliminates the proportionality constants in these equations and connects measured quenching from SV plots with the physical model incorporating exciton diffusion.

These equations can be integrated numerically, but it is useful to find a simple solution for the limiting case of 100% quenching efficiency. First, we integrate over *r* in Eq. 2.19 with γ=1 in Eq. 2.18 to derive the following expression for the integrated emission intensity of a monodisperse NP distribution;

$$I_{\gamma=1} \propto 4/3\pi k_G \tau R^3 - 4\pi k_G \tau RL(R\coth(R/L) - L). \qquad \text{(Eq. 2.21)}$$

For $R>2L$, coth(R/L) is close to 1 and can be set to unity. Then, performing the second integration over a Gaussian distribution in Eq. 2.19, followed by division by I_0 from Eq. 2.20 results in

$$\Gamma \approx 1 - 3\frac{L(\overline{R}^2 + \sigma^2) - L^2\overline{R}}{\overline{R}^3 + 3\overline{R}\sigma^2} \ , \qquad \text{(Eq. 2.22)}$$

which gives

$$L \approx \frac{\sqrt{3}(R^2 + \sigma^2) - \sqrt{(4\Gamma - 1)R^4 + (12\Gamma - 6)\sigma^2 R^2 + 3\sigma^4}}{\sqrt{12}R}. \qquad \text{(Eq. 2.23)}$$

This provides a simple expression for calculating *L*, assuming that quenching occurs with 100% efficiency and meeting the condition $R > 2L$.

Numerical integration of the exact solution (Eq. 2.18) in Eq. 2.19 for fits of Gaussian functions to NP size distributions is shown in Fig. 2.16 for various quenching efficiencies. Using the actual size distribution measured from AFM scans does not result in significant deviation from calculations using the fitted gaussian functions. From the numerical integration of the exact solution with γ=1, average L of 4.2±0.2 nm are calculated. Within experimental error, the approximate solution (Eq. 2.23) gives quantitatively identical result.

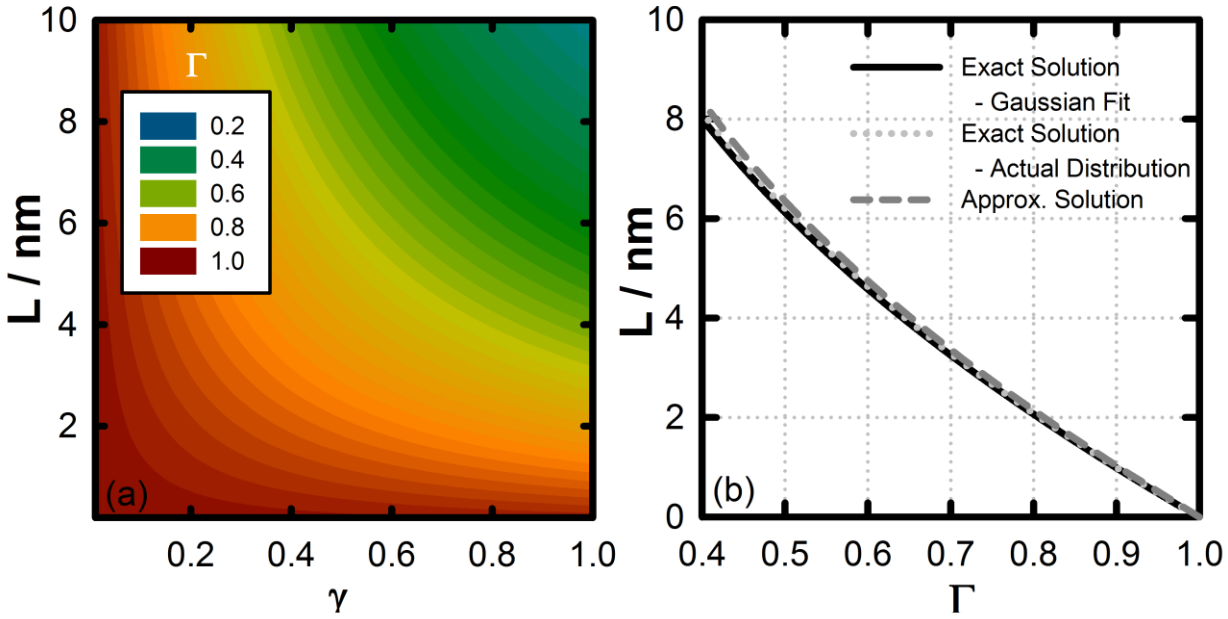

Figure 2.16. (a) Contour plot of simulated quenching from numerical integration of Eq. 2.18 in Eq. 2.19 for a Gaussian distribution of NP radii. The plot shows the dependence of L on the efficiency of quenching. (b) Model given by Eqs. 2.18 and 2.19 with numerical integration over both the fitted Gaussian function and measured distribution of nanoparticle sizes, further compared with approximate solution (Eq. 2.23) using $\bar{R}$ =28 nm and σ=5 nm.

In the case of NP surface saturation by dye molecules, quenching of MEH-PPV emission at the NP boundary is assumed to occur with high efficiency. However, it is important to examine the effects of quenching efficiency on measured L_D. For γ=0.8, the calculated L_D is 4.7±0.3 nm. Averaging over all quenching efficiencies greater than 80% gives a reasonable estimate of L assuming that many acceptors are aggregated on the NPs. Measured L are then 4.5±0.5 nm, corresponding to three dimensional L_D of 12±1 nm assuming quenching

efficiencies between 80-100%. This is close to the lowest reported L_D in thin films of MEH-PPV.[43,130,147]

Conclusion

This method for measuring L_D requires particle size measurement and quenching experiments with an appropriate acceptor. The measured Γ can then be used in Eq. 2.23 to extract L_D, as long as the mean NP radius is at least twice as large as L and the distribution of NP sizes is approximately Gaussian. In other cases, numerical solution of generalized model equations allows any NP size distribution to be used.

This measurement was performed using MEH-PPV nanoparticles, which are known to be amorphous.[137] In the case of P3HT, these measurements may provide a method of examining the effect of semicrystalline structure on the exciton diffusion length, since methods exist for precise control of crystallinity in conjugated polymer NPs. In chapters 3 and 4, the effects of crystallinity on exciton diffusion are explored with computational models.

POTENTIAL OF THE TWIST ANGLE AND OPTICAL EFFECTS OF INTRAMOLECULAR DISORDER

Since measurements of L_D give only an averaged (macroscopic) picture of exciton transport, it is necessary to formulate a microscopic picture. To do so requires an atomistic description of the involved polymers. To begin, it is necessary to identify the most important nuclear degree of freedom (DOF) for disorder in the nuclear structure. For P3HT, a single DOF has been clearly implicated in terms of optical properties, the twist angle (Fig. 1.3).[21,148,149] This disorder, the absence of which occurs in crystallites, can be used to simulate an ensemble of polymers and their optical properties, as performed in this chapter. The method used to construct disordered polymer chains is then used in chapter 4 to simulate disordered dimers for exciton diffusion simulations.

Twisting of the Polymer Backbone: Torsional Potential of the Twist Angle

Introduction

The twist angle is defined as the angle of torsional rotation around a bond connecting polymer building blocks and was defined in Fig. 1.3. It is the most important nuclear DOF in many conjugated molecules because it has, in many cases, the most prominent effect on the optoelectronic properties at room temperature.[21,34,148–151] For example, later in this chapter it will be shown that the twist angle can have a strong effect on the calculated excitation energy of the $S_0 \rightarrow S_1$ transition, changing its energy by as much as 50%. Other properties which may be affected by the twist angle include conjugation length, excitation energy and the electronic coupling between two molecules. It is not surprising that recent strategies for controlling the optoelectronic properties of conjugated molecules have focused on constraining twist angles.[152]

In this chapter, the torsional potential of twist angles in P3HT is examined in detail. Since the alkyl chains of P3HT play a limited role in π-conjugation, these alkyl chains are truncated to methyl groups in calculations. In P3HT, interaction of alkyl chains may play an important role in determining the population of twist angles in chains. For this study, the contribution of side chains is neglected. Thus, the torsional potential of the twist angle in oligo(3-methylthiophene) (O3MT) is calculated using tetramer and hexamer oligomer lengths.

It is important to note that other DOFs may be affected by choice of twist angle, i.e., bond angle and bond length may change when relaxed at fixed twist angle. However, it was found during this study that relaxed calculations with tetra(3-methylthiophene) (T3MT) show that these DOFs vary by only ~1% of their values from unconstrained optimization. However, because of the qualitative 'rigidity' in comparison to the twist angle, unrelaxed and relaxed potential energy scans are not quantitatively similar, although qualitative features are conserved. That is, unrelaxed potential energy scans include some change in energy due to variation of DOF other than the torsional potential which may be very narrow minima on the full adiabatic potential energy surface, as shown later in this section.

A general goal of modeling the torsional potential of twist angles is to model extended polymer conformations using smaller model compounds. Several other studies have examined these potentials. In the simplest case, the torsional potential of 2,2'-bithiophene has been analyzed as a model for torsional potentials in extended polythiophenes.[153–155] However, using a longer oligomer may result in a different torsional potential. For example, the torsional potential of tetrathiophene is predicted to have an increased barrier at 90^{o} due to strengthened conjugation in comparison to the 2,2'-bithiophene case.[155] The tetrathiophene potential calculated with DFT using B3LYP/6-311G** has further been used to parameterize classical forcefields and derive

accurate enthalpies and crystal structures of poly(3-alkylthiophene)s and oligo(3-alkylthiophene)s in molecular dynamics simulations.[114] Evidently, the comparison of the twist angle torsional potential of various oligomers is necessary.

The second order Moller-Plesset perturbation theory (MP2) is widely considered to give accurate results for ground state thermodynamic potentials when using reasonable basis set. For tetrathiophene, the torsional potential at the B3LYP/6-311G** level of theory has been found to be comparable to MP2/6-31G* calculations.[114] Similarly, as is shown later on we find that for an O3MT hexamer, this comparison provides good agreement.

The remainder of this section is structured as follows. First, the potential energy surface (PES) of an O3MT trimer is examined over the DOF corresponding to the two twist angles between thiophene units to determine the extent of coupling between twist angles. Then, the effects of solvent on the torsional potential of the central twist angle of O3MT tetramer and hexamer are investigated with a polarized continuum solvent model (PCM) in conjunction with DFT simulations.

Conjugated polymers are frequently more chemically complex than P3HT, as many literature examples show. A brief departure from the focus of this chapter on P3HT concludes this section by modeling twist angles in polymers with several chemical building blocks.[112] This reveals interactions between carbonyl- and methoxy- groups on polymer building blocks which may cause a phenomena termed “conformational locking” and demonstrates the possible complexity of the twist angles in conjugated polymers other than P3HT.

Computational Methods

Calculations of the twist angle torsional potential were performed for tetramer and hexamer of O3MT at the B3LYP/6-311G** level of theory. For these calculations, the optimized

geometries were used and the central twist angle was varied. At each value of the central twist angle, a single point calculation was performed. The level of theory was chosen because of the known agreement[114] between the tetramer at MP2/6-31G* and B3LYP/6-311G** and the similarly observed agreement for the hexamer in the following calculations. The continuum solvation model used was the default in Gaussian '09. This solvent model requires both a solvent radius and dielectric constant.[156]

Since one of the main goals of the studies in this thesis are to simulate exciton transport in condensed phase conjugated polymers (performed in chapter 4), a solvent with similar dielectric constant to P3HT films was selected (diethylether). For tetraramer, calculations with default parameters for chloroform were also performed. Chloroform is a common solvent used with P3HT and other conjugated polymers. In all calculations, the gas phase optimized geometries were used with hexyl chain replaced with a methyl group, i.e. for poly(3-methylthiophene) (P3MT). The $\vec{c}$-axis value given in Fig. 1.5 was calculated from this gas phase optimized tetramer geometry. All calculations are performed with the Gaussian '09 program suite.[157]

Results and Discussion

Potential Energy Surface of Two Torsional Potentials. When π-systems include more than one twist angle, interaction between the twist angles are possible, i.e. the potential energies of the twist angles may be coupled.[23,24,149] For example, it is possible that breaking of conjugation by rotation around the twist angle reduces the conjugation length so that the potential energy associated with rotation around a second twist angle is modified. Another possible interaction could involve long range electrostatic interaction between units, resulting in modification of the torsional potential between two units by the twist angle to a third unit. To

examine these possible interactions in the case of O3MT, we use the tertiary oligomer as the simplest example, having only two twist angles.

First, the optimized geometry of the anti/anti conformer was determined. This corresponds to twist angles of ~150 degrees, the minimum energy conformation. Then, a rigid potential energy scan, giving a single point calculation at every variation of 15 degrees was performed beginning at $\Phi_1=\Phi_2=0$ running over π and 2π for angles 1 and 2, respectively (Fig. 3.1). There are three rotational barriers. The potential maxima at 0 and 180 degrees are a result of steric interactions between monomer units. Specifically, these steric interactions are between the closest atoms in a conformatio, i.e. S···H and S···CH_3- at 180° or S···S and H···CH_3- at 0°. The barrier at 90 degrees is a result of breaking conjugation along the polymer backbone by reduced π orbital overlap. The general shape of the potential energy curve for a single twist angle is nearly the same for all values of the second twist angle, although the base value (i.e. minimum energy on a potential energy curve of one twist angle) changes. Although this is the case for this O3MT trimer, varying potential energy curve shapes are seen for O3MT tetramer and hexamer, as shown below.

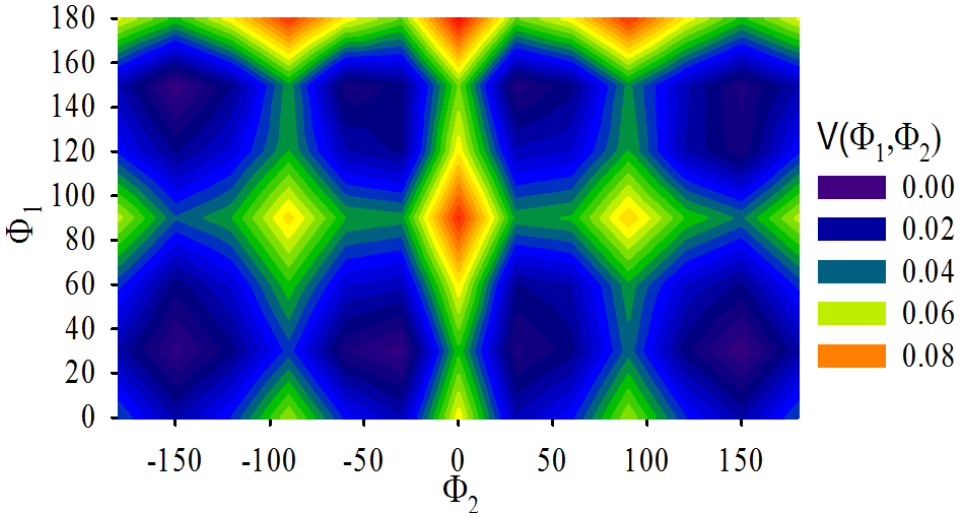

Figure 3.1. Torsional potential energy surface for the two twist angles of an O3MT trimer calculated at the B3LYP/6-311G** level of theory. Contour height is given in units of eV.

Oligomer Length/Solvent Modelling. In comparison with calculations performed without PCM, there is a decreased potential barrier at 0 degrees and increased barrier at 90 degrees when solvent is included (Fig. 3.2). The barrier at 180 degrees shows no qualitative difference. Changing the solvent parameters from diethylether (ε=4.24) to chloroform (ε=4.71) produces no qualitative change in the torsional potential (Fig. 3.3), likely becuase of the similarity of dielectric constant (ε). These solvent model results can be explained by preferred π -conjugation induced by screening of electron correlation, i.e. the repulsive coulomb interaction between electrons is reduced, resulting in stabilization of higher electron density. Further, the π-conjugation may facilitate a reduction in the dipole moment of the molecule by the solvent dielectric, thus resulting in stabilization when the conjugated backbone facilitates strong π-orbital overlap at 0 and 180 degrees, as shown in Figs. 3.2 and 3.3.

The extent of conjugation as a stabilizing factor explains the differences in torsional potentials of tetramer and hexamer. The torsional potential of the hexamer has a stronger barrier at 0 and 180 degrees as well as slightly increased barrier at 90 degrees (Fig. 3.2). The increased barrier at 90 degrees is likely due to stronger partial π-bonds during the twist angle rotation in the hexamer, rather than the tetramer. This is simply explained by an increased number of thiophene units on either side of the rotated bond (3 units vs. 2 units). The larger barriers at 0 and 180 degrees cannot be attributed to conjugation and are likely a result of geometry (of the optimized structure) and subsequent calculation of unrelaxed potential energy surfaces. Increased steric interaction between repeat units could be responsible for these barriers, i.e. the optimized geometries of tetramer and hexamer could be different enough to change the strength of steric interactions discussed above by shifting the proximity of monomers when the twist angle is 0 or 180 degrees.

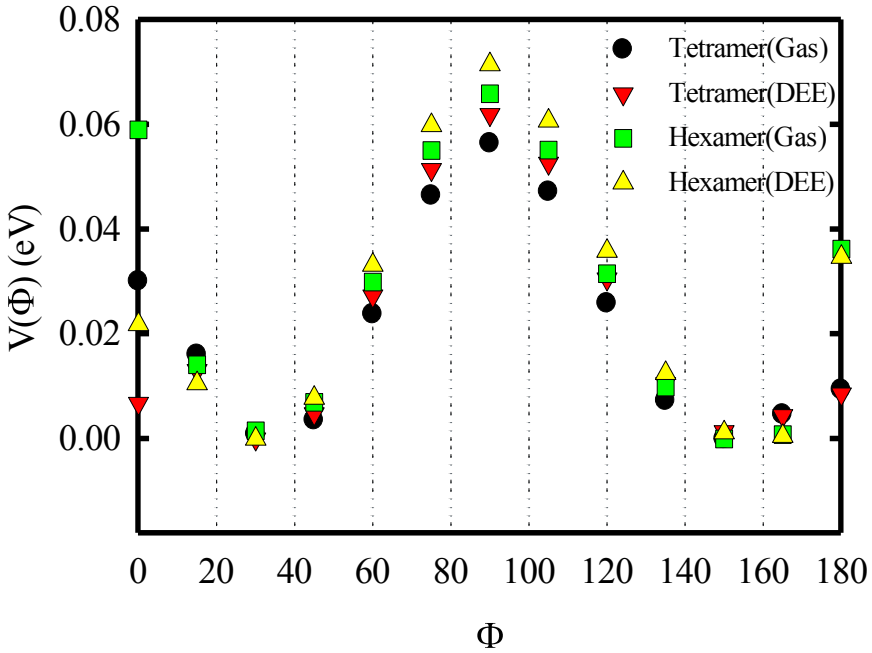

Figure 3.2. Torsional potentials calculated using DFT with B3LYP/6-311G** in either the gas phase or using the PCM for diethylether, which has a similar dielectric constant to the polymer film.

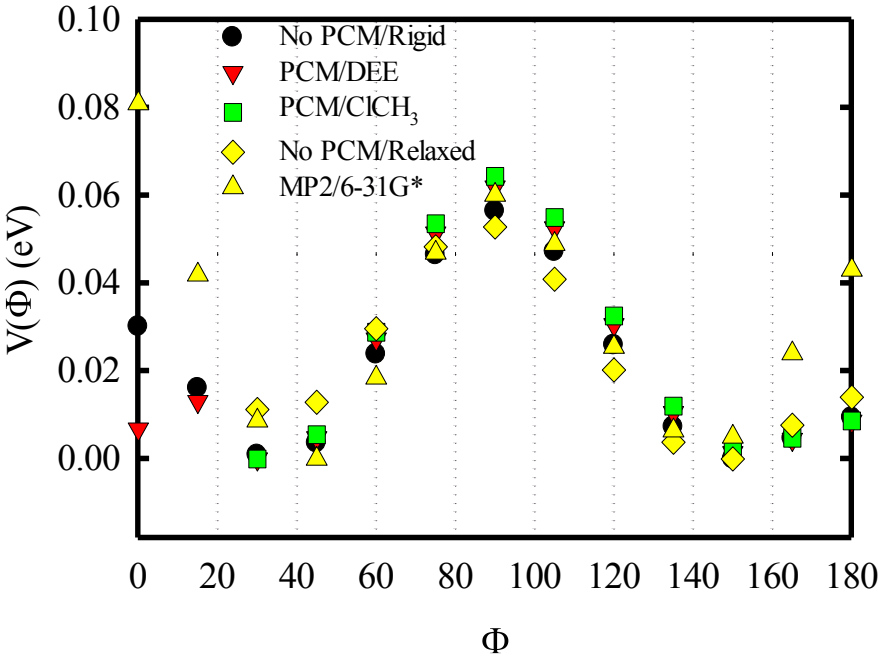

Figure 3.3. Torsional potentials of central tetramer twist angle calculated using DFT with B3LYP/6-311G**in either the gas phase or using PCM parameterized for diethylether or chloroform. Also plotted are a relaxed PES scan without solvent model for tetramer and a calculation with MP2/6-31G* for hexamer.

However, steric interaction is also seen in relaxed scans, i.e. where the geometry is relaxed at each point with the constraint of fixed twist angle (Fig. 3.3). A slightly increased barrier at the 30 degree minimum is observed, while potential barriers at 90 and 180 degrees are in near quantitative agreement. Calculations with MP2/6-31G* are very similar to calculations with B3LYP/6-311G** in Figure 3.2.

These potential energy curves show the basic elements of P3HT twist angle torsional potentials; steric interactions in planar configurations and conjugation breaking at 90^{o}. However, many conjugated polymers are more complex than P3HT, since it has only a single chemical building block. Examples of twist angles in conjugated polymers with multiple chemical building blocks and attractive interactions in planar conformations will now be discussed.

Conformational Locking. The torsional potential of the twist angles in polymer structures given in Fig. 3.4 may include attractive interactions external (but possibly inductively connected to) the π-system. In contrast, the O3MT case includes steric repulsive interactions between thiophene units. In these molecules, attractive interactions may include S···O=, H···O=,-O···H, and –O···S interactions, where –O and =O refer to sp^3 and sp^2 hybridized oxygen molecules, respectively.[20]

By examining the torsional potential, the strength and sign of the interaction are hinted at. Model compounds are used which represent various combinations of the chemical building blocks of polymers in Fig. 3.4. These calculations are performed similarly to those above, but with the B3LYP/6-31G* method. Alkyl chains are truncated in order to reduce computational time and focus on the interactions of ring structures.

The structures of model compounds used are given in Fig. 3.5. Examining the torsional potential of each possible building block dimer, two types of rotational barriers are observed.

First, torsional potentials with local minima at 0 degrees and/or 180 degrees. Second, torsional potentials with local maxima at 0 degrees and/or 180 degrees. Since the torsional potential should have a shifted minima in the absence of an attractive interaction due to steric repulsion at 0 and 180 degrees, i.e. potentials with minima at 20-30^{o}, the presence of a local minima at these values is indicative of a stabilizing effect.

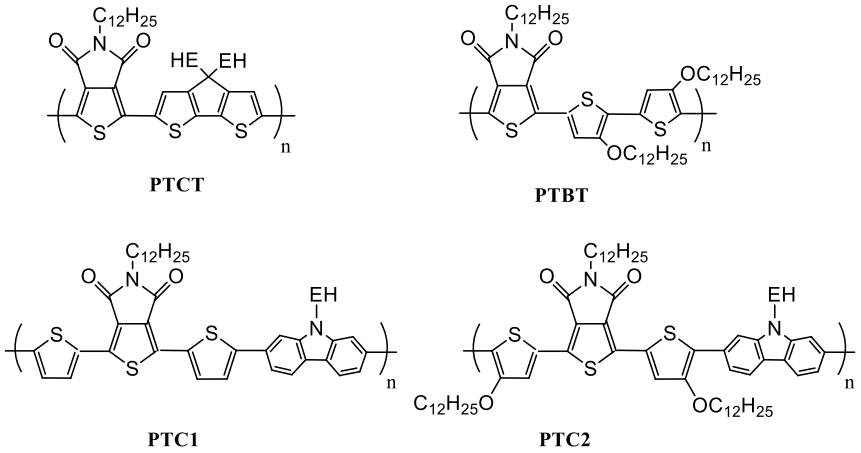

Figure 3.4. Chemical structures of conjugated polymers with multiple building blocks applied to calculations in this chapter. EH represents 2-ethylhexyl.

This stabilizing effect is likely due to the attractive interactions mentioned above. Torsional potentials at the 0 and 180 degree twist angles that contain the interactions –O···S, H···O=, S···S, and =O···S have minima at the closest proximity between atoms (0 or 180 degrees), while for H···O- and other interactions, the minima are shifted by approximately the same amount as in the T3MT torsional potential of Fig. 3.2. This value of shift in the minimum torsional potential is likely due to steric interaction between building block units. The magnitude is most likely related to the Van der Waals radii of the sterically interacting groups, e.g. H···O- and H···H, and their proximity in the planar conformation.

The difference in stabilization energy between two molecular conformations is easily observed by comparing the potential at 0 and 180 degrees. The greatest conformer stabilization

("conformational locking") occurs for heterodimers with =O···H interactions. There, the syn conformation is stabilized by ~0.1 eV relative to anti (Fig. 3.5, bottom). Heterodimers without these interactions show very little stabilization (<0.03 eV). In contrast, the T3MT torsional potential has nearly equal minima, i.e. negligible "conformational locking".

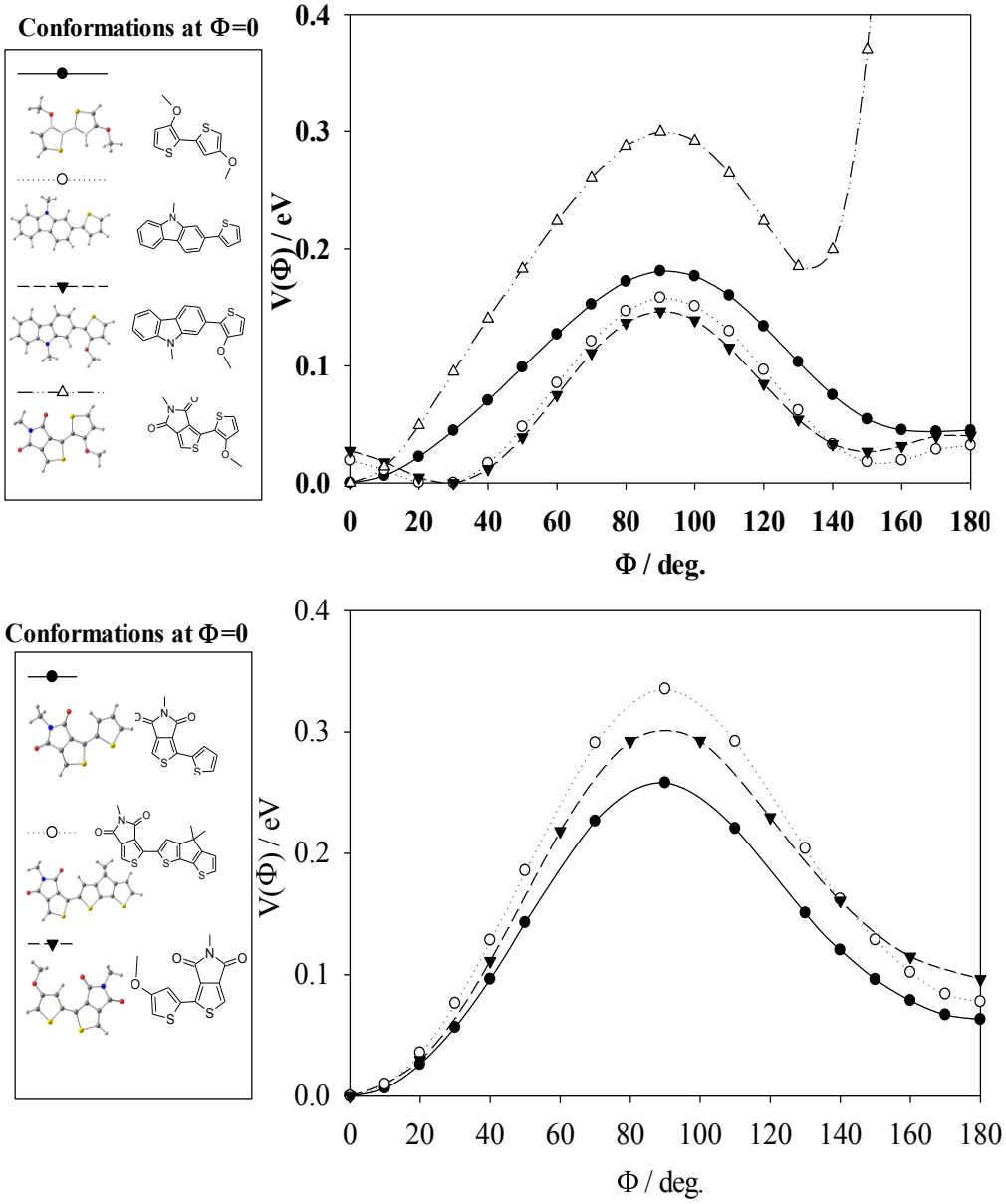

Figure 3.5. Calculated torsional potentials for sections of conjugated polymers from Fig. 3.4. Chemical structures of these sections are given in the legend at the conformation for Φ=0. Atom type is given by yellow-sulfur, red-oxygen, grey-carbon, white-hydrogen. (Top) Potentials with minima at 0 and 180 degrees. (Bottom) Potentials with other minima.

Conclusion

Torsional potentials of twist angles contain important information related to conformations of conjugated polymer backbones. Various simulation methods and oligomer sizes for O3MT were examined. General features of O3MT twist angle torsional potentials include barriers to rotation at 0, 90, and 180 degrees with minima at 30 and 150 degrees. Barriers at 0 and 180 degrees are assigned to steric interactions between 3-methylthiophene units. Including a dielectric environment in calculations through solvent modelling has the effect of slightly decreasing barriers at 0 and 180 degrees and increasing the barrier at 90 degrees. These effects are explained by strengthened conjugation. Examining heterodimers related to several more chemically complex polymers, attractive non-bonding interactions between building block units in conjugated polymer backbones decrease the potential energy of twist angle conformations. Results for heterodimers require further validation to be applied to general conclusions of polymers. In the following section, the tetramer O3MT torsional potential is used to construct polymer chains for excited state calculations.

The Effects of Twist Angle Disorder on The Optical Spectra of Poly(3-alkylthiophene)s

Reproduced in part with permission from Bjorgaard, J. A.; Köse, M. E. *J. Phys. Chem. A* **2013**, *117*, 3869–3876 Copyright 2013 American Chemical Society.

Introduction

This section presents a computational study of the localization of holes and electrons caused by twist angle disorder in P3MT during photoexcitation. P3HT is semicrystalline, having a stacked structure of ordered polymer in crystallites.[158] Thus, in crystalline domains torsional disorder is nearly absent. This has implications for optical properties which will be further explored in chapter 4. For example, it was recently discovered that L_D is relatively larger in

crystalline regions, while nonradiative relaxation is highly efficient at crystalline grain boundaries.[35] In crystalline P3HT, it is expected that chains adopt an anti conformation with planar backbone (the planar anti conformation) in order to form crystalline lammaela[70] (Fig. 1.5), while in amorphous regions static torsional disorder prevents crystalline lammaela from forming. Therefore, it is important to examine how the optical properties are affected by these conformations.

Evidence exists for low lying exciton localization through disruption of π-conjugation by disordered twist angles.[23,24,74,159] Neglecting coupling between chromophores, this would effectively create discrete chromophore units along a conjugated polymer backbone with conjugation length dictated by the distance between such defects. In the case of a single severe torsional defect in a large thiophene oligomer, conjugation breaking has not been observed in calculations using the ZINDO hamiltonian[160] (for HOMO/LUMO/transition density) or B3LYP/3-21G* (for HOMO/LUMO).[21] However, in large disordered chain calculations, the Pariser-Parr-Pople hamiltonian predicts spatial separation of low lying exciton states into discrete chromophore units.[23] In the first case, through space coupling was suggested as a cause for the absence of observed exciton localization at the torsional defect. The observation of localization in calculations on disordered polymer chains but not in chains with single defects suggests that localization occurs due to the combined effect of multiple defects. However, it is still necessary to determine the exciton size with a computational model which accurately reproduces the experimental absorbtion spectrum.

Experimentally, the solution absorbtion and emission maxima of oligothiophenes reach a polymer limit at 10-15 repeat units, i.e. the spectral peak doesn't change substantially when oligomers longer than 10-15 repeat units are measured.[12,111] This might reflect the 'particle in a

box' effect discussed in chapter 1, reflecting a maximum exciton size of 10-15 repeat units in disordered polymers. A method to compute the optical properties of disordered polymer chains will now be described.

Methodology

Disordered polymers of P3MT were constructed by a Monte-Carlo method from the geometry and torsional potential of T3MT optimized using DFT at the B3LYP/6-311G(d,p) level from Fig. 2.3. TD-DFT calculations for the lowest four excited states were performed with B3LYP[96] and the long-range corrected functionals CAM-B3LYP,[92] LC-ωPBE,[102,103] and ωB97X-D.[100]. These are compared with calculations using TD-HF. Probability densities of electron and hole are then constructed from Mulliken populations of Natural Transition Orbitals (NTOs), which give the contributions to the transition density from occupied and virtual spaces separately. These are examined over both an ensemble of disordered polymers and the planar anti conformation.

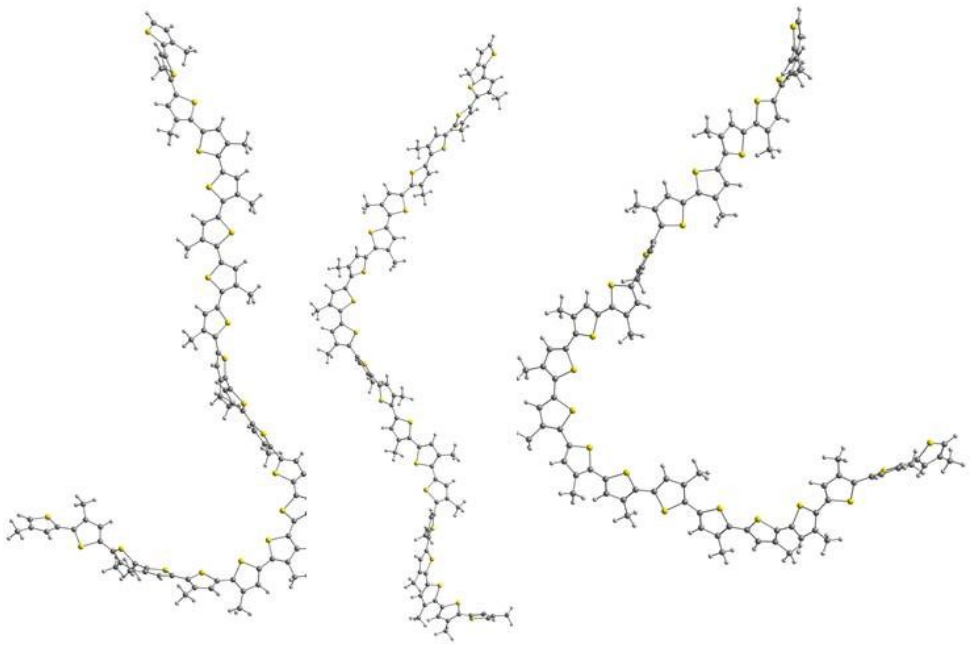

Figure 3.6. Twenty thiophene unit long oligomers constructed using the geometry of the optimized T3MT internal rings from Fig. 3.2 Three sample oligomer conformations are shown.

A set of 250 random nuclear geometries of rr-P3MT with a total length of 20 α-linked 3-methylthiophene units which vary in twist angle were prepared along with a planar anti chain. Then, TD-DFT or TD-HF calculations for the lowest four excitations were performed. The transition density of the lowest excited state is decomposed into electron and hole components using NTO analysis[161] and then population analysis is performed on the resulting orbitals. Finally, the populations are coarse-grained to individual 3-methylthiophene units and the resulting electron and hole probability functions are representative of the exciton size. DFT, TD-DFT, TD-HF, and NTO calculations were performed with Gaussian 09,[157] while population analysis and other calculations were performed with Matlab.

One can generate an approximate Maxwell-Boltzmann distribution of polymer geometries using a calculated torsional potential, assuming that other geometric parameters (such as inter-subunit bond length and angle) change only minimally upon geometric relaxation. When Φ is rotated and held fixed. The calculated torsional potentials of T3MT were fit with a Fourier series given by

$$E(\Phi) = \sum_n C_n (1 - sin(\Phi - \Phi_0)). \qquad \text{(Eq. 3.1)}$$

The polymeric structure is created from the central two thiophene rings of T3MT with varying Φ. That is, the molecular geometry of these rings in the optimized conformation (~150°) is used for each 3-methylthiophene ring but attached to a subsequent 3-methylthiophene ring with the torsional angle selected. These torsional angles were selected by Monte Carlo sampling from the probability calculated according to

$$P(\Phi) = \frac{exp(E(\Phi)/kT)}{\int exp(E(\Phi)/kT) d\Phi}. \qquad \text{(Eq. 3.2)}$$

where *k* is Boltzmann's constant and T is temperature set at 298 K. The geometries of the inner rings of the T3MT were then used to construct oligomers with twist angles sampled from the probability distribution given by Eq. 3.2.

After generating random oligomer conformations, TD-DFT calculations were performed. NTOs are generated by decomposing the transition density into electron and hole components for analysis of electron and hole localization, i.e. contributions to the transition density from unoccupied and occupied spaces, respectively.[161] This is especially useful for transitions with high degrees of 'mixing' due to electron correlation, as is seen in calculations with these disordered polymers, since transitions can not be characterized using single ground state MOs, i.e. transitions have components of many single particle transitions.[161,162] All excited state calculations were performed with the 6-31G(d) basis set.

NTOs are the result of singular value decomposition of the transition density matrix (**T**), defined in the(Kohn-Sham) MO basis as

$$\mathbf{T}_{ia} = \langle \phi_i \,|\, \hat{T}(r) \,|\, \phi_a \rangle \,. \qquad \text{(Eq. 3.3)}$$

where φ_i and φ_a are occupied and unoccupied MOs, respectively. NTOs are calculated from the transition density matrix with the unitary transformation

$$\mathbf{T} = \mathbf{U}\mathbf{S}\mathbf{V}^{\dagger} \qquad \text{(Eq. 3.4)}$$

The elements of $\mathbf{V}$ and $\mathbf{U}$ are given by

$$\mathbf{T}\mathbf{T}^{\dagger}\vec{u}_i = \lambda_i \vec{u}_i; \quad \mathbf{T}^{\dagger}\mathbf{T}\vec{v}_i = \lambda_i \vec{v}_i \qquad \text{(Eq. 3.5)}$$

and the NTOs calculated using the resulting transformation matrices according to

$$\phi_i^{NTO} = \phi_i \mathbf{U}; \quad \phi_a^{NTO} = \phi_a \mathbf{V} \,. \qquad \text{(Eq. 3.6)}$$

Each NTO is expressed in the basis set of the (Kohn-Sham) MOs and constructed either from the occupied or virtual space. Each pair of NTOs (one from occupied space and one from

virtual space) is associated with a specific λ which gives its relative contribution to the corresponding $\mathbf{T}$. In configuration space, $\sum\lambda_i = 1$, while for TD-DFT small deviation from unity may occur due to neglect of the contribution of de-excitation operators (Tamm-Dancoff approximation). These deviations are expected to be very small.[109,161]

To analyze localization of NTOs we performed Mulliken population analysis by constructing a density matrix (**D**) from the atomic orbital coefficients of NTOs, $C_{\mu(\nu)}$, defined by

$$D_{\mu\nu} = 2C_\mu C_\nu^* \qquad \text{(Eq. 3.7)}$$

and calculated the corresponding probability (P) of finding a hole or electron within basis function μ as

$$P_\mu = \sum_\nu D_{\mu,\nu} S_{\mu,\nu} \qquad \text{(Eq. 3.8)}$$

where $S_{\mu,\nu}$ is the basis function overlap matrix.[163] To reduce the computational effort, basis function overlap within only monomer units were considered.

In order to examine the localization of electron and hole along the polymer chain, the NTO probability distributions (several NTOs per oligomer) are weighted by eigenvalues and condensed classical probabilities on monomer units ($P(n) = \sum_{i(a)} \lambda_{i(a)} \sum_{\mu\in n} P_{\mu,i(a)}$, where n is the position of the monomer unit) resulting in electron ($P_e(n)$) or hole ($P_h(n)$) probability distribution for observation of an electron or hole in the nth thiophene unit. This neglects quantum interference effects. In general, transition densities for this ensemble of disordered polymer chains are described by 2-3 NTO pairs with λ greater than 0.1. Here, the first five NTOs are used. The electron and hole conjugation length (L_e and L_h) is calculated as the number of consecutive monomers containing 95% of the NTO population.

Gas phase absorption spectra for disordered oligomer chains were simulated by summing transitions broadened by Lorentzian functions with half width at half maximum of 0.05 eV and then weighted by the associated oscillator strength for the indicated transitions. Experimental absorption spectra were collected with a Cary WinUV spectrophotometer from well dissolved dilute solutions (approximately 0.01 mg/mL) of P3HT (Rieke Metals Sepiolid 200, >95% rr, 20-30kD, PDI=2.0) in chloroform and from a film spin-cast from P3HT in DCB. A quartz slide was placed on a spin coater and 0.5 mL of approimately 0.01 mg/mL P3HT solution was added with a pipetter. The slide was spun at approximately 600 rpm for 5 minutes to produce a thin film. It was then placed in a sample holder and the absorption spectra was measured.

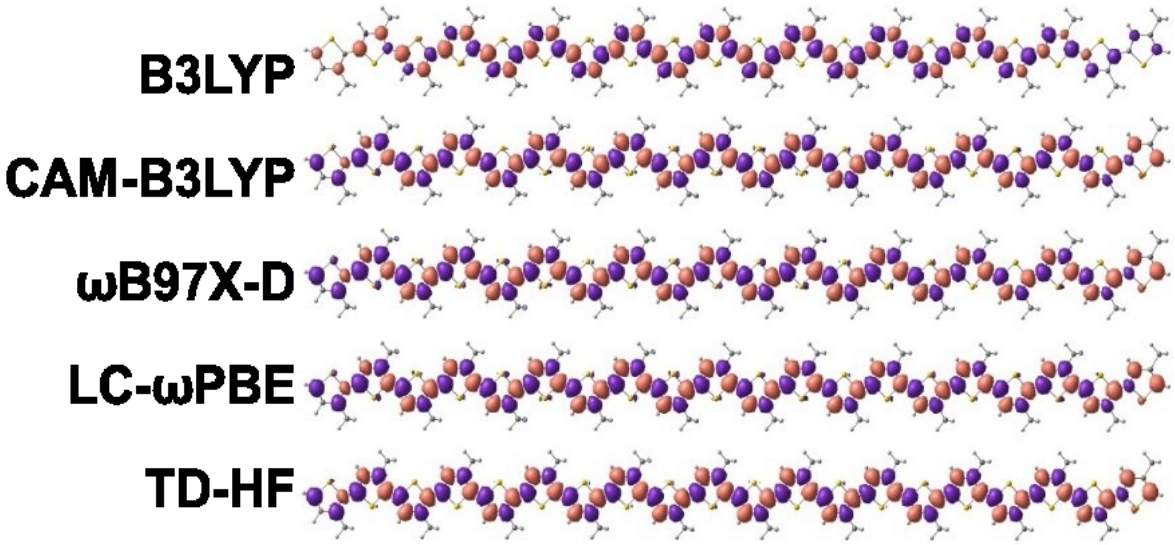

Figure 3.7. Transition densities calculated using various DFT functionals and TD-HF method for planar anti oligomer.

Results and Discussion

Planar Anti Conformation. In the planar anti conformation, transition densities occupy nearly the entire polymer chain, with slightly decreased occupation on terminal thiophene units irrespective of the method used in this study (Fig. 3.7). The number of monomer units occupied by the electron (L_e)and hole (L_h) depend on the calculation method (Table 3.1). For NTOs

pictured for CAM-B3LYP in Fig. 3.8, some localization is observed. The CAM-B3LYP NTOs are representative of NTOs calculated with other LCFs. The sets of LCFs vary only by slight changes in the extent of NTOs (Table 3.1).

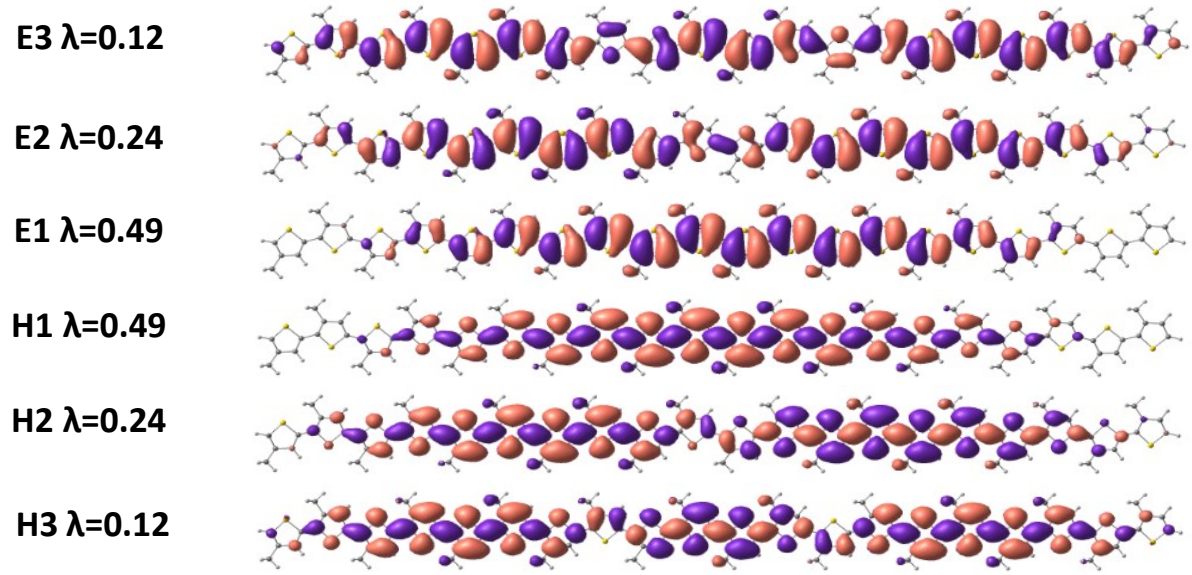

Figure 3.8. Natural transition orbitals from CAM-B3LYP calculations and corresponding eigenvalues. E stands for electron (unoccupied space), while H stand for hole (occupied space).

Table 3.1. Effective sizes for electron (L_e) and hole (L_h), and excitation energy (ω_{exc}) determined from calculations for planar anti oligomer.

	B3LYP	CAM-B3LYP	ωB97XD	LC-ωPBE	TD-HF
L_h	19	16	14	14	14
L_e	19	16	14	14	14
ω_{exc}/eV	2.02	2.56	2.65	2.93	2.84

Simulated Absorption Spectrum. The simulated absorption spectrum (Fig. 3.9) of disordered shows a general trend of decreasing maximum excitation energy from simulated absorbance spectra ($\omega_{exc,max}$) with increasing HF exchange for TD-DFT functionals. The lineshapes for the S_0->S_1 transition are approximately symmetric, while lineshapes comprised of the lowest four excitations include a tail at higher excitation energies due to the significant oscillator strength of these higher energy transitions. This is unlike higher energy transitions in calculations using the planar conformation where S_0->S_2, S_0->S_3, and S_0->S_4 transitions have

negligible oscillator strength. Both CAM-B3LYP and ωB97X-D are well suited to describe low lying optical transitions in conjugated molecules, which is further emphasized in this ensemble of polymers with unrelaxed geometries.

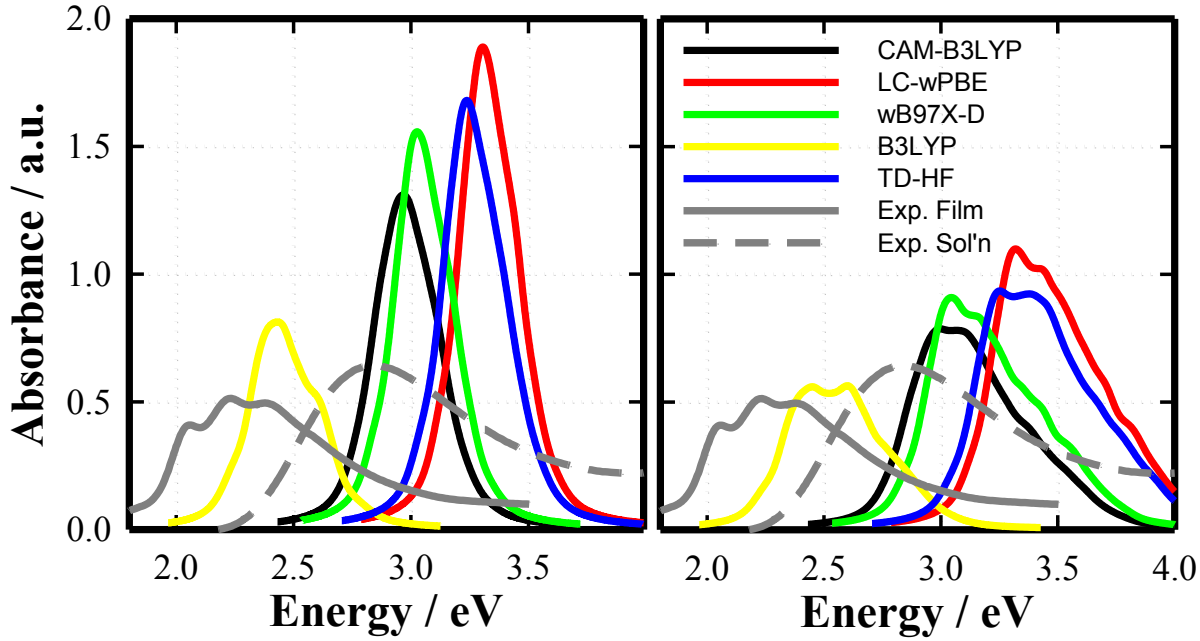

Figure 3.9. Simulated gas phase absorbance spectrum for S_0->S_1 (Left) and lowest four transitions (Right) for disordered polymers with experimental absorbance spectrum of P3HT in chloroform (dotted).

The simulated absorption spectrum of CAM-B3LYP and ωB97X-D have $\omega_{exc,max}$ ~0.2 eV higher than the experimental $\omega_{exc,max}$ of P3HT in chloroform solution, while calculations with the B3LYP hybrid functional predict $\omega_{exc,max}$ ~0.5 eV lower (Table 3.2). It is important to note that these are gas-phase calculations. With the inclusion of solvent effects, one might obtain even better agreement with the experimental results using CAM-B3LYP and/or ωB97X-D functionals. The effects of vibronic coupling on the simulated absorption spectra are not included here, but are likely to cause assymmetry in the absorption lineshape and may cause shifting of $\omega_{exc,max}$ to higher energy. That is, the maximum from the absorption lineshape may be shifted to higher energy due to the superposition of vibronic transitions with stronger transitions to vibrational states greater than 0. Regardless of these effects and the correspondence of excitation energy to

experiment, the relationship between conformation and excitation energy can be examined using calculations on the disordered polymer ensemble.

Neglecting solvent or vibronic effects on the absorbtion spectrum, CAM-B3LYP clearly reproduces the experimental spectrum with the highest accuracy. For analysis of other photophysical properties, CAM-B3LYP is used since it predicts the most reasonable excitation energies for the disordered ensemble of oligomer chains.

Electron/Hole Populations of Disordered Polymers. In the case of the lowest energy singlet excitation, conjugation length is easily characterized. For CAM-B3LYP, L_e and L_h range from 6-18 thiophene units long, with average values of 9 units (Fig. 3.10). Evidently, in the disordered ensemble electron and hole are more localized then in the planar anti configuration.

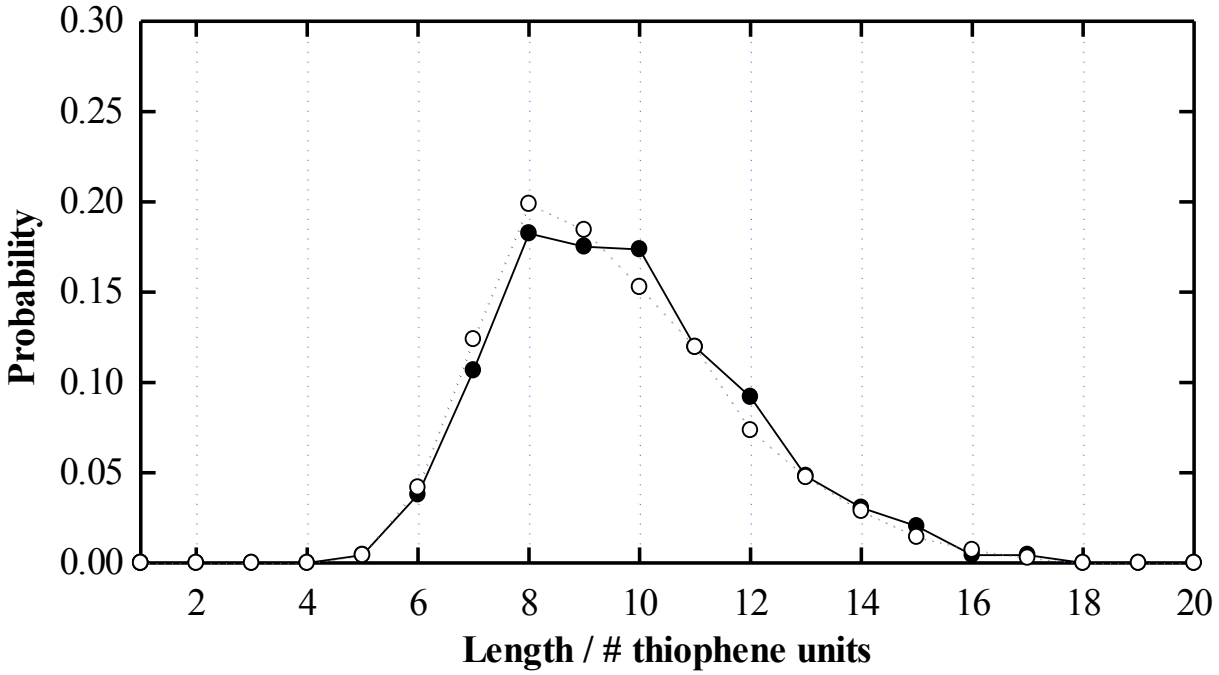

Figure 3.10. Distribution of electron (dotted) and hole (solid) NTO populations for S_0->S_1 transitions of an ensemble of disordered polymer calculated using CAM-B3LYP. The x-axis is the length of 95% of population along the disordered polymer chain.

Variation Within a Disordered Ensemble. To examine the effects of changing disorder, a larger ensemble of 500 polymer chains was prepared according to the presented methodology.

Calculations were performed with the CAM-B3LYP functional, since it reproduces the experimental absorbance spectra most accurately. To quantify the disorder in each oligomer chain, the average torsional potential for each chain is calculated as a measure of disorder. From the probability distribution given by Eq. 3.2, higher average torsional potential will have lower probability of occuring. If temperature were to be increased, the distribution of oligomers would sample more strongly from the higher energy conformations. This average torsional energy then gives a way of visualizing the effects of disorder on various properties. Plotting ω_{exc} and oscillator strength (f) as functions of the average torsional potential, the effects of increasing disorder can be visualized (Fig. 3.11). Although substantial variance is seen in these plots, trends emerge when moving averages (with a window of 1.8 meV) are calculated. Increasing disorder increases ω_{exc} and lowers f.

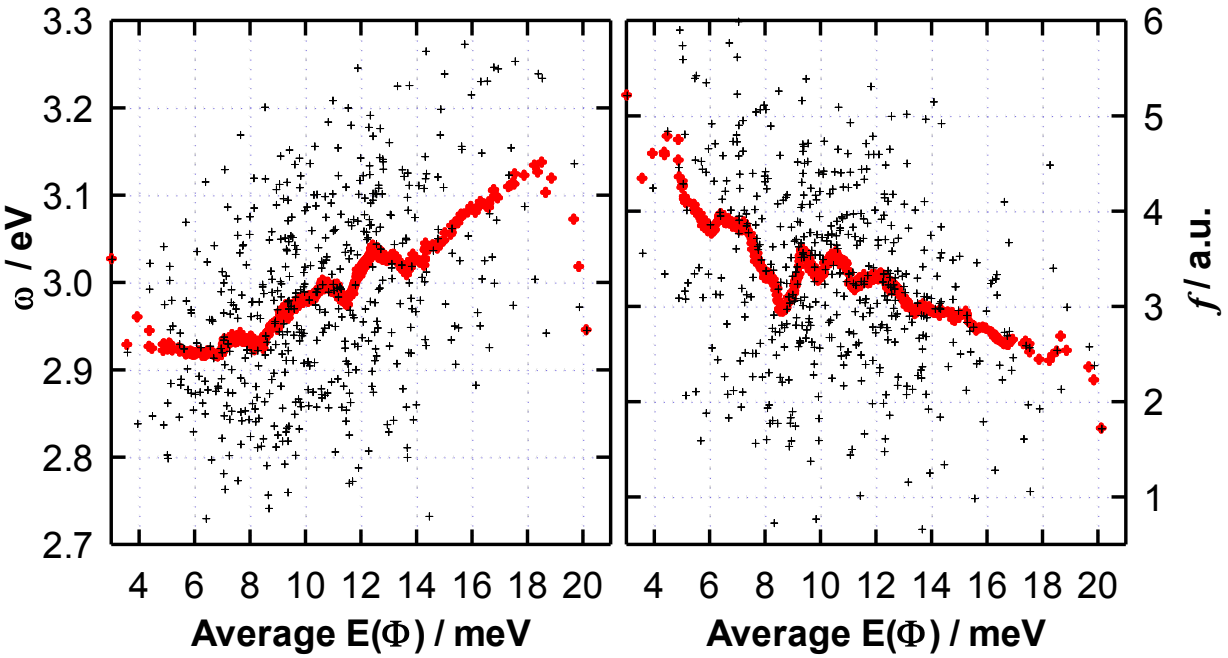

Figure 3.11. Distribution of excitation energy (ω_{exc}) (Left) and oscillator strength (f) (Right) as a function of average polymer torsional potential energy (black) and moving average of the distributions with a window of 1.8 meV (red).

The moving averages of ω_{exc} and f have a near linear dependence on average torsional energy. For ω_{exc}, average values range from ~2.9-3.1 eV, or ~30 nm difference in wavelength. At low average torsional energy, the average excitation energy tends towards convergence at ~2.9 eV. The calculated oscillator strength decreases with increasing disorder from oscillator strengths of ~3.5-2.5. These trends agree with experimental thermochromic spectra of polythiophene derivatives in both solution and solid state at temperatures where low energy peaks associated with aggregation are absent (i.e. in the melted polymer) or in derivatives which do not display additional low energy peaks.[36,164,165]

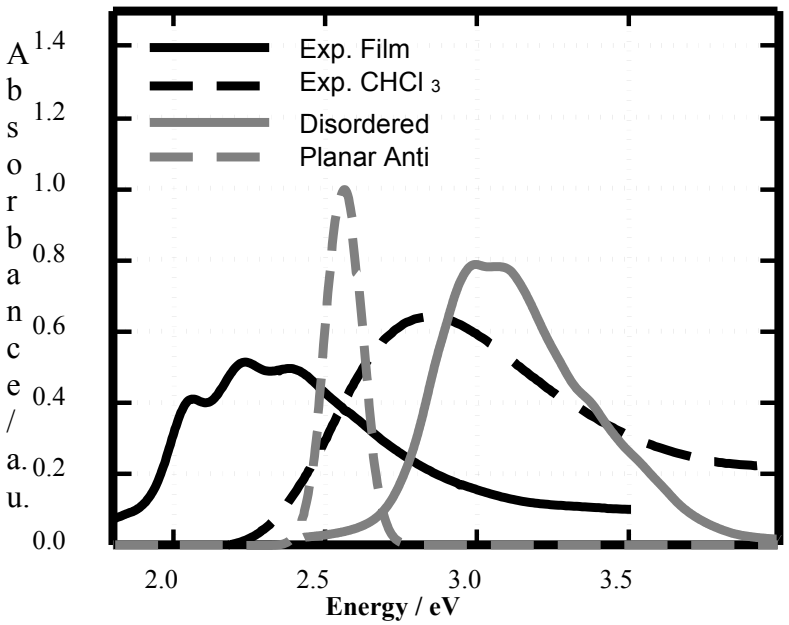

Figure 3.12. Comparison of simulated spectra using the CAM-B3LYP functional for the planar anti conformation and disordered ensemble of oligomers with experimental.

Comparison of Ordered and Disordered Calculations. In the planar anti conformation ω_{exc} is 0.5 eV higher than the corresponding $\omega_{exc,max}$ in the disordered ensemble (Fig. 3.12). This is similar to the difference in maximum absorption energy of solvated polymers and thin films. An explanation of this is confinement effects due to exciton size reduction, resulting in increased excitation energy in the disordered ensemble. The oscillator strength of planar anti oligomers

(8.04 for CAM-B3LYP) is greater than twice that of the average oscillator strength of disordered oligomers, predicting that the absorption cross section of crystalline polymers is higher than that of disordered polymers by a factor of two.

Discussion of Implications for Photovoltaic Properties. Planar anti chains are predicted to have a higher oscillator strength. Since crystallinity enforces planarity in P3HT, a larger absorption cross-section could lead to a higher rate of exciton generation. The lack of disorder in crystalline P3HT causes excitons to be of similar size, while torsional disorder causes excitons to be of a large range of sizes from 6-15 thiophene units as shown in Fig. 3.10. The large range of conjugation lengths present in disordered polymer chains may result in reduced electronic coupling integrals between chromophores in comparison with the planar anti conformation, since in a π-stacked conformation transition densities of differing size can not overlap to as great an extent as those of the same size. These electronic coupling integrals are further discussed in chapter 4. Results suggest that higher crystallinity in P3HT/PCBM devices increases device efficiency due, in part, to a greater rate of exciton generation and diffusion.

Conclusions

The optoelectronic properties of O3MT during photoexcitation have been examined using quantum chemical methods. Of several methods used, CAM-B3LYP gives the most accurate results regarding excitation energy for both the planar anti conformation and an ensemble of disordered oligomer chains. Comparison of planar anti chains and disordered ensemble shows greater average localization in the disordered ensemble. The range of electron and hole sizes in the disordered ensemble is large (6-15 repeat units), but the average exciton size of 9 repeat units is reduced from the planar anti case of 16 repeat units. This chapter builds on previous studies[22–24] of singlet excitations in disordered conjugated polymers by separately examining electron and

hole in systems with static disorder. The methodology used here to build disordered polymer chains is now used in chapter 4 to created disordered dimer ensembles for calculation of electronic couplings for exciton diffusion simulations.

MULTISCALE SIMULATIONS OF EXCITON DIFFUSION IN SEMICRYSTALLINE POLY(3-HEXYLTHIOPHENE)

Morphology Dependent Exciton Diffusion Length

Introduction

To understand the role of semicrystalline morphology in exciton, it is difficult to find a single computational model for simulations. Methods generally applied to organic molecules, such as DFT or molecular dynamics, are not well suited to simulate this system because of the range of length and timescales involved. Therefore, a combination of methods which are coupled in a multiscale model is used here. This chapter details a scheme developed and used to examine transport in semicrystalline films of P3HT.

It was shown in chapter 2 how crystallinity can vary with film thickness and difficulties in measuring L_D were then discussed. This chapter is focused on the microscopic dynamics of exciton transport in semicrystalline P3HT. In chapter 2, it was described how existing measurement methods assume that excitons diffuse homogeneously in crystallites. In this chapter, it's predicted that this is not the case. In fact, L_D is predicted to be predominated by transport in crystallites. This diffusion is anisotropic, so that the relative orientation of crystallites in a semicrystalline material is important when measuring macroscopic properties.

In P3AT chains, excitons are localized to segments of the conjugated polymer chain.[18,22,74] This effectively creates subunits of the polymer backbone which act as single chromophores. In thin films, these subunits are packed together in crystalline or amorphous domains.[149] Thin films of P3HT have been prepared with various morphologies, and transport properties may be highly dependent on the crystalline shape, size, and orientation.[71]

Films of P3HT are effectively modeled as type 1 crystallites dispersed in a matrix of disordered P3HT chains.[118] From thin films spin-cast from solvents such as DCB or chloroform, crystallites are rectilinear, with the longest crystallite axis extend along the π-stacking direction ($\vec{\boldsymbol{b}}$-axis).[50,71] On the other hand, in films prepared using vapour annealing techniques, nanofibers of P3HT can be prepared which are comprised of only a few unit cells along the $\vec{\boldsymbol{b}}$-axis and extended length along the interdigitated $\vec{\boldsymbol{a}}$-axis.[70,158] With such precise control over the morphology of P3HT nanocrystals, an understanding of the effects on transport properties 'opens the door' to tunable L_D.

Herein, transport through a semicrystalline medium is decribed using a kinetic Monte-Carlo scheme.[166] To perform such a simulation requires both a means of calculating the hopping rates between sites (chromophores) and a method of accounting for hopping between regions of crystalline and amorphous morphologies. In order to connect the simulation with experiment and make it widely applicable to various materials, the parameters governing the transport rates should be derivable from experimental sources and the morphology should be variable. The model described in this study fulfills these requirements and could be used to examine L_D in a wide range of materials,

L_D is related to specific aspects of the microstructure and optical properties of polymer aggregates that can be determined from experiment and/or theory. These factors are the distance between chromophore units, the coupling between them, their relative energy, and the reorganization energy (Stokes' Shift) of the exciton. The transport (hopping) rate depends on intermolecular interactions, which are strong in crystallites.

It is intuitive to expect that the crystalline microstructure is important for this optoelectronic property. Indeed, this has been found experimentally.[35] However, the dynamics of

diffusion in semicrystalline P3HT have not been examined experimentally, possibly because of difficulties in observing picosecond dynamics on the single molecule scale. The purpose of this chapter is to examine these properties in a computational model. By doing so, an understanding of the effects of morphology on L_D can be achieved

Theory and Methodology

Transport Rate. Exciton transport at room temperature can be described as diffusive. In this case, transport is a hopping process. Thermal relaxation of the exciton occurs on a timescale much shorter than the average chromophore residence time (rapid thermalization).[167] The transition rate for an exciton to hop between chromophores ($k_{mn,}$ for a transition from chromophore m to chromophore n) can then be described by a Golden rule type expression (Eq. 1.4).[41]

In the case of harmonic intramolecular vibrations and the limit of high-temperature (T), D_{mn} can be given as a function of excitation energies (E^{ex}) and Stokes' shifts (S) of the relevant chromophores. Following May and Kuhn,[86] the transition rates become

$$k_{mn} = |J_{mn}|^2 \left(\frac{2\pi}{\hbar^2 k_B T (S_m + S_n)}\right)^{1/2} \exp\left\{-\frac{(E_m^{ex} - E_n^{ex} + (S_m + S_n)/2)^2}{2 k_B T (S_m + S_n)}\right\}. \quad \text{(Eq. 4.1)}$$

This result is very similar to Marcus theory for electron hopping rates as described in the introduction.[86] The Stokes' shift and reorganization energy are clearly similar in that they describe the relaxation that occurs due to site occupation. This energy can be recovered and exchanged between molecules during hopping as part of Förster energy transfer according to this expression.

Thermally assisted hopping to higher energy sites is also possible. A Miller-Abrahams type hopping rate is then necessary to describe the thermal population of phonon's available for hopping to higher energy sites.[168] Then, the transition rate becomes

$$\tilde{k}_{mn} = k_{mn}\begin{cases}1 & \text{if } E_m^{ex} \geq E_n^{ex} \\ \exp\{-\frac{E_n^{ex}-E_m^{ex}}{k_B T}} & \text{if } E_m^{ex} < E_n^{ex}\end{cases} \quad \text{(Eq. 4.2)}$$

which, upon substitution of k_{mn} with Eq. 4.2, can be expressed as

$$\tilde{k}_{mn} = \begin{cases}|J_{mn}|^2(\frac{\pi}{\hbar^2 k_B T\bar{S}})^{1/2}\exp\{-\frac{(\Delta E^{ex}+\bar{S})^2}{4k_B T\bar{S}}\} & \text{if } E_m^{ex} \geq E_n^{ex} \\ |J_{mn}|^2(\frac{\pi}{\hbar^2 k_B T\bar{S}})^{1/2}\exp\{-\frac{(\Delta E^{ex}-\bar{S})^2}{4k_B T\bar{S}}\} & \text{if } E_m^{ex} < E_n^{ex}\end{cases} \quad \text{(Eq. 4.3)}$$

Here, $\Delta E^{ex} = E_m^{ex} - E_n^{ex}$ and $\bar{S} = (S_m + S_n)/2$. Which can be simplified to give

$$\tilde{k}_{mn} = |J_{mn}|^2(\frac{\pi}{\hbar^2 k_B T\bar{S}})^{1/2}\exp\{-\frac{(|\Delta E^{ex}|+\bar{S})^2}{4k_B T\bar{S}}\}. \quad \text{(Eq. 4.4)}$$

This rate is plotted in Fig. 4.1 for various values of ΔE^{ex} and $\bar{S}$.

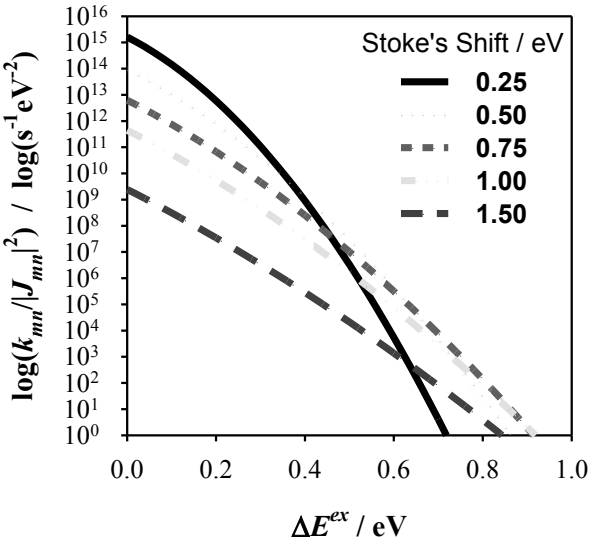

Figure 4.1. Relationship of calculated Miller-Abrahams/Forster type rate to expected values of excitation energy difference and average Stokes' shift. Rate decreases by several orders of magnitude as site energy difference is decreased.

In traditional Forster theory for exciton transfer, D_{mn} from Eq. 1.4 is calculated from the spectral overlap of chromophore ensembles.[124,169] The introduction of the site excitation energies and molecular Stokes' shifts give a molecular picture of energy transfer. That is, they are applicable to molecular properties rather than ensemble properties and facilitate the multiscale

methodology outlined in this chapter, where some molecular properties are calculated from DFT calculations. However, the excitation energies and Stokes' shifts are not determined from calculations, but extract from experimental optical spectra. Ergo, simulations can be parameterized by the experimental energy landscape.

This approach seems identical to that of Forster's, since the Forster rate's spectral overlap should be recovered upon random sampling of experimental optical spectra. However, the Forster rate cannot account for energy relaxation that occurs with hopping transport, which is important when more than one distinct energy landscape is present, e.g. in the case of semicrystalline films.[85] As opposed to simulations describing band-like transport where all energy states are spatially accessible, random sampling of energies from experimental lineshapes can better describe the discrete spatial nature of energy states accessible at each hopping site. These simulations describe completely thermalized, incoherent exciton transport. That is, when the relaxation time is much faster than the residence time. This approximation is best applied when the exciton is strongly coupled to the environment (thermal bath).[170]

The use of energy distributions from absorption and emission spectra leaves only $|J_{mn}|$ to be determined in Eq. 4.4. To model exciton diffusion in semicrystalline organic films, electronic couplings must be calculated for both the crystalline and amorphous regions. Quantum chemical methods are the most accurate in determining these couplings, which typically have values less than 0.1 eV.[72,160] The electronic coupling may be strongly affected by both the inter- and intra-molecular morphology.[149]

Due to the low disorder present in the crystal structure, it is reasonable to assume that the nuclear configuration remains static and use the intermolecular morphology derived from the P3HT crystal structure as presented in Fig. 1.5. However, for amorphous material, a range of

nuclear configurations must be accounted for. Thus, dimers of disordered deca(3-hexylthiophene) have been used to approximate electronic couplings in P3HT because disorder was predicted was predicted in chapter 3 to confine excitons to small sections (on average, 9 units) of the polymer chain.

Amorphous Dimer Morphologies. The morphology of chromophore dimers in amorphous domains of P3HT has been carried out using randomly oriented decamers with torsional angles selected from a Maxwell-Boltzmann distribution as performed in chapter 3. The potential energy function used for calculation of the Maxwell-Boltzmann distribution was derived from the gas phase torsional potential of T3MT calculated at the B3LYP/6-311G** level of theory and plotted in Fig. 3.2.

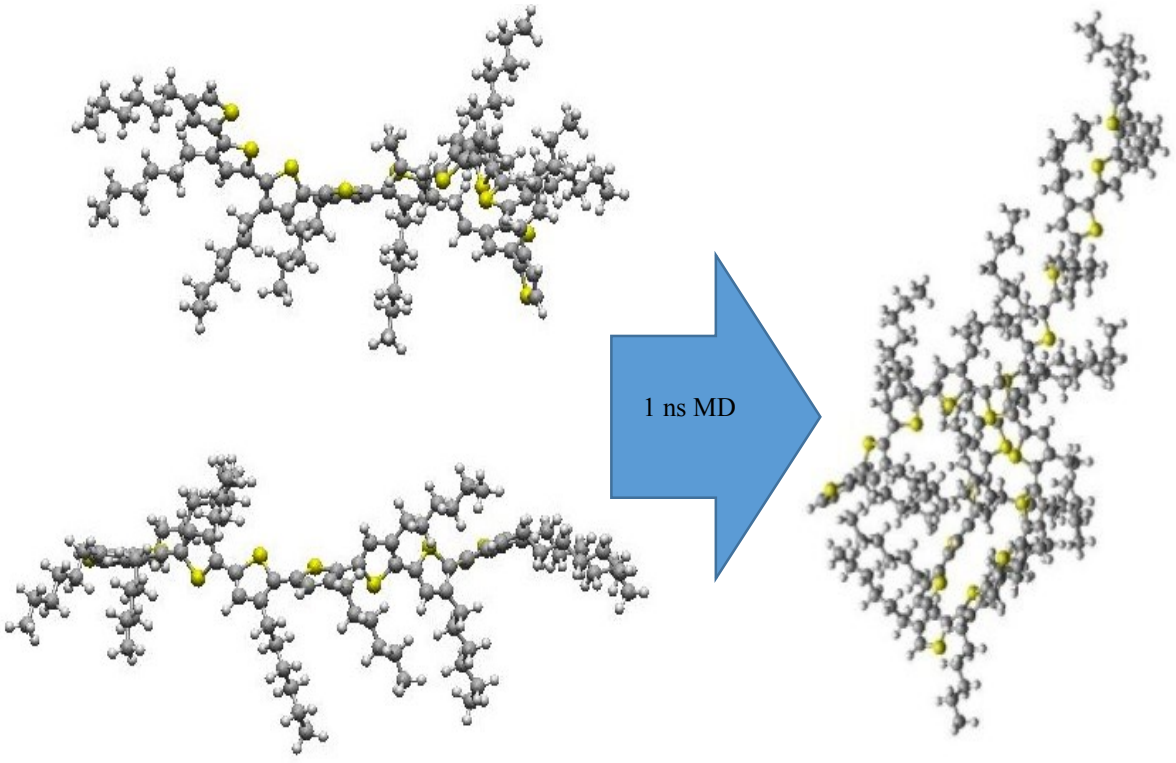

Figure 4.2. Representative geometry of generated disordered single chains and interacting dimer morphologies after molecular dynamics simulations performed for 1 ns.

These initial molecular nuclear geometries are then paired in a 5 nm cube with random molecular rotation and positional. Then, if any of the atoms of the first molecule are within 0.5 nm of the second molecule, a new molecular orientation of the second molecule is determined. Otherwise, an initial dimer configuration is accepted. Molecular dynamics simulations are then performed which allow these 'random' dimers to reach a room temperature configuration with intermolecular interactions (Fig. 4.2).

Molecular dynamics simulation using an MM3 type force field parameterized for polythiophene oligomers[114] is carried out for 1 ns using a NVT ensemble bath. In this bath, the motion of the molecules is at equilibrium with an environment that maintains constant volume, temperature, and number of molecules. These calculations were performed with the TINKER package.[171] The temperature was set at 273 K and volume was calculated in the TINKER package according to the default method. All other parameters were left as defaults. Generally, this is enough time for the molecules to become 'intertwined' due to the simulated Van-der Waals force. A fraction (~20%) of initial morphologies result in negligible intermolecular binding energy (V_b) and are discarded. V_b is calculated from molecular mechanics calculations using the difference in total energy of isolated and interacting components.

Electronic Coupling. There are a number of methods for calculating the electronic coupling between molecules.[72,160] For a review of various methods, the reader is directed towards the cited references. For a heterodimer of coupled two-level molecules, $|J_{mn}|$ is given from non-degenerate first-order perturbation theory of a two level system by

$$|\mathrm{J_{mn}}|^2 = |(\mathrm{E_+^{ex}} - \mathrm{E_-^{ex}})^2 - (\mathrm{E_m^{ex}} - \mathrm{E_n^{ex}})^2)|/2. \qquad \text{(Eq. 4.5)}$$

where $E^{ex}_{+/-}$ are the upper/lower excitation energies of the coupled dimer system for dimers in either crystalline or disordered morphologies .[172] Therefore, it remains only to calculate the coupled and uncoupled excitation energies.

Although computationally expensive, the calculation of 'supermolecular' excited state or excitation energies for a full dimeric system are an accurate means of determining the coupling for monomers in close proximity if the first principles method accurately captures dispersive and long-range interactions.[172] However, for large oligomers and polymers, the computational time required for such a calculation may be undesirable, especially if calculations for many molecular morphologies are required as in the case of disordered chromophores.

The result of Subsystem TD-DFT calculations are electronic couplings between transitions contrained to single molecules. The ground-state electronic structure of each subsystem is calculated separately using the SAOP exchange-correlation functional.[173] For this and further calculations, alkyl chains are truncated to methyl groups. Then, after relaxation of the electronic structure in the fixed potential of other subsystem, the uncoupled excitation energies are calculated with the PW91 functional for exchange and correlation.[174] Then, calculation of the coupled excitation energies is carried out.

The coupled transitions are calculated by solving the TD-DFT eigenvalue problem using a coupling matrix with subsystem structure as described by Eq. 1.16.[172] This step involves a non-additive modified version of the PW91 functional.[175] The resulting coupled and uncoupled excitation energies are used in Eq. 4.5 to determine $|J_{mn}|$. Further technical details of this procedure and the theoretical methodology are available in the above references. Calculations were carried out using the ADF 2012 package.[176]

Experimental Optical Spectra. P3HT (Rieke Metals Sepiolid 200, >95% rr, 20-30kD, PDI=2.0) absorbance and emission spectra were collected as follows. Solution UV-Vis and fluorescence spectra were taken as solutions in chloroform at a concentration of ~0.01 mg/mL. UV-Vis spectra were taken using a Varian Cary 50 spectrophotometer. Fluorescence spectra were taken using a Horiba-Yvon Nanolog Fluorimeter. Films were spin-cast from the same chloroform solution on glass substrates. A thin glass slide was placed on a spin-coater and 0.5 mL of solution was placed on the slide. It was then spun at 1400 rpm until dry.

Energy Landscape: Franck-Condon Analysis. To calculate rates using Eq. 4.5, the correct energy landscape is given by the 0-0 transitions in a given material. For crystalline regions this is derived from film spectra, while for disordered material it is derived from solution spectra. Using the absorption spectra of dilute P3HT in chloroform as a model for amorphous P3HT, it is necessary to subtract the amorphous contribution to thin film absorbance to model crystalline absorbance. Assuming that disordered chromophores have the same optical spectra in film and solution, the absorbance spectra of P3HT in chloroform is subtracted after being scaled to the high energy edge of the thin film absorption band. Then, Franck-Condon analysis is performed as described below.[50]

The 0-0 emission and absorption peaks were extracted using Franck-Condon analysis of the absorption and emission spectra at room temperature.[85] Spectra were fit with the function

$$I(E) \propto \sum_{i=0}^{n} \sigma(2\pi)^{-1/2}\eta^3 E^3 F(n) e^{-\frac{[(E-E_0)\pm(n-1)h\omega]^2}{2\sigma^2}} \qquad \text{(Eq. 4.6)}$$

where the Franck-Condon factors (*F(n)*)are given by

$$F(n) = \frac{S^{n-1}e^{-S}}{(n-1)!} \qquad \text{(Eq. 4.7)}$$

and the sign in the exponent of Eq. 4.6 is positive for absorption and negative for emission. Then, least-squares fitting of the Huang-Rhys parameter (*S*), full width at half maximum

(FWHM) (σ), 0-0 transition energy (E_0) and vibrational mode frequency (ω) to experimental spectra is performed. Since the spectra are normalized during fitting, the index of refraction (η) is irrelevant for the purposes herein, but is included for clarity.

These deconvolutions create the energy landscape for random-walk simulations. Site energies are drawn from Gaussian probability distributions given by the 0-0 absorption peaks of Franck-Condon deconvolutions. Stoke's shifts are determined by drawing from the probability distribution of the 0-0 emission peaks and subtracting from the drawn site energies. Similarly, the electronic coupling energy of amorphous material is drawn from the distribution presented above. This gives all necessary ingredients to calculate transfer rates for random-walk simulations.

Random-Walk Simulation. A kinetic Monte-Carlo scheme is used for random walk simulations in semicrystalline polymers. Standard kinetic Monte-Carlo schemes consider a choice of a path by choosing a random number u such that uR falls within the bounds of one of the rates in the cumulative sum, $R = \sum_m \tilde{k}_{mn}$. Then, the residence time can be calculated as $t = -\log(v)/R$, where v is a second random number.[166] At each step, new rates are calculated. The parameters which were used to calculate the rate selected by u from a given step are saved and used to determine the next set of rates. The procedure for calculating the rates is dependent on the location of the current site on the simulation lattice as described in the following.

The semicrystalline morphology is imagined as cuboids of $n_a l_a \times n_b l_b \times n_c l_c$ dimensions embedded in amorphous polymer. A visual description of the partitioning of the simulation space is given in Fig. 4.3. According to this idea, the lattice of sites in the crystallite are determined from the known unit cell dimensions. Practically, the crystallite is characterized by the coordinates of the edges of the crystallite. The simulation space not occupied by the cuboid is

considered amorphous. Periodic boundary conditions are defined in the amorphous region surrounding the crystallite. Within the amorphous region, an explicit lattice is not defined prior to hopping events. Rather, 6 nearest neighbors are assumed and hopping occurs in a random direction with distance of $l_{amorph}=3l_c$. This distance was chosen because it represents an approximate separation of excitons in the disordered dimer calculations. Other hopping events are also possible in semicrystalline morphologies.

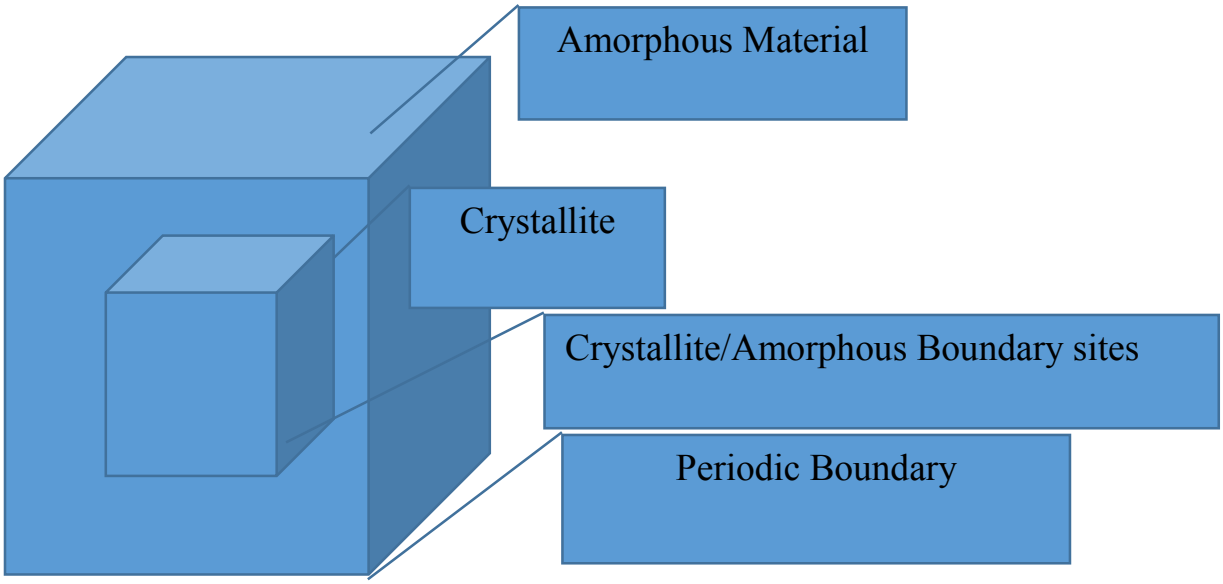

Figure 4.3. Scheme for simulating semicrystalline polymer films

Possible hopping events can then be categorized according to the location in the simulation box. When the initial location is in the amorphous region and the exciton coordinates are within a distance l_{amorph}, of the cuboid surrounding a crystallite, the exciton is considered to be at the edge of the amorphous region. In this case, the rate of hopping of one of the 6 nearest neighbors is calculated using a site energy and Stokes' shift drawn from the energy landscape of crystalline material, but with $|J_{mn}|$ drawn from the distribution for disordered dimers. This rate is used to approximate hopping from amorphous to crystalline material. If it is selected in the kinetic MC scheme, the nearest crystalline site becomes the current site. Otherwise, a random

direction is chosen like in amorphous to amorphous site hopping, but constrained to lie within the amorphous region of the simulation box. On the other hand, when the exciton is in a crystalline site directly adjacent to the amorphous region, it is considered to be at the edge of the crystallite. Accounting for rates of hopping on the crystalline lattice proceeds as follows.

In crystalline regions, there are 6 nearest neighbor sites corresponding to the three crystallographic directions. Rates are calculated for hopping in the $\vec{a}$ or $\vec{b}$ direction using the appropriate $|J_{mn}|$ and the crystalline energy landscape. For P3HT chains in crystallites of this size (10 repeat units), excitons are expected to occupy the entire length along the chain direction, the $\vec{c}$-axis.[149] That is, transport in the chain direction is assumed to be much more rapid than the average residence time. In this case, crystalline lattice sites have at least 2 nearest neighbors which are considered amorphous in the direction of the $\vec{c}$-axis. For hops at the edge of the crystallite from crystalline to amorphous material, the energy landscape of the amorphous material is used for the receiving chromophore and $|J_{mn}|$ is selected from the disordered dimer distribution. The direction of hopping in this case occurs to a 'virtual' unit cell located a distance l_i in the direction of the axis i of the selected hop, where i=*a, b, or c*.

Results and Discussion

Binding Energy of Disordered Dimers. The distribution of V_b for interacting disordered dimers shows a Gaussian type dependence of binding energy populations with mean of ~3 eV and FWHM of ~1 eV (Fig.4.4). Since V_b is much larger than kT, it is reasonable to attribute these conformations to possible amorphous film morphologies. It would be more accurate to justify the conformations through comparison of simulated and experimental densities, but this is not possible with dimer calculations because the dimer size is not large enough to give an average density. However, the strength of dimer binding energy provides justification for their use as

model systems for disordered film morphologies, where the conformation represents a potential minimum much greater than thermal fluctuations. After 1 ns of molecular dynamics, these intermolecular morphologies are then used in Subsystem-DFT calculations to determine $|J_{mn}|$ for calculation of hopping rates from Eq. 4.4.

Electronic Coupling. Electronic coupling for ordered dimers in crystalline geometries are calculated to be 6 meV in the $\vec{a}$-axis (interdigitated) and 23 meV in the $\vec{b}$-axis (π-stacking) where these morphologies are defined in Fig. 1.5. Calculations of electronic coupling using the interdigitated dimer were also performed with alkyl chains explicitly represented. The resulting electronic coupling magnitude is not changed in the structure with explicit alkyl chains. Similar results are expected for disordered dimers when alkyl chains are explicitly represented in amorphous dimer morphologies, but were not tested.

The $|J_{mn}|$ calculated here are lower than other reported values using different methodologies, e.g. transition density cube and transition dipole coupling.[72,160] Interestingly, experimental estimates from the work of Spano et al. discussed in chapter 1 predict interchain couplings in P3HT to be approximately 5-30 meV for spincast films.[79]

In disordered dimers, electronic coupling strengths between 0-22 meV were calculated (Fig. 4.4). The average electronic coupling from this distribution was 5.4 meV. In comparison to ordered dimers, the maximum electronic coupling is near that of π-stacked ordered dimers, the average is near that of interdigitated dimers, and the minimum is ~0 meV. According to this distribution, more than half of amorphous chromophore pairs have electronic couplings less than the minimum electronic coupling in crystallites. These differences obviously lead to lower average hopping rates in Eq. 4.4 for amorphous material. The same effect is found to be caused by the difference in energy landscapes.

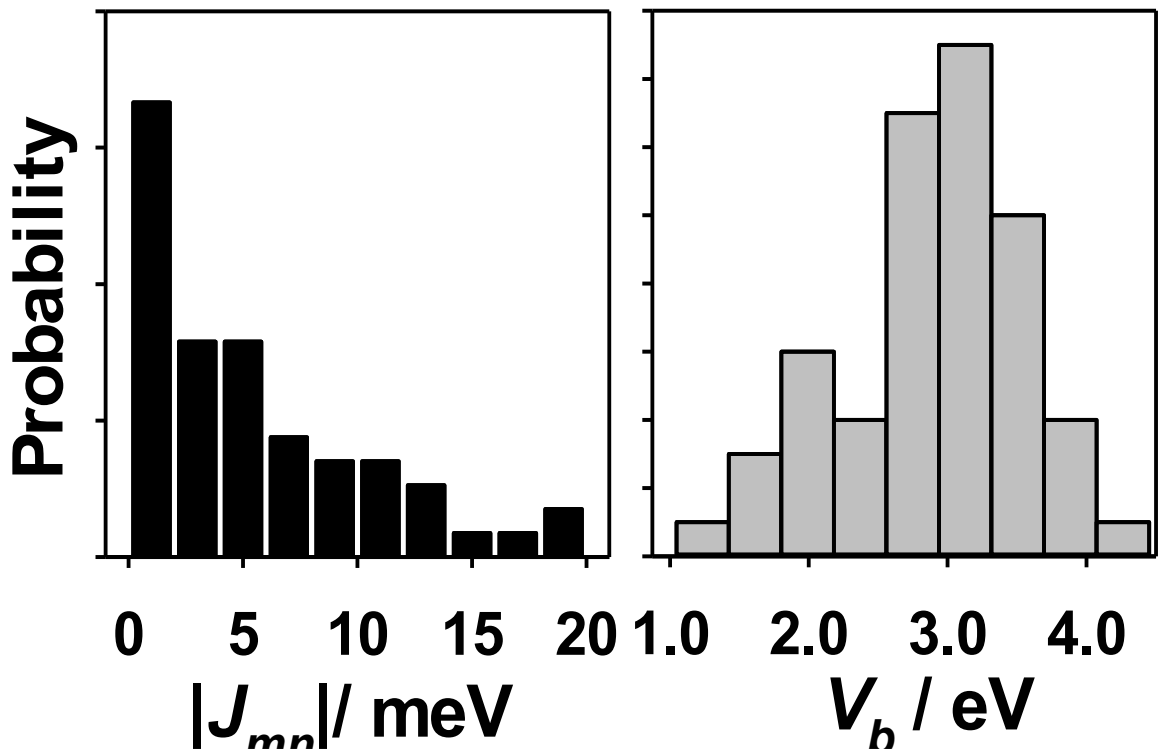

Figure 4.4. Histograms of calculation results for 50 amorphous dimers. Binding energy calculated from MD forcefield (V_b) (Right) and electronic coupling magnitude ($|J_{mn}|$) (Left) of final (1 ns) geometries of amorphous dimers.

Franck-Condon Deconvolutions. To extract the experimental energy landscape for parameterization of Eq. 4.4, it is necessary to determine the lineshape of the 0-0 transition from absorbance spectra (corresponding to ensemble distribution of E^{ex}) and from the emission spectra (in order to calculate the distribution of the molecular Stokes' Shift). The results of these deconvolutions are given in Table 4.1 and Figs. 4.5/4.6. The FWHM of vibronic peaks in the absorbance spectrum of solvated P3HT is much larger than the FWHM of absorbance in film and fluorescence in both film and solution. The difference is substantial (0.182 vs. 0.065-0.085) and 0-0 transition energies in film are red-shifted from solution. However, this is based on a nonstandard fitting of $h\omega$=0.33 eV for the solution absorption spectrum. Excitons are captured by crystallites in simulations of the semicrystalline morphology, as described in detail below.

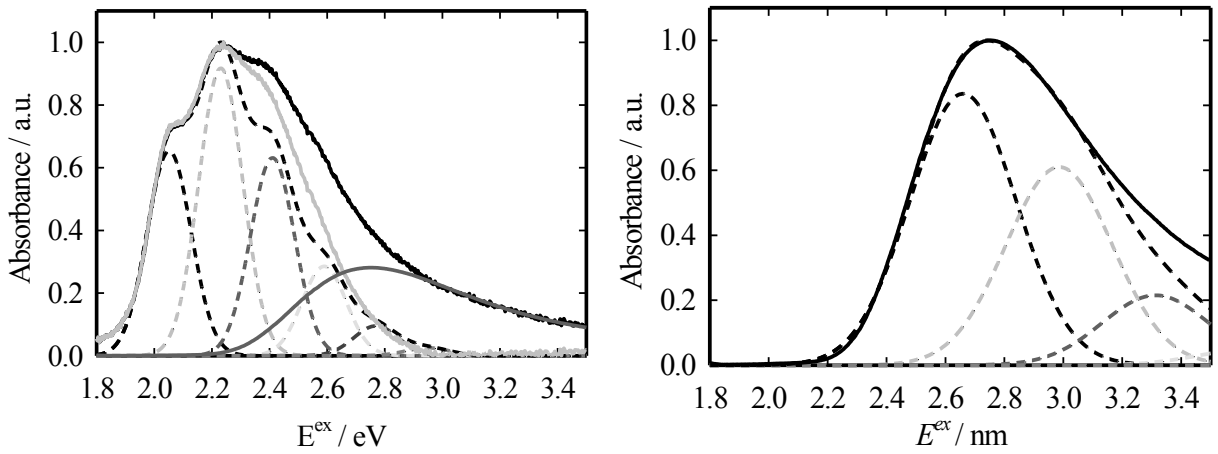

Figure 4.5. Franck-Condon deconvolutions of P3HT absorbance spectra. To isolate the approximate spectra of P3HT crystallites, the absorbance spectrum of P3HT in dilute chloroform solution was subtracted from the film spectra (after fitting the high energy tails of the two spectra). (Left) Film spectra. (Right) Dilute P3HT in chloroform.

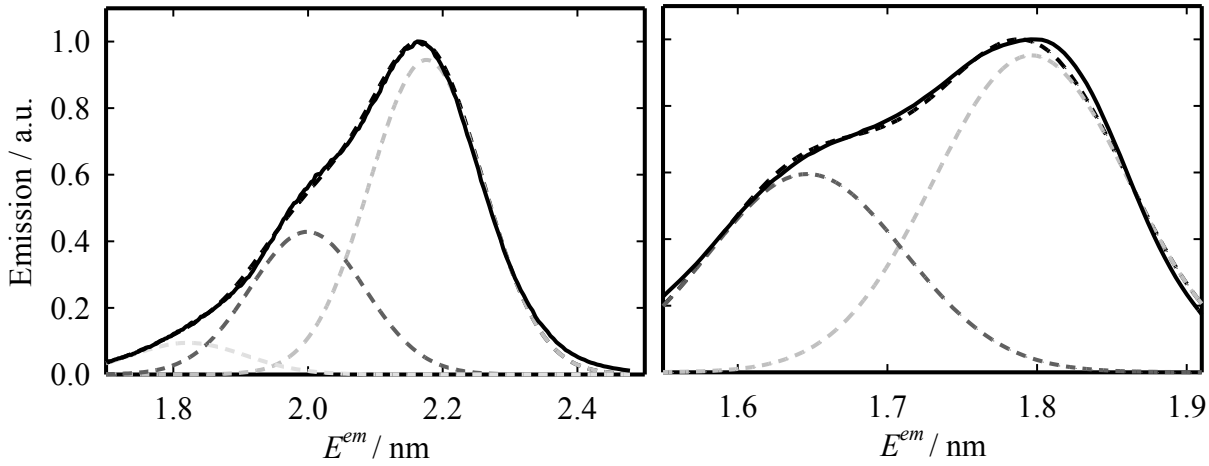

Figure 4.6. Franck-Condon deconvolutions of P3HT emission spectra. (Left) Film spectra. (Right) Dilute P3HT in Chloroform.

Table 4.1. Results of Franck-Condon deconvolutions of absorption and PL of dilute P3HT/$CHCl_3$ solution and thin films. Fitted parameters include energy of 0-0 transition (E_0), peak width, vibrational mode frequency (ω) and Huang-Rhys factor (S).

	Film		**Solution**	
	PL	**Abs**	**PL**	**Abs**
E₀	1.79	2.04	2.17	2.62
FWHM	0.065	0.077	0.085	0.182
hω	0.15	0.18	0.18	0.33
S	0.813	1.091	0.585	0.514

Effects of Energetic Disorder. In the absence of energetic disorder ($\Delta E^{ex}=0$), crystalline L_D is calculated to be 23 nm in the π-stacking direction and 19 nm in the interdigitated direction. These lengths are calculated for one dimensional diffusion (two nearest neighbors) from the average of $L_D=l_{hop}(\tau/2t)^{1/2}$, where t is the residence time. Including energetic disorder reduces this diffusion length (Table 4.2). In contrast, amorphous L_D is calculated to be 4.4 nm without disorder and 1.7 nm for disordered simulations. In fact, 62% of residence times are beyond the lifetime of an exciton in energetically disordered amorphous hopping, while this percentage is very small (~2 %) in energetically disordered crystal simulations.

Table 4.2. Calculated transport properties of excitons in crystalline and amorphous regions of semicrystalline thin films of P3HT with site energy disorder and without (Static). Mean diffusion length is calculated from the average of $L_D=l_{hop}(\tau/2t)^{1/2}$ where t is a residence time, l_{hop} is a hopping distance, and τ=470ps is the lifetime of P3HT. average log residence time is also given.

	Crystalline (a/b)		**Amorphous**	
	Disordered	**Static**	**Disorder**	**Static**
Diffusion Length / nm	**14/11**	**23/19**	**1.7**	**4.4**
Residence Time / ps	**8.1/0.7**	**2.1/0.2**	**2900**	**60**
Trapping Probability	**0.02/0.001**	**0**	**0.62**	**0**

L_D was measured in chapter 2 for a single thin film of 44 nm thickness (Fig. 2.5). The one dimensional L_D of this film was approximately 8 nm before annealing and 16 nm afterwords. This is of the same order of magnitude as calculated in these simulations. However, the absorbtion lineshape of similar films in Fig. 1.3 did not change upon annealing, suggesting that crystallinity did not change. As shown below, L_D is also dependent on the crystallite shape. It may be that crystallite shapes change upon annealing without changing the overall crystallinity of the film, but this assertion requires further evidence.

For amorphous material, beginning random walks at various initial site energies results in different relaxation times (Fig. 4.7), i.e. the time until the average site energy is the average 0-0 excitation energy. Excitation energies far from equilibrium (the average 0-0 excitation energy)

result in lengthened log residence times. Equilibration of the excitation energies to this mean value occurs in ~4 hops, while the time to equilibration is dependent on the initial excitation energy. Average log residence times are much longer than the P3HT singlet lifetime (470 ps)[177] at both the low and high edge of the 0-0 transition energy distribution. Fewer hops are necessary for equilibration at the low energy edge of the landscape than at the high energy edge.

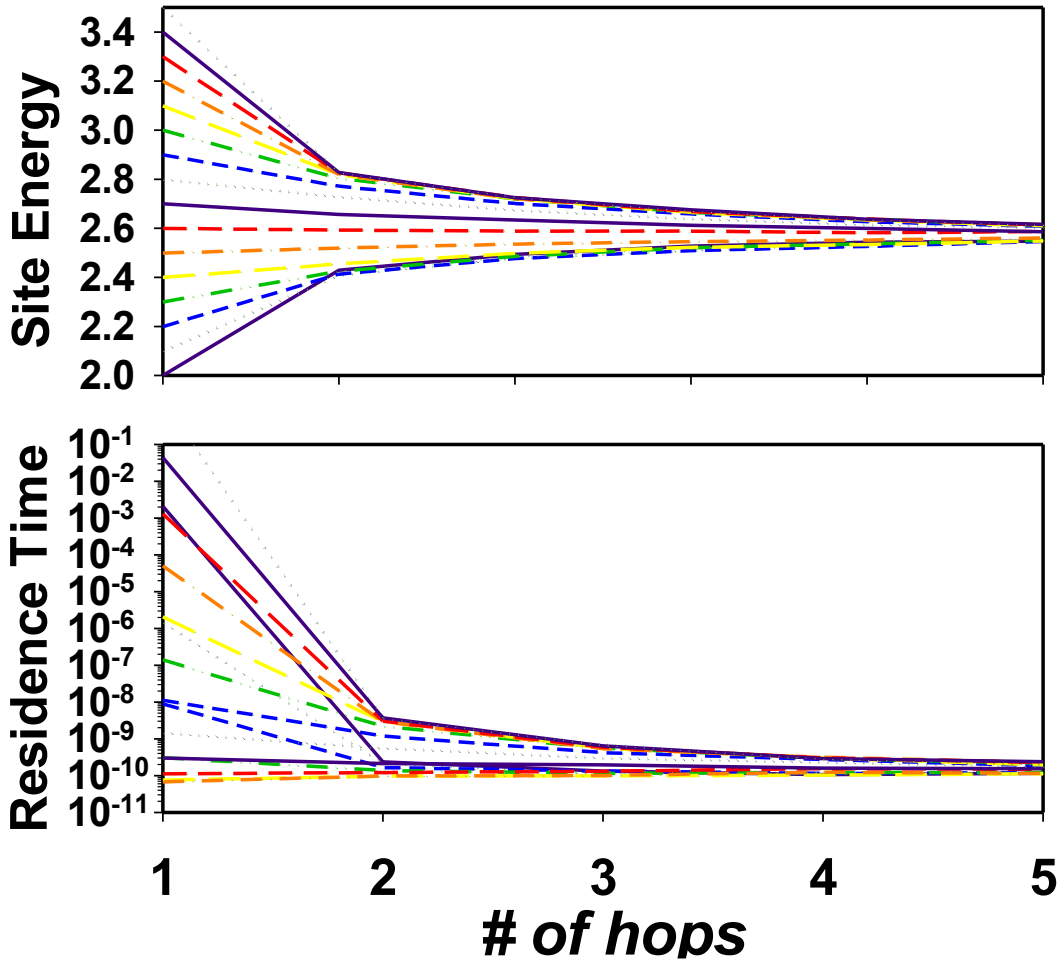

Figure 4.7. Average site energy (Top) and average log residence time (Bottom) after 1-5 hops for 10^6 short simulations for various starting energies. Starting energies are given by the points at 0 hops in the top figure.

Diffusion in Semicrystalline Morphologies. Initial excitons were placed at the center of a crystallite with average 0-0 excitation energy. The resulting L_D distributions show sampling of the entire crystallite for crystals of varying size, ranging from 3-10l_a x 5l_b and 3l_a x 5-40l_b. These

sizes correspond to what might be seen in an experimental thin film.[67] The predominant features of these distributions correspond to various combinations of unit cell lengths (Fig. 4.8).

Since these simulations are performed in semicrystalline morphologies, it is surprising that the major contribution to L_D is from crystalline hopping. This reflects the significant potential basin created by the lowered excitation (site) energies of crystalline polymer, as well as the longer residence time and high trapping probability of amorphous polymer. The effect of these qualities is that transport mainly occurs in crystallites.

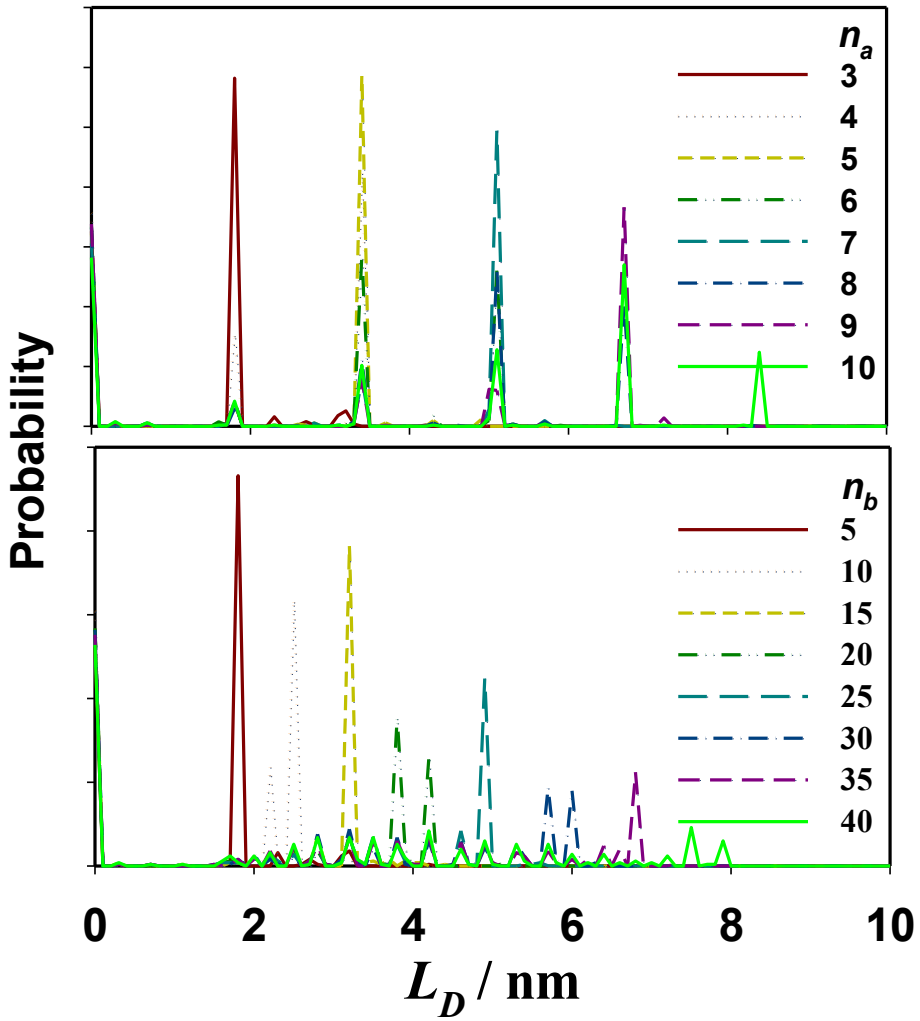

Figure 4.8. Simulation results of single exciton L_D, i.e. maximum distance traveled from starting point after 470 ps, for 10^3 iterations of MC simulation (Top) with number of $\vec{a}$-axis unit cells and 5 unit cells in the $\vec{b}$-axis direction. (Bottom) with varying number of $\vec{a}$-axis unit cells and 3 unit cells in $\vec{b}$-axis direction.

Long simulations (10^6 hops) were also analyzed. Here, the time scale separation between hopping in amorphous and crystalline material can be surpassed. To do so, the results of simulations were segmented at hops where an exciton jumps between crystalline and amorphous material. These simulation segments were then categorized as amorphous or crystalline paths based on their location in the simulation box. Distributions of the path times and distances were then created.

The distribution of the total time (τ_d) and maximum lengths (R_d) of paths through amorphous material reflect two distributions, one corresponding to rapid capture of excitons by crystallites and the second corresponding to long path times after escape from the local crystallite sites (Fig. 4.9). These line shapes are affected very little by crystallite size. The fraction of recaptured excitons is ~75% and ~25% of these make a single amorphous to amorphous hop before being recaptured. This process is also reflected in the distribution of maximum distance travelled by an exciton between leaving and returning to crystalline hopping sites, where a peak corresponding to a single amorphous hop along the crystalline-amorphous boundary is seen (Fig. 4.9).

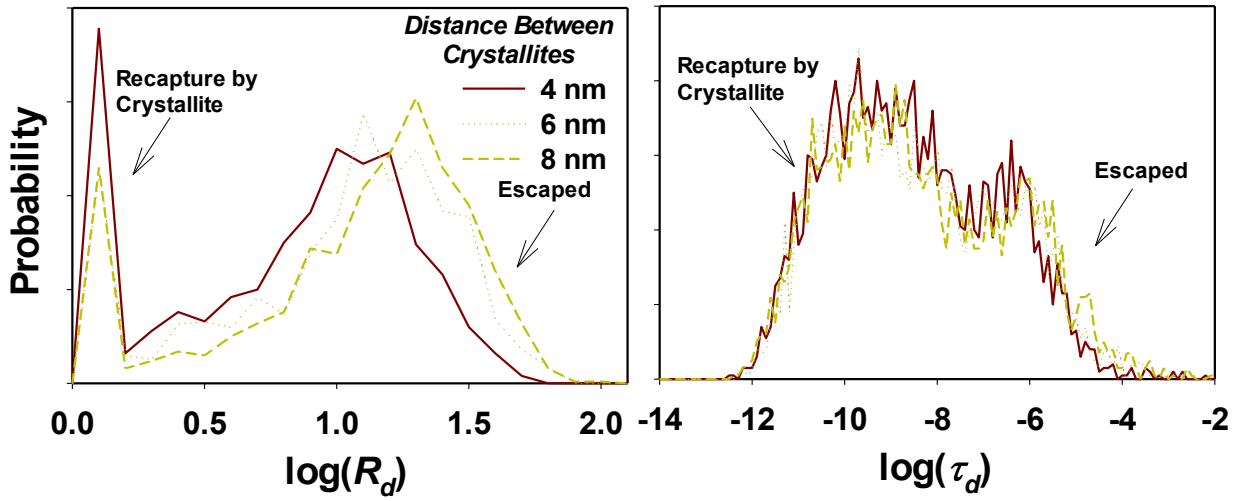

Figure 4.9. Distributions of maximum distance travelled (Left) and path times (Right) through amorphous material in semicrystalline morphologies with crystallites of dimensions $3l_a$ x $40l_b$ x $10l_c$ with varying separation between crystallites

While two distinct peaks are found in amorphous path times, crystalline path times (τ_c) have a single, sharper peak (Fig. 4.10). The peak has maximum in the nanosecond scale, but the tail extends into the picosecond regime. In these distributions, a decrease in the number of escaped excitons is observed upon lengthening crystallites from 5 to 10 unit cells, (compare n_b=5 with n_b>5 in Fig. 4.10). This decrease in escaped excitons arises when the crystalline dimensions are larger than the hopping length in amorphous material. Beyond this, there is very little variation in these distributions when changing crystallite size. This is a reflection of the ability of the exciton to traverse the entire nanocrystal several times in its lifetime with relatively low probability of jumping from the crystalline to amorphous material.

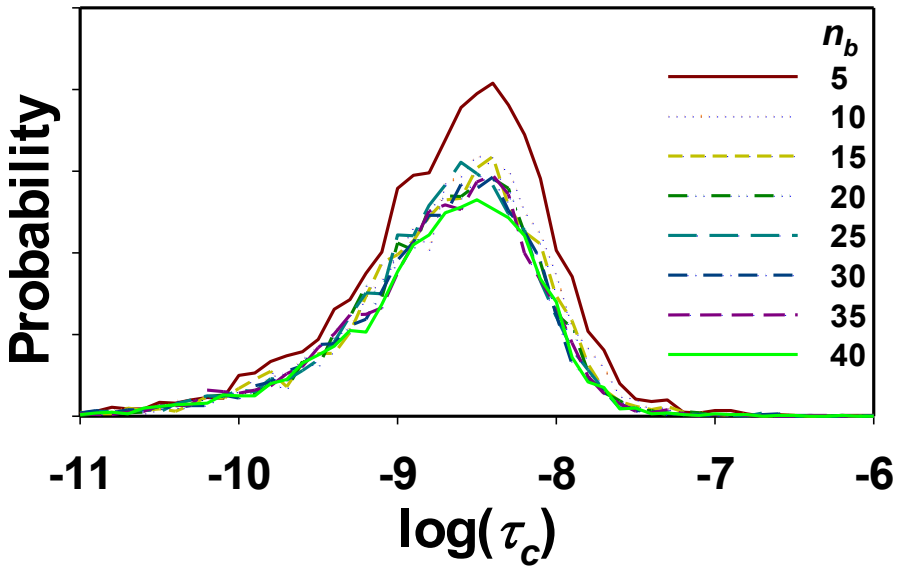

Figure 4.10. Distribution of path times in crystalline material for crystallites of varying size in the π-stacked direction and $3l_a$ x $10l_c$ with 4 nm separation between crystallites.

Discussion

Exciton Diffusion. This random walk simulation shows that exciton diffusion is much faster in crystalline material, while amorphous regions include many trapping sites for excitons. The time scale of paths through amorphous and crystalline material show that most excitons which travel through amorphous material do not reach crystallites when the crystallite spacing is

4-8 nm. Indeed, it is extremely rare for an exciton to reach two crystallites in the P3HT lifetime according to these simulations.

Due to the difference in energy landscape between crystalline and amorphous material, it is observed that exitons in crystallites are more likely to remain in crystallites than hop to amorphous material. Excitons which do hop out of amorphous material are likely to be recaptured immediately or after a single hop. If this phenomenon can be developed by choice of material and control of semicrystalline morphology, it may be useful to prepare more efficient devices and enhance the yield of exciton splitting for the following reasons.

In BHSCs, exciton splitting must occur in either amorphous material or at crystalline boundaries because acceptor material (e.g. PCBM) cannot penetrate crystallites. These simulations show that the crystallite energy landscape captures excitons from the higher energy amorphous material. If the relative energetics of crystalline and amorphous material can be tuned, it should be possible to enhance the probability that an exciton will make a single hop to amorphous material and be recaptured by crystallite sites where L_D is longer. Then, excitons can sample the most space in amorphous material in order to have a higher chance of encountering an acceptor. This highlights the importance of engineering microstructures that take advantage of the L_D of crystalline material while allowing exciton migration into amorphous material for exciton splitting.

In this chapter, results suggest that any model for exciton diffusion in semicrystalline P3HT should include these important features: 1.) A potential basin in the crystalline region with low roughness. 2.) Higher potential roughness in the amorphous regions surrounding crystallites, 3.) anisotropic transport rates in crystallites. It is important to note that the presented model does not include intramolecular relaxation between electronic states. That is, energetic relaxation

occurs during hopping only. Higher excited states can be populated due to energy transfer or excitation which then nonradiatively decay to lower, i.e. S_1, excited states before further energy transfer. The excitons here are considered as two level systems including only the lowest singlet excited state. In simulations where excitation is performed at high energy (Fig. 4.7), the residence time scale is very high due to very small D_{mn} (defined in Eq. 1.4). In reality, an exciting photon of high energy would likely populate states higher than S_1 and then nonradiatively decay to S_1 with or without spatial relocation of the excitation energy. In this case, the present simulation methodology is primarily applicable to band edge transport. That is, this model most accurately describes the transport of low energy excitons where only the first singlet excited state is populated on any chromophore site.

Conclusion

A multiscale model was described which combines quantum chemistry, molecular dynamics, and random walk simulations in order to simulate exciton diffusion in semicrystalline materials. This is the first attempt at performing random walk simulations of excitons in organic semicrystalline material of this type. Atomistic electronic coupling simulations of disordered dimers were performed that had a monotonically decreasing probability with magnitude, the probability decayed to zero upon reaching the electronic coupling strength of a π-stacked dimer. Using a Forster-type rate equation that allowed a molecular definition of the spectral overlap, rates were calculated by sampling energies from the experimental optical spectra. The resulting random-walk simulation on a semicrystalline lattice highlights the differences in diffusion dynamics in crystalline and amorphous material, showing that crystallites act as traps wherein rapid internal diffusion occurs.

REFERENCES

(1) Liang, Z.; Nardes, A.; Wang, D.; Berry, J. J.; Gregg, B. A. *Chem. Mater.* **2009**, *21*, 4914–4919.
(2) Brédas, J.-L.; Norton, J. E.; Cornil, J.; Coropceanu, V. *Acc. Chem. Res.* **2009**, *42*, 1691–1699.
(3) Blom, P. W. M.; Mihailetchi, V. D.; Koster, L. J. A.; Markov, D. E. *Adv. Mater.* **2007**, *19*, 1551–1566.
(4) Cheng, Y. J.; Yang, S. H.; Hsu, C. S. *Chem. Rev.* **2009**, *109*, 5868–5923.
(5) Dante, M.; Peet, J.; Nguyen, T. Q. *J. Phys. Chem. C* **2008**, *112*, 7241–7249.
(6) Hush, N. S. *Ann. N. Y. Acad. Sci.* **2003**, *1006*, 1–20.
(7) Spanggaard, H.; Krebs, F. C. *Sol. Energy Mater. Sol. Cells* **2004**, *83*, 125–146.
(8) Shirakawa, H.; Louis, E. J.; MacDiarmid, A. G.; Chiang, C. K.; Heeger, A. J. *J. Chem. Soc., Chem. Commun.* **1977**, 578–580.
(9) Heeger, A. J.; Kivelson, S.; Schrieffer, J. R.; Su, W.-P. *Rev. Mod. Phys.* **1988**, *60*, 781.
(10) Fichou, D. *Handbook of oligo-and polythiophenes*; John Wiley & Sons: New York, 2008.
(11) Hutchison, G. R.; Zhao, Y.-J.; Delley, B.; Freeman, A. J.; Ratner, M. A.; Marks, T. J. *Phys. Rev. B* **2003**, *68*, 035204.
(12) Meier, H.; Stalmach, U.; Kolshorn, H. *Acta Polym.* **1997**, *48*, 379–384.
(13) Becker, R. S.; de Melo, J. S.; Maçanita, A. L.; Elisei, F. *J. Phys. Chem.* **1996**, *100*, 18683–18695.
(14) Kanemitsu, Y.; Shimizu, N.; Suzuki, K.; Shiraishi, Y.; Kuroda, M. *Phys. Rev. B* **1996**, *54*, 2198.
(15) Bidan, G.; De Nicola, A.; Enée, V.; Guillerez, S. *Chem. Mater.* **1998**, *10*, 1052–1058.
(16) Parnell, A. J.; Cadby, A. J.; Mykhaylyk, O. O.; Dunbar, A. D. F.; Hopkinson, P. E.; Donald, A. M.; Jones, R. A. L. *Macromolecules* **2011**, *44*, 6503–6508.
(17) Jones, D.; Guerra, M.; Favaretto, L.; Modelli, A.; Fabrizio, M.; Distefano, G. *J. Phys. Chem.* **1990**, *94*, 5761–5766.
(18) Beenken, W. J. D. *Phys. Status Solidi* **2009**, *206*, 2750–2756.
(19) Turro, N. J.; Ramamurthy, V.; Scaiano, J. C. *Modern molecular photochemistry of organic molecules*; University Science Books: Sausalito, CA, 2010.
(20) Pomerantz, M. *Tetrahedron Lett.* **2003**, *44*, 1563–1565.
(21) Darling, S. B. *J. Phys. Chem. B* **2008**, *112*, 8891–8895.
(22) Beenken, W. J. D.; Pullerits, T. *J. Phys. Chem. B* **2004**, *108*, 6164–6169.
(23) Barford, W.; Lidzey, D. G.; Makhov, D. V.; Meijer, A. J. H. *J. Chem. Phys.* **2010**, *133*, 044504.
(24) Barford, W.; Trembath, D. *Phys. Rev. B* **2009**, *80*, 165418.
(25) Nayyar, I. H.; Batista, E. R.; Tretiak, S.; Saxena, A.; Smith, D. L.; Martin, R. L. *J. Phys. Chem. Lett.* **2011**, *2*, 566–571.
(26) Walczak, R. M.; Cowart Jr, J. S.; Abboud, K. A.; Reynolds, J. R. *Chem. Commun.* **2006**, 1604–1606.
(27) Jackson, N. E.; Savoie, B. M.; Kohlstedt, K. L.; Olvera de la Cruz, M.; Schatz, G. C.; Chen, L. X.; Ratner, M. A. *J. Am. Chem. Soc.* **2013**.
(28) Iyer, A.; Bjorgaard, J.; Anderson, T.; Köse, M. E. *Macromolecules* **2012**, *45*, 6380–6389.

(29) Huang, H.; Chen, Z.; Ortiz, R. P.; Newman, C.; Usta, H.; Lou, S.; Youn, J.; Noh, Y.-Y.; Baeg, K.-J.; Chen, L. X. *J. Am. Chem. Soc.* **2012**, *134*, 10966–10973.
(30) Shi, Y. *J Appl Phys* **2000**, *87*, 4254.
(31) Sirringhaus, H. *Adv. Mater.* **2005**, *17*, 2411–2425.
(32) Kelley, T. W.; Baude, P. F.; Gerlach, C.; Ender, D. E.; Muyres, D.; Haase, M. A.; Vogel, D. E.; Theiss, S. D. *Chem. Mater.* **2004**, *16*, 4413–4422.
(33) Toman, P.; Nešpůrek, S.; Weiter, M.; Vala, M.; Sworakowski, J.; Bartkowiak, W.; Menšík, M. *Polym. Adv. Technol.* **2009**, *20*, 263–267.
(34) Siebbeles, L. D. A.; Grozema, F. C.; de Haas, M. P.; Warman, J. M. *Radiat. Phys. Chem.* **2005**, *72*, 85–91.
(35) Lunt, R. R.; Benziger, J. B.; Forrest, S. R. *Adv. Mater.* **2010**, *22*, 1233–1236.
(36) Garreau, S.; Leclerc, M.; Errien, N.; Louarn, G. *Macromolecules* **2003**, *36*, 692–697.
(37) Barbara, P. F.; Gesquiere, A. J.; Park, S.-J.; Lee, Y. J. *Acc. Chem. Res.* **2005**, *38*, 602–610.
(38) Bolinger, J. C.; Traub, M. C.; Adachi, T.; Barbara, P. F. *Science* **2011**, *331*, 565.
(39) Clark, J.; Nelson, T.; Tretiak, S.; Cirmi, G.; Lanzani, G. *Nat. Phys.* **2012**, *8*, 225–231.
(40) Tretiak, S.; Saxena, A.; Martin, R. L.; Bishop, A. R. *Phys. Rev. Lett.* **2002**, *89*, 097402.
(41) Athanasopoulos, S.; Emelianova, E. V.; Walker, A. B.; Beljonne, D. *Phys. Rev. B* **2009**, *80*, 195209.
(42) Bjorgaard, J. A.; Kose, M. E. *J. Appl. Phys.* **2013**, *113*, 203707–6.
(43) Haugeneder, A.; Neges, M.; Kallinger, C.; Spirkl, W.; Lemmer, U.; Feldmann, J.; Scherf, U.; Harth, E.; Gügel, A.; Müllen, K. *Phys. Rev. B* **1999**, *59*, 15346–15351.
(44) Lyons, B. P.; Monkman, A. P. *Phys. Rev. B* **2005**, *71*, 235201.
(45) Walker, A. B. *Proc. IEEE* **2009**, *97*, 1587–1596.
(46) Hains, A. W.; Liang, Z.; Woodhouse, M. A.; Gregg, B. A. *Chem. Rev.* **2010**, *110*, 6689–6735.
(47) Venkataraman, D.; Yurt, S.; Venkatraman, B. H.; Gavvalapalli, N. *J. Phys. Chem. Lett.* **2010**, *1*, 947–958.
(48) Stubinger, T.; Brutting, W. *J. Appl. Phys.* **2001**, *90*, 3632–3641.
(49) Zhan, X.; Zhu, D. *Polym. Chem.* **2010**, *1*, 409–419.
(50) Scharsich, C.; Lohwasser, R. H.; Sommer, M.; Asawapirom, U.; Scherf, U.; Thelakkat, M.; Neher, D.; Köhler, A. *J. Polym. Sci. Part B Polym. Phys.* **2012**, *50*, 442–453.
(51) Scully, S. R.; McGehee, M. D. *J. Appl. Phys.* **2006**, *100*, 034907–034907–5.
(52) Shaw, P. E.; Ruseckas, A.; Samuel, I. D. W. *Adv. Mater.* **2008**, *20*, 3516–3520.
(53) Kroeze, J. E.; Savenije, T. J.; Vermeulen, M. J. W.; Warman, J. M. *J. Phys. Chem. B* **2003**, *107*, 7696–7705.
(54) Bässler, H. *Phys. Status Solidi B* **1993**, *175*, 15–56.
(55) Richert, R.; Ries, B.; Bässler, H. *Philos. Mag. B* **1984**, *49*, L25–L30.
(56) Köse, M. E.; Graf, P.; Kopidakis, N.; Shaheen, S. E.; Kim, K.; Rumbles, G. *ChemPhysChem* **2009**, *10*, 3285–3294.
(57) Zhang, X.; Li, Z.; Lu, G. *Phys. Rev. B* **2011**, *84*, 235208.
(58) Tian, Z.; Yu, J.; Wu, C.; Szymanski, C.; McNeill, J. *Nanoscale* **2010**, *2*, 1999–2011.
(59) Park, E. J.; Erdem, T.; Ibrahimova, V.; Nizamoglu, S.; Demir, H. V.; Tuncel, D. *ACS Nano* **2011**, *5*, 2483.
(60) Nagarjuna, G.; Baghgar, M.; Labastide, J. A.; Algaier, D. D.; Barnes, M. D.; Venkataraman, D. *ACS Nano* **2012**.

(61) Pecher, J.; Mecking, S. *Chem. Rev.* **2010**, *110*, 6260–6279.
(62) Tuncel, D.; Demir, H. V. *Nanoscale* **2010**, *2*.
(63) Venkatraman, B. H. Ph. D Dissertation, University of Massachusetts Amherst, 2011.
(64) Treat, N. D.; Brady, M. A.; Smith, G.; Toney, M. F.; Kramer, E. J.; Hawker, C. J.; Chabinyc, M. L. *Adv. Energy Mater.* **2011**, *1*, 82–89.
(65) Clarke, T. M.; Ballantyne, A. M.; Nelson, J.; Bradley, D. D. C.; Durrant, J. R. *Adv. Funct. Mater.* **2008**, *18*, 4029–4035.
(66) Yang, X.; Loos, J.; Veenstra, S. C.; Verhees, W. J. H.; Wienk, M. M.; Kroon, J. M.; Michels, M. A. J.; Janssen, R. A. J. *Nano Lett.* **2005**, *5*, 579–583.
(67) Hugger, S.; Thomann, R.; Heinzel, T.; Thurn-Albrecht, T. *Colloid Polym. Sci.* **2004**, *282*, 932–938.
(68) Dudenko, D.; Kiersnowski, A.; Shu, J.; Pisula, W.; Sebastiani, D.; Spiess, H. W.; Hansen, M. R. *Angew. Chem. Int. Ed.* **2012**, *51*, 11068–11072.
(69) Brinkmann, M.; Rannou, P. *Macromolecules* **2009**, *42*, 1125–1130.
(70) Brinkmann, M. *J. Polym. Sci. Part B Polym. Phys.* **2011**.
(71) Kline, R. J.; McGehee, M. D. *J. Macromol. Sci. Part C Polym. Rev.* **2006**, *46*, 27–45.
(72) Köse, M. E. *J. Phys. Chem. C* **2011**, *115*, 13076–13082.
(73) Lakowicz, J. R. *Principles of fluorescence spectroscopy,* 2nd ed.*;* Springer: New York, 1999.
(74) Scholes, G. D.; Rumbles, G. *Nat. Mater.* **2006**, *5*, 683–696.
(75) Singh, J. *Excitation energy transfer processes in condensed matter: theory and applications*; Plenum Press: New York, 1994.
(76) Kasha, M. *Radiat. Res.* **1963**, *20*, 55–70.
(77) Kasha, M.; Rawls, H. R.; El-Bayoumi, M. A. *Pure Appl Chem* **1965**, *11*, 371–392.
(78) Spano, F. C. *J. Chem. Phys.* **2005**, *122*, 234701–234701–15.
(79) Clark, J.; Silva, C.; Friend, R. H.; Spano, F. C. *Phys. Rev. Lett.* **2007**, *98*, 206406.
(80) Nguyen, T. *J Chem Phys* **1999**, *110*, 4068.
(81) Brown, P. J.; Thomas, D. S.; Köhler, A.; Wilson, J. S.; Kim, J.-S.; Ramsdale, C. M.; Sirringhaus, H.; Friend, R. H. *Phys. Rev. B* **2003**, *67*, 064203.
(82) Spano, F. C. *Annu Rev Phys Chem* **2006**, *57*, 217–243.
(83) Spano, F. C. *Chem. Phys.* **2006**, *325*, 22–35.
(84) Spano, F. C.; Clark, J.; Silva, C.; Friend, R. H. *J. Chem. Phys.* **2009**, *130*, 074904–16.
(85) Clark, J.; Chang, J.-F.; Spano, F. C.; Friend, R. H.; Silva, C. *Appl. Phys. Lett.* **2009**, *94*, 163306–163306–3.
(86) May, V.; Kühn, O. *Charge and energy transfer dynamics in molecular systems*; John Wiley & Sons: New York, 2008.
(87) Bredas, J. L.; Calbert, J. P.; da Silva Filho, D. A.; Cornil, J. *Proc. Natl. Acad. Sci.* **2002**, *99*, 5804.
(88) Nelson, J.; Kwiatkowski, J. J.; Kirkpatrick, J.; Frost, J. M. *Acc. Chem. Res.* **2009**, *42*, 1768–1778.
(89) Bickelhaupt, F. M.; Baerends, E. J. *Rev. Comput. Chem. Vol. 15* **2000**, 1–86.
(90) Furche, F. *J. Chem. Phys.* **2001**, *114*, 5982.
(91) Furche, F.; Ahlrichs, R. *J. Chem. Phys.* **2002**, *117*, 7433.
(92) Yanai, T.; Tew, D. P.; Handy, N. C. *Chem. Phys. Lett.* **2004**, *393*, 51–57.
(93) Del Bene, J. E.; Person, W. B.; Szczepaniak, K. *J. Phys. Chem.* **1995**, *99*, 10705–10707.
(94) Becke, A. D. *Phys. Rev.* **1988**, *38*, 3098.

(95) Becke, A. D. *J. Chem. Phys.* **1996**, *104*, 1040.
(96) Becke, A. D. *J. Chem. Phys.* **1993**, *98*, 1372–1377.
(97) Becke, A. D. *J. Chem. Phys.* **1993**, *98*, 5648–5652.
(98) Miehlich, B.; Savin, A.; Stoll, H.; Preuss, H. *Chem. Phys. Lett.* **1989**, *157*, 200–206.
(99) Pandey, L.; Doiron, C.; Sears, J.; Bredas, J.-L. *Phys. Chem. Chem. Phys.* **2012**.
(100) Chai, J.-D.; Head-Gordon, M. *Phys. Chem. Chem. Phys.* **2008**, *10*, 6615–6620.
(101) Grimme, S. *J. Comput. Chem.* **2006**, *27*, 1787–1799.
(102) Tawada, Y.; Tsuneda, T.; Yanagisawa, S.; Yanai, T.; Hirao, K. *J. Chem. Phys.* **2004**, *120*, 8425.
(103) Vydrov, O. A.; Scuseria, G. E. *J. Chem. Phys.* **2006**, *125*, 234109–9.
(104) Neugebauer, J.; Jacob, C. R.; Wesolowski, T. A.; Baerends, E. J. *J. Phys. Chem. A* **2005**, *109*, 7805–7814.
(105) Neugebauer, J.; Louwerse, M. J.; Baerends, E. J.; Wesolowski, T. A. *J. Chem. Phys.* **2005**, *122*, 094115–13.
(106) König, C.; Schlüter, N.; Neugebauer, J. *J. Chem. Phys.* **2013**, *138*, -.
(107) Khait, Y. G.; Hoffmann, M. R. *Annu. Reports Comput. Chem.* **2012**, 53.
(108) Neugebauer, J. *J. Phys. Chem. B* **2008**, *112*, 2207–2217.
(109) Dreuw, A.; Head-Gordon, M. *Chem. Rev.* **2005**, *105*, 4009–4037.
(110) Köse, M. *Theor. Chim. Acta* **2011**, *128*, 157–164.
(111) Gierschner, J.; Cornil, J.; Egelhaaf, H.-J. *Adv. Mater.* **2007**, *19*, 173–191.
(112) Lin, Z.; Bjorgaard, J.; Yavuz, A. G.; Iyer, A.; Köse, M. E. *RSC Adv.* **2012**, *2*, 642–651.
(113) Darling, S. B.; Sternberg, M. *J. Phys. Chem. B* **2009**, *113*, 6215–6218.
(114) Moreno, M.; Casalegno, M.; Raos, G.; Meille, S. V.; Po, R. *J. Phys. Chem. B* **2010**, *114*, 1591–1602.
(115) Tretiak, S.; Igumenshchev, K.; Chernyak, V. *Phys. Rev. B* **2005**, *71*, 033201.
(116) Barbosa, H. M. C.; Correia, H. M.; Ramos, M. M. D. *J. Nanosci. Nanotechnol.* **2010**, *10*, 1148–1152.
(117) Gommans, H.; Schols, S.; Kadashchuk, A.; Heremans, P.; Meskers, S. C. J. *J. Phys. Chem. C* **2009**, *113*, 2974–2979.
(118) Banerji, N.; Cowan, S.; Vauthey, E.; Heeger, A. J. *J. Phys. Chem. C* **2011**, *115*, 9726–9739.
(119) Zhokhavets, U.; Erb, T.; Gobsch, G.; Al-Ibrahim, M.; Ambacher, O. *Chem. Phys. Lett.* **2006**, *418*, 347–350.
(120) Zen, A.; Pflaum, J.; Hirschmann, S.; Zhuang, W.; Jaiser, F.; Asawapirom, U.; Rabe, J. P.; Scherf, U.; Neher, D. *Adv. Funct. Mater.* **2004**, *14*, 757–764.
(121) Rance, W. L.; Rupert, B. L.; Mitchell, W. J.; Kose, M. E.; Ginley, D. S.; Shaheen, S. E.; Rumbles, G.; Kopidakis, N. *J. Phys. Chem. C* **2010**, *114*, 22269–22276.
(122) Morfa, A. J.; Barnes, T. M.; Ferguson, A. J.; Levi, D. H.; Rumbles, G.; Rowlen, K. L.; van de Lagemaat, J. *J. Polym. Sci. Part B Polym. Phys.* **2011**, *49*, 186–194.
(123) Schneider, M.; Brinkmann, M.; Muccini, M.; Biscarini, F.; Taliani, C.; Gebauer, W.; Sokolowski, M.; Umbach, E. *Chem. Phys.* **2002**, *285*, 345–353.
(124) Forster, T. *Discuss. Faraday Soc.* **1959**, *27*.
(125) Cook, S.; Katoh, R.; Furube, A. *J. Phys. Chem. C* **2009**, *113*, 2547–2552.
(126) Shimizu, Y.; Kobayashi, T.; Nagase, T.; Naito, H. *Appl. Phys. Lett.* **2007**, *91*, 141909.
(127) Djurisic, A. B.; Li, E. H. *J. Appl. Phys.* **1999**, *85*, 7404–7410.

(128) Inagaki, T.; Arakawa, E. T.; Hamm, R. N.; Williams, M. W. *Phys. Rev. B* **1977**, *15*, 3243.
(129) Ng, A. M. C.; Cheung, K. Y.; Fung, M. K.; Djurisic, A. B.; Chan, W. K. *Thin Solid Films* **2008**, *517*, 1047–1052.
(130) Markov, D. E.; Amsterdam, E.; Blom, P. W. M.; Sieval, A. B.; Hummelen, J. C. *J. Phys. Chem. A* **2005**, *109*, 5266–5274.
(131) Denis, E.; Amsterdam, E.; Blom, P. W. M.; Sieval, A. B.; Hummelen, J. C. *J. Phys. Chem. A* **2005**, *109*, 5266–5274.
(132) Lunt, R. R.; Giebink, N. C.; Belak, A. A.; Benziger, J. B.; Forrest, S. R. *J. Appl. Phys.* **2009**, *105*, 053711–7.
(133) Cook, S.; Liyuan, H.; Furube, A.; Katoh, R. *J. Phys. Chem. C* **2010**, *114*, 10962–10968.
(134) Halls, J. J. M.; Pichler, K.; Friend, R. H.; Moratti, S. C.; Holmes, A. B. *Appl. Phys. Lett.* **1996**, *68*, 3120–3122.
(135) Markov, D. E.; Tanase, C.; Blom, P. W. M.; Wildeman, J. *Phys. Rev. B* **2005**, *72*, 045217.
(136) Wu, C.; Zheng, Y.; Szymanski, C.; McNeill, J. *J. Phys. Chem. C* **2008**, *112*, 1772–1781.
(137) Szymanski, C.; Wu, C.; Hooper, J.; Salazar, M. A.; Perdomo, A.; Dukes, A.; McNeill, J. *J. Phys. Chem. B* **2005**, *109*, 8543–8546.
(138) Lawton, W. H.; Sylvestre, E. A. *Technometrics* **1971**, *13*, 617–633.
(139) Ten Berge, J. M. F. *Psychometrika* **1977**, *42*, 267–276.
(140) Olmsted, J. *J. Phys. Chem.* **1979**, *83*, 2581–2584.
(141) Kubin, R. F.; Fletcher, A. N. *J. Lumin.* **1982**, *27*, 455–462.
(142) Fan, C.; Wang, S.; Hong, J. W.; Bazan, G. C.; Plaxco, K. W.; Heeger, A. J. *Proc. Natl. Acad. Sci.* **2003**, *100*, 6297–6301.
(143) Clafton, S. N.; Beattie, D. A.; Mierczynska-Vasilev, A.; Acres, R. G.; Morgan, A. C.; Kee, T. W. *Langmuir* **2010**, *26*, 17785–17789.
(144) Fitrilawati, F.; Tjia, M. O.; Pfeiffer, S.; Hörhold, H. H.; Deutesfeld, A.; Eichner, H.; Bubeck, C. *Opt. Mater.* **2003**, *21*, 511–519.
(145) Smilowitz, L.; Hays, A.; Heeger, A. J.; Wang, G.; Bowers, J. E. *J. Chem. Phys.* **1993**, *98*, 6504–6509.
(146) Kim, Y.; Swager, T. M. *Chem. Commun.* **2005**, *0*, 372–374.
(147) Lewis, A. J.; Ruseckas, A.; Gaudin, O. P. M.; Webster, G. R.; Burn, P. L.; Samuel, I. D. W. *Org. Electron.* **2006**, *7*, 452–456.
(148) Zade, S. S.; Bendikov, M. *Chem.--Eur. J.* **2007**, *13*, 3688–3700.
(149) Bjorgaard, J. A.; Köse, M. E. *J. Phys. Chem. A* **2013**, *117*, 3869–3876.
(150) Brunner, K.; Tortschanoff, A.; Warmuth, C.; Bässler, H.; Kauffmann, H. F. *J. Phys. Chem. B* **2000**, *104*, 3781–3790.
(151) Grozema, F. C.; Van Duijnen, P. T.; Yuri, A.; Ratner, M. A.; Siebbeles, L. D. A. *J. Phys. Chem. B* **2002**, *106*, 7791–7795.
(152) Chan, N. Y.; Hao, X.-T.; Smith, T. A.; Dunstan, D. E. *J. Phys. Chem. B* **2011**, *115*, 6838–6842.
(153) Orti, E.; Viruela, P. M.; Sanchez-Marin, J.; Tomas, F. *J. Phys. Chem.* **1995**, *99*, 4955–4963.
(154) Bredas, J. L.; Heeger, A. J. *Macromolecules* **1990**, *23*, 1150–1156.
(155) Van Eijck, L.; Johnson, M. R.; Kearley, G. J. *J. Phys. Chem. A* **2003**, *107*, 8980–8984.
(156) Ho, J.; Klamt, A.; Coote, M. L. *J. Phys. Chem. A* **2010**, *114*, 13442–13444.

(157) Frisch, M. J.; Trucks, G. W.; Schlegel, H. B.; Scuseria, G. E.; Robb, M. A.; Cheeseman, J. R.; Scalmani, G.; Barone, V.; Mennucci, B.; Petersson, G. A.; et al. *Gaussian 09*, revision B.01; Gaussian, Inc.: Wallingford CT, **2009**.
(158) Brinkmann, M.; Wittmann, J. C. *Adv. Mater.* **2006**, *18*, 860–863.
(159) De Leener, C.; Hennebicq, E.; Sancho-Garcia, J. C.; Beljonne, D. *J. Phys. Chem. B* **2009**, *113*, 1311–1322.
(160) Beenken, W. J. D.; Pullerits, T. *J. Chem. Phys.* **2004**, *120*, 2490–2495.
(161) Martin, R. L. *J. Chem. Phys.* **2003**, *118*, 4775.
(162) Batista, E. R.; Martin, R. L. Natural transition orbitals. In *Encyclopedia of Computational Chemistry*; von Ragu Schleyer, P., Allinger, N. L., Clark, T., Gasteiger, J., Kollman, P. A., Schaefer, H. F., III, Schreiner, P. R., Eds.; John Wiley & Sons Ltd.: Chichester, U.K., 2004.
(163) Mulliken, R. S. *J. Chem. Phys.* **1955**, *23*, 1833–1840.
(164) Roux, C.; Leclerc, M. *Chem. Mater.* **1994**, *6*, 620–624.
(165) Leclerc, M.; Fréchette, M.; Bergeron, J.-Y.; Ranger, M.; Lévesque, I.; Faïd, K. *Macromol. Chem. Phys.* **1996**, *197*, 2077–2087.
(166) Voter, A. F. In *Radiation Effects in Solids*; Springer: New York, 2007; pp. 1–23.
(167) Movaghar, B.; Grünewald, M.; Ries, B.; Bassler, H.; Würtz, D. *Phys. Rev. B* **1986**, *33*, 5545.
(168) Grünewald, M.; Pohlmann, B.; Movaghar, B.; Würtz, D. *Philos. Mag. B* **1984**, *49*, 341–356.
(169) Forster, T. *Ann. Phys.* **1948**, *437*, 55–75.
(170) Haken, H.; Strobl, G. *Z. Für Phys. Hadrons Nucl.* **1973**, *262*, 135–148.
(171) Ponder, J. W. TINKER: Software Tools for Molecular Design, 3.9 ed.; Washington University School of Medicine: Saint Louis, MO, 2001.
(172) Neugebauer, J. *J. Chem. Phys.* **2007**, *126*, 134116–12.
(173) Gritsenko, O. V.; Schipper, P. R. T.; Baerends, E. J. *Chem. Phys. Lett.* **1999**, *302*, 199–207.
(174) Perdew, J. P.; Chevary, J. A.; Vosko, S. H.; Jackson, K. A.; Pederson, M. R.; Singh, D. J.; Fiolhais, C. *Phys. Rev. B* **1992**, *46*, 6671–6687.
(175) Wesolowski, T. A.; Chermette, H.; Weber, J. *J. Chem. Phys.* **1996**, *105*, 9182–9190.
(176) Te Velde, G.; Bickelhaupt, F. M.; Baerends, E. J.; Fonseca Guerra, C.; van Gisbergen, S. J.; Snijders, J. G.; Ziegler, T. *J. Comput. Chem.* **2001**, *22*, 931–967.
(177) Cook, S.; Furube, A.; Katoh, R. *Energy Environ. Sci.* **2008**, *1*, 294–299.